Impact of electron correlation on light-induced demagnetization

Dissertation

zur Erlangung des Doktorgrades der Naturwissenschaften
Dr. rer. nat.

der

Naturwissenschaftlichen Fakultät II
Chemie, Physik und Mathematik

der Martin-Luther-Universität
Halle-Wittenberg

vorgelegt von

Herrn Périé de Barros, Tomás

geb. am 09.01.1995 in Coimbra, Portugal

Betreuer: Prof. Dr. Miguel A. L. Marques

1. Gutachter: Prof. Dr. Miguel A. L. Marques
2. Gutachter: Prof. Dr. Ingrid Mertig
3. Gutachter: Prof. Dr. Angel Rubio

Datum der Abgabe: 21.12.2022
Datum der öffentlichen Verteidigung: 30.06.2023
Vorsitzender der Promotionskommision: Prof. Dr. Roland Scheer

Abstract

The field of laser-induced ultrafast demagnetization has gathered a lot of attention, at both the experimental and theoretical level, for its possible technological applications. At the *ab initio* level, most density-functional-based studies in this area use the local spin-density approximation (LSDA) which is known to describe poorly the electronic structure of $3d$ transition metals.

In this thesis we employ a correction to the LSDA, the Hubbard U correction, to better account for Coulomb correlations among the localized d electrons and show that these correlations alter significantly the amount of demagnetization in both ferro- and antiferromagnetic materials with the $3d$ transition metals manganese, iron, cobalt, and nickel. We use the Hubbard U correction also as a tool to investigate the part that several laser parameters, such as pulse duration or intensity, play on the demagnetization dynamics. At the LSDA level with frozen ions the demagnetization is due to spin-orbit mediated spin flips after optical excitations. This in turn means that the rate of demagnetization depends critically on several parameters of the laser pulse used. Turns out that the amount of energy carried by the pulse is not a good indicator of how much a material will demagnetize and changes in pulse duration and shape influence significantly the outcome. We relate these findings to the electronic structure of the material and the phase space for optical transitions.

Abstrakt

Das Gebiet der laserinduzierten ultraschnellen Entmagnetisierung hat aufgrund seiner möglichen technologischen Anwendungen sowohl auf experimenteller als auch auf theoretischer Ebene viel Aufmerksamkeit erregt. Für theoretische Forschung in diesem Bereich wird meistens die Dichtefunktional mit der lokalen Spin-Dichte-Näherung (LSDA) verwendet. Von Letzterer ist bekannt, dass sie die elektronische Struktur von $3d$ Übergangsmetallen schlecht beschreibt.

In dieser Arbeit verwenden wir eine Korrektur der LSDA, die Hubbard U-Korrektur, um Coulomb-Korrelationen zwischen den lokalisierten d-Elektronen besser zu berücksichtigen. Wir zeigen, dass diese Korrelationen das Ausmaß der Entmagnetisierung sowohl in ferro- als auch in antiferromagnetischen Materialien mit den $3d$-Übergangsmetallen Mangan, Eisen, Kobalt und Nickel deutlich verändern. Wir verwenden die Hubbard U-Korrektur auch als Werkzeug, um die Rolle zu untersuchen, die verschiedene Laserparameter, wie Pulsdauer oder Intensität für die Entmagnetisierungsdynamik spielen. Auf dem LSDA-Niveau mit eingefrorenen Ionen ist die Entmagnetisierung auf Spin-Orbit-vermittelte Spin-Flips nach optischen Anregungen zurückzuführen. Dies wiederum bedeutet, dass die Geschwindigkeit der Entmagnetisierung entscheidend von mehreren Parametern des verwendeten Laserpulses abhängt. Es stellt sich heraus, dass die vom Puls übertragene Energiemenge kein guter Indikator dafür ist, wie stark ein Material entmagnetisiert wird, und dass Änderungen der Pulsdauer und -form das Ergebnis erheblich beeinflussen. Wir stellen die Verbindug diese Erkenntnisse mit der elektronischen Struktur des Materials und dem Phasenraum für optische Übergänge her.

Contents

Introduction **9**

1 Introduction **9**

2 Background **13**

2.1 Many-body problem 14

2.2 Density Functional Theory 15

2.2.1 The Kohn-Sham equations 16

2.2.2 Local Density Approximation 18

2.2.3 The LSDA+U method 19

2.3 Time-dependent DFT 21

2.3.1 Adiabatic LDA 22

2.3.2 Time propagation 23

2.4 Our calculations 26

2.4.1 Spin-orbit coupling 26

3 Ferromagnets **29**

3.1 Ground state convergence 30

3.1.1 Total energy and magnetization convergence 31

3.1.2 Density of states convergence 32

3.1.3 Demagnetization convergence 33

3.2 LSDA+U calculations 35

3.2.1 Effects of U on ground-state properties 36

3.2.2 Demagnetization dynamics with U 38

3.3 The effects of different laser parameters 45

3.3.1 Intensity 45

3.3.2 Pulse duration 50

3.3.3 Frequency 51

4 Antiferromagnets **53**
4.1 Ground-state convergence 54
4.1.1 Total energy and magnetization convergence 55
4.1.2 Density of states convergence 56
4.1.3 Demagnetization convergence 57
4.2 LSDA+U calculations 59
4.2.1 Effects of U on ground-state properties 59
4.2.2 Demagnetization dynamics 61
4.3 Probing different areas of the JDOS 67
4.3.1 Using the Hubbard U 67
4.3.2 Using different frequency pulses 68

5 Spin-orbit coupling **71**
5.1 Spin-orbit strength 71

6 Conclusion **75**

A Ground-state convergence in ferromagnets **79**

B LSDA+U results for Co and Ni **83**

C Demagnetization in Co under laser pulses of varying intensity **87**

D Ground state convergence in MnO and NiO **89**

E LSDA+U results for the antiferromagnets **93**

Bibliography **94**

Chapter 1

Introduction

Ever since Beaurepiare *et al.* first presented results of ultrafast demagnetization[1] (under the picosecond mark) in 1995 (see figure 1.1), a vast amount of effort, both at the experimental and theoretical level, has gone into trying to understand the mechanisms behind this phenomenon[2]. All this work is justified not only by the continuous human quest for knowledge but also by the possible technological advancements that a mastery of laser induced ultrafast demagnetization could provide. These include an increase in the speed of data storage by orders of magnitude[2], the creation of spintronic logic devices and the broader field of spintronics[3], as well as applications on time-resolved magnetic imaging[4].

This is clearly a complex problem where several different processes play important roles. The photons, the electrons, the lattice and the spins all interact with each other and all interactions have different contributions, some of more importance than others, to the overall process of femtosecond magnetism. This leads to a multitude of models attempting to describe this process. Some of the more important ones are the three temperature model[1], superdiffusive spin transport[5], Elliott-Yafet scattering induced spins flips[6], or spin-orbit induced spins flips.[7]

Ab initio simulations are evidently of great interest when trying to gain insights into how this phenomenon works. So far *ab initio* studies have investigated, for example, the role of spin-orbit interaction for Ni and Co films [8], the influence of finite size effects [9] and the possibility of demagnetizing correlated magnetic insulators [10]. These studies, and most *ab initio* studies in this field, use time-dependent density functional theory (TDDFT), which extends density functional theory (DFT) to the time domain enabling the application of these *ab initio* tools to dynamical problems such as the change in magnetic moments under the influence of an external field. The accuracy of DFT obviously depends on the density functional used, of which there are numerous options to chose from. The local spin density approximation (LSDA) is one of the most popular approximations used in *ab initio* TDDFT

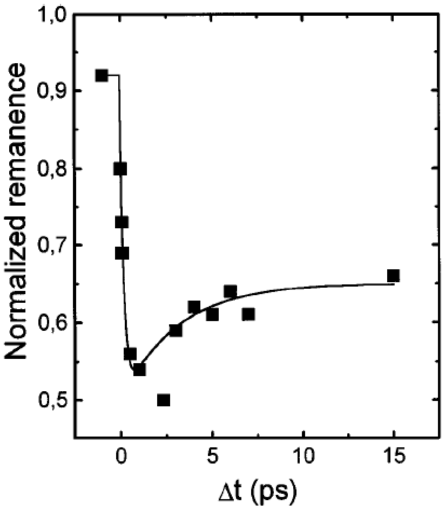

Figure 1.1: The graph that started it all, sub-picosecond laser induced demagnetization measured in ferromagnetic Ni, from ref. [1].

calculations in this area.[9, 11, 12] It is the simplest approximation possible, it was in fact the first one proposed done so in the very same paper where Kohn and Sham first proposed their DFT scheme[13]. Despite its simplicity it is a surprisingly effective tool, even more than one would expect. And yet it has some known problems. It has, for example, a tendency to delocalize the $3d$ electrons on transition metals. That is, the electronic structure of metals such as iron or nickel is not properly described with the LSDA.[14] How important is a correct description of these states in the demagnetization dynamics of materials containing $3d$ transition metals? That is one of the questions we will be looking at.

Another big issue with using the LSDA to describe demagnetization is that, to put it plainly, it just does not work very well. Several studies have shown that the demagnetization is severely underestimated when employing the adiabatic LSDA (ALSDA) in TDDFT calculations.[11, 15, 16] That is perhaps not too surprising given the amount of complexity ignored when using the ALSDA. For example one study [16] has found that memory effects that are ignored in the ALSDA have a profound impact and produce demagnetization that is larger and much closer to what is observed experimentally. The effects of phonons, usually also neglected, are becoming better understood as well.[17] Another important difference between the experimental results and those of computational simulations with the ALSDA is what happens after laser pulse. In reality the magnetization recovers, in a much longer time scale than that of the demagnetization [18], while in *ab initio* calculations that recovery is not present[19]. Part of the problem is that longer calculations are much more expensive and so simulations tend to focus on the initial process of demagnetization in only the first few femtoseconds (as, we must confess, is also the case of the results present in this thesis).

Another reason is that phonons likely play a key role in the recovery process and they also lead to more demanding calculations as they require larger cells. This, coupled with the fact that their lower time-scale means that they can be ignored in the first few femtoseconds, leads to phononic effects being often neglected in *ab initio* simulations. We must again make a *mea culpa* as we will also not consider phonons in our calculations but this is still an important discrepancy with reality that we should keep in mind.

It is the objective of the present work to contribute to a better understanding of the shortcomings of the ASLDA by investigating the role of correlations in demagnetization. That is, how does a better description of the ground-state impact the demagnetization dynamics in correlated systems? How does it affect the electronic structure of the systems in question and how can we relate that to the demagnetization observed?

To do so we employed the DFT+U method to different types of magnetic systems. This method is known to improve the electronic properties of $3d$ transition metals compared to the LSDA while still being quite efficient numerically. The Hubbard U also helps us to investigate the role played by various laser parameters, the ground-state electronic structure and the spin-orbit correction.

This thesis is organized as follows. In the next chapter we lay the foundations of our work. That means explaining the tools and concepts we will rely on for the rest of this work. We will go into more detail on DFT as well as explain what exactly constitutes the LSDA approximation. Then we move on to one way of improving on some of the shortcomings mentioned above, the Hubbard U correction also referred to as LSDA+U. Because ours is a dynamical problem a time-dependent theory is needed and so we will also go into some detail on TDDFT including some numerical considerations that are required when implementing it in practice. We then discuss spin-orbit coupling (SOC), a fundamental ingredient in time-dependent laser induced demagnetization.

In chapter 3, we start showing the fruits of our labour by applying the tools mentioned in chapter 2 to ferromagnetic materials. We first establish that our calculations are well converged with regards to a number of computational variables before moving on to results with the LSDA and LSDA+U. We finish this chapter not by looking directly at the effects of the Hubbard U but by using it as a way to investigate the impact of several different laser parameters on the demagnetization observed.

In chapter 4 we move on to a new class of materials, antiferromagnets. We follow the structure of chapter 3 and start by laying out all the necessary convergence to guarantee the validity of our results. Those results being the ones we show next, of the impact of the Hubbard U on the electronic structure of the antiferromagnets we study and how that changes their demagnetization dynamics. We conclude this chapter by investigating again the relationship between laser parameters, electronic structure and demagnetization.

The next chapter looks at the role of SOC on the demagnetization dynamics at this level of theory. We investigate how the demagnetization proceeds without SOC, as well as with different strengths for it.

In the final chapter we present the conclusions found throughout this thesis as well as some of the challenges still present.

Chapter 2

Background

Before we start presenting the results of the work done in this thesis (which we will do in its due course in the next chapters) we must first establish clearly the theoretical backdrop in which it was conducted. We will be performing computational simulations of the processes in question and investigating some of the shortcomings of some of the most popular methods used to investigate ultrafast demagnetization and so it is important that we are familiar with what these methods are, their theoretical basis, what approximations are used in the calculations and some other theoretical considerations important for our problem. All of this is addressed in this first chapter which is organized as follows.

The first section deals with our problem in the broadest of terms, how to tackle the systems we are interested in, systems with many electrons and many atoms, i.e. how to approach the many-body problem.

In the second section, we present what is one of the most popular theories used to solve the many-body problem and the one used in the work presented here, Density Functional Theory (DFT). We present the Kohn-Sham system, an ingenious solution to solve the problem in practice, as well as some of the approximations used in it, the ones used in this work, the Local Spin Density Approximation (LSDA) and an extension to it, used to better describe localized electrons, the LSDA+U.

But ours is not a static problem and so in the third section, we present an extension of DFT used to deal with time-dependent processes such as the demagnetization dynamics we are interested in, known as Time-Dependent Density Functional Theory (TDDFT). We introduce as well an extension of the LSDA to time-dependent problems, the Adiabatic Local Spin Density Approximation (ALSDA), and also some important considerations regarding the practical solution of the time-dependent Schrödinger equation, that is, how the time propagation is achieved.

Finally, we pool all things together and present the equations we will be dealing with in the remaining chapters as well as some considerations on spin-orbit coupling (SOC), a relativistic correction that plays an important role in ultrafast demagnetization.

2.1 Many-body problem

To study the problem of light-induced demagnetization in ferromagnetic solids we must first know how to describe such systems. At the simplest level, discarding relativistic effects and any external perturbation, a system of M nuclei and N electrons can be defined by the Hamiltonian

$$\hat{H} = -\frac{1}{2}\sum_i \nabla_i^2 + \frac{1}{2}\sum_{i\neq j}\frac{1}{|\mathbf{r}_i - \mathbf{r}_j|} - \sum_I \frac{1}{2M_I}\nabla_I^2 + \frac{1}{2}\sum_{I\neq J}\frac{Z_I Z_J}{|\mathbf{R}_I - \mathbf{R}_J|} + \sum_{i,I}\frac{Z_I}{|\mathbf{r}_i - \mathbf{R}_I|}, \tag{2.1}$$

where as usual lower case indices refer to the electrons and upper case indices correspond to the nuclei. Atomic units ($e = m_e = \hbar = 4\pi\epsilon_0 = 1$) have been used here and will also be used throughout this text. The electronic part of the system is described in the first two terms, $-\frac{1}{2}\sum_i \nabla_i^2 + \frac{1}{2}\sum_{i\neq j}\frac{1}{|\mathbf{r}_i - \mathbf{r}_j|}$, the first of which represents the kinetic energy of the electrons and the second represents the electron-electron interaction. The two next terms in the Hamiltonian represent the same quantities but for the nuclei, the kinetic energy $-\sum_I \frac{1}{2M_I}\nabla_I^2$ and the nucleus-nucleus interaction $\frac{1}{2}\sum_{I\neq J}\frac{Z_I Z_J}{|\mathbf{R}_I - \mathbf{R}_J|}$. Finally, the last term $\sum_{i,I}\frac{Z_I}{|\mathbf{r}_i - \mathbf{R}_I|}$ is the interaction between the electrons and the nuclei.

Now all that is left is to solve the time-independent Schrödinger equation

$$\hat{H}(\{\mathbf{r}\},\{\mathbf{R}\})\Psi(\{\mathbf{r}\},\{\mathbf{R}\}) = E\Psi(\{\mathbf{r}\},\{\mathbf{R}\}), \tag{2.2}$$

to obtain the system's wave-function $\Psi(\{\mathbf{r}\},\{\mathbf{R}\})$, where $\{\mathbf{r}\},\{\mathbf{R}\}$ represent the set of electronic ($\{\mathbf{r}\} = (\mathbf{r}_1, ..., \mathbf{r}_N)$) and nucleic coordinates ($\{\mathbf{R}\} = (\mathbf{R}_1, ..., \mathbf{R}_M)$), and then we could calculate the expected value of any property of interest. Unfortunately, this problem is too convoluted to solve in practice. The wave-function we would obtain from solving equation 2.2 is a function of $3N + 3M$ variables. There is just too much complexity, making solving this problem directly infeasible.

We can, however, try to tackle the problem by simplifying it. The nuclei mass is much bigger than the electron mass (around 1800 times bigger[20]) which means that the nuclear motion is a lot slower than the electronic motion. In fact, we can consider that the electrons move in a field created by the static nuclei and that they react instantaneously when the nuclei move. This allows us to separate the problem into two new ones, one dealing solely with the nuclear motion, and the other dealing with the electronic motion that depends on the positions of the nuclei simply as parameters. This is known as the Born-Oppenheimer approximation. Since we care only about the electronic properties, the nuclear problem can safely be ignored and we have thus successfully reduced our problem from $3N + 3M$ variables to only $3N$. But alas $3N$ is still too much for any meaningfully interesting system, the sheer amount of computational resources necessary is too big. An example of such difficulties, one that is mentioned elsewhere in the literature[21], is that of storing the ground-state wave-function of a simple atom, for instance, an oxygen one. An oxygen atom has eight electrons and so our wave-function depends on 24 coordinates. If we store this in a very modest grid with just 10 points for each coordinate that means we need to store 10^{24} numbers. If each number is a byte that is 10^{24} bytes, a quantity much greater than we can feasibly hope to deal with. And we haven't even accounted for spin yet.

Fortunately, there are several approaches to further treat and simplify the problem so that we can obtain relevant insights. One of the most popular ones, and the one used in this work, is known as DFT.

2.2 Density Functional Theory

In 1964 Hohenberg and Kohn published a paper where they proved two theorems[22]. The first of these theorems states that the electronic density ($n(\mathbf{r})$) uniquely determines, up to an additive constant, the external potential $v_{ext}(\mathbf{r})$ of a system of interacting particles. If the external potential is determined by the external potential then so is the Hamiltonian and thus also the wave-functions. This means that the expectation value of any observable is also a functional of the non-degenerate ground-state density

$$O[\mathbf{r}] = \langle \Psi[n(\mathbf{r})] | \hat{O} | \Psi[n(\mathbf{r})] \rangle \tag{2.3}$$

which in turn also provides the name for the overall theory, Density Functional Theory.

The second Hohenberg-Kohn theorem deals specifically with the energy. It states that the energy of the system, for any $v_{ext}(\mathbf{r})$, can be written as:

$$E_{HK}[n] = F[n] + \int v_{ext}(\mathbf{r}) n(\vec{r}) d\mathbf{r} \tag{2.4}$$

where $F[n]$ is a universal functional that encompasses all interactions not dependent on the external potential, and therefore is valid for any number of electrons. Moreover, the density that minimizes this energy functional is the ground-state energy and that minimum energy is the ground-state energy. If the universal functional $F[n]$ were known (and simple enough to calculate) all our problems would be solved. Regrettably that is not the case.

We have nonetheless succeeded in reducing our problem from looking for a function of $3N$ variables, the wave-function, to looking for a function of only 3 variables, the electronic density. Only one problem remains, how do we find the electronic density?

2.2.1 The Kohn-Sham equations

One year after Hohenberg and Kohn published their theorems, Kohn again, this time with Sham, proposed a way to calculate the many-body density[13]. The main idea to simplify the problem is to substitute the N electron problem with a fictitious system of non-interacting particles. Since all properties are a functional of the density, if the density of the fictitious system is the same as the real one then we can find the solutions we seek by solving the simpler non-interacting system.

The solutions for the new system are obtained through the so-called Kohn-Sham equations:

$$\left[-\frac{1}{2}\nabla^2 + \hat{v}_{KS}(\mathbf{r})\right]\psi_i(\mathbf{r}) = \epsilon_i\psi_i(\mathbf{r}). \tag{2.5}$$

The effective Kohn-Sham potential felt by the independent particles is given by

$$\hat{v}_{KS}(\mathbf{r}) = \hat{v}_{ext}(\mathbf{r}) + \int \frac{n(\mathbf{r}')}{|\mathbf{r}-\mathbf{r}'|}d\mathbf{r}' + \hat{v}_{xc}(\mathbf{r}). \tag{2.6}$$

Here v_{ext} is the external potential and v_{xc} is the exchange and correlation potential, which is given by the functional derivative of the exchange and correlation energy (E_{xc})

$$v_{xc}(\mathbf{r}) = \frac{\delta E_{xc}[n]}{\delta n(\mathbf{r})}. \tag{2.7}$$

In E_{xc} are contained all the non-trivial many-body contributions to the total energy. The ground-state density is obtained from the single particle wave-functions,

$$n(\mathbf{r}) = \sum_{i=1}^{N} |\psi_i(\mathbf{r})|^2. \tag{2.8}$$

Looking at the Kohn-Sham equations (equations 2.5 to 2.7), we see that they depend explicitly on the density that in 2.8 is calculated with the single particle wave-functions that in turn come from 2.5. To solve this problem we must then do it iteratively. A guess density is chosen to start and plugged into the Kohn-Sham equations that are then solved, resulting in a set of wave-functions ϕ_i. These are then used to calculate a new density and a new exchange-correlation potential. The new density and potential are again plugged into equation 2.5 and the whole process is repeated. We finish when the difference between the previous density and the next one is negligible, i.e. the system is considered converged. This whole iterative process is known as the self-consistency field (SCF) loop.

So far we have been dismissing spin considerations but it is possible to extend the concepts we have discussed so far to deal with non-colinear spin[23–25]. The biggest change is that the single-particle wavefunctions become two-component spinors,

$$\Psi_i(\mathbf{r}) = \begin{pmatrix} \psi_{i,\uparrow}(\mathbf{r}) \\ \psi_{i,\downarrow}(\mathbf{r}) \end{pmatrix}. \tag{2.9}$$

This in turn means that the KS spin density becomes a 2 × 2 Hermitian matrix,

$$n(\mathbf{r}) = \begin{pmatrix} n_{\uparrow\uparrow}(\mathbf{r}) & n_{\uparrow\downarrow}(\mathbf{r}) \\ n_{\downarrow\uparrow}(\mathbf{r}) & n_{\downarrow\downarrow}(\mathbf{r}) \end{pmatrix}, \tag{2.10}$$

as is the KS potential,

$$\hat{v}^{KS}_{\alpha\beta}(\mathbf{r}) = \hat{v}^{ext}_{\alpha\beta}(\mathbf{r}) + \hat{v}^{xc}_{\alpha\beta}(\mathbf{r}) + \hat{v}^{H}_{\alpha\beta}(\mathbf{r}). \tag{2.11}$$

In equation 2.11 α and β denote the spin indices and $v^{ext}_{\alpha\beta}(\mathbf{r})$, $v^{xc}_{\alpha\beta}(\mathbf{r})$ and $v^{H}_{\alpha\beta}(\mathbf{r})$ are respectively the external electron-ion potential, the exchange-correlation potential, and the Hartree potential. One should add that the Hartree potential is diagonal and the electronic density is the trace of the density matrix,

$$n^{Tr}(\mathbf{r}) = Tr[n(\mathbf{r})] = n_{\uparrow\uparrow}(\mathbf{r}) + n_{\downarrow\downarrow}(\mathbf{r}). \tag{2.12}$$

Having a non-colinear version of the KS system is important to our goal of simulating laser-induced demagnetization, however our problem is not entirely resolved just yet. There is still one big issue to solve, how do we find the exchange and correlation energy?

Given that we have essentially condensed all complications into this one functional it should come as no surprise that finding it is not a trivial task. In general we do not know its form. Fortunately there are numerous approximations available to tackle this problem[26, 27]. These approximations can be divided into several families of increasing complexity. The simplest of these, the local density approximation (LDA), depends only on the density and was considered originally by Kohn and Sham in the paper where they also first proposed the scheme we have been talking about[13]. Increasing the complexity a bit, we can look at functionals that depend on the gradient of the density in addition to the density itself, a family known as generalized-gradient approximations (GGAs). Other more involved families have names such as meta-GGAs and hybrid functionals. These other functionals add terms such as the Laplacian of the density, the kinetic energy density, and exact-exchange.

From among all these different functionals, the calculations in this work have been done with the LDA, so it is worth it to look into it in a bit more detail.

2.2.2 Local Density Approximation

Even though it is the simplest approximation to the exchange and correlation energy, the LDA is still a very powerful and useful tool. There is of course also a non-colinear version of the LDA, the local spin density approximation (LSDA)[23] which is the version we use throughout this work.

Despite not knowing the general form of E_{xc}, we do know it for a spin-polarized homogeneous gas of electrons (HEG). In this case it has the form

$$E_{xc}[n_{\uparrow\uparrow}, n_{\downarrow\downarrow}] = \int n^{Tr}(\mathbf{r})\epsilon_{xc}^{HEG}[n_{\uparrow\uparrow}, n_{\downarrow\downarrow}]d\mathbf{r} \tag{2.13}$$

where ϵ_{xc}^{HEG} is the exchange-correlation energy per atom for the spin-polarized HEG. The main idea behind LSDA then, is to approximate the unknown exchange-correlation energy of our system with that of a spin-polarized homogeneous gas of electrons, whose density is the same as the density of our system at each point.

The problem now is that our density, equation 2.10, is not necessarily diagonal. We can, however, perform a unitary transformation at a given point in space that diagonalises it.

$$n(\mathbf{r}) = \begin{pmatrix} n_{\uparrow\uparrow}(\mathbf{r}) & n_{\uparrow\downarrow}(\mathbf{r}) \\ n_{\downarrow\uparrow}(\mathbf{r}) & n_{\downarrow\downarrow}(\mathbf{r}) \end{pmatrix} \rightarrow \begin{pmatrix} n_{+}(\mathbf{r}) & 0 \\ 0 & n_{-}(\mathbf{r}) \end{pmatrix} \tag{2.14}$$

We can then use n_+ and n_- to calculate E_{xc} and therefor v_{xc} and transform back to obtain $v_{\alpha\beta}^{xc}(\mathbf{r})$.

The exchange-correlation energy per atom for the HEG, ϵ_{xc}^{HEG}, can be divided into two parts, the exchange contribution that can be calculated analytically and the correlation contribution that has been tabulated using Monte Carlo calculations.[28]

Despite its surprising usefulness (given how it is such a simple approximation) the LSDA does fall short sometimes. For example, it has a tendency to over-delocalize the $3d$ electrons in transition metals[14]. One way to deal with this is to use the LSDA+U method, which we present in the next section.

These shortcomings, and the existence of corrections to it, means that the LSDA is a good choice if we want to highlight the role of correlations. Combine that with the fact that most *ab initio* studies that have considered only electronic degrees of freedom (and thus neglecting the effects of phonons) have used it[11, 12], and we have the motivation for the choice of the LSDA as the exchange-correlation approximation used in this work. On a more practical note, the choice of the LSDA also presents advantages in relation to the code chosen for this work, Octopus[29], since in it, in order to use spin-orbit coupling (a relativistic correction with an important role in the demagnetization process that we present in more detail in one of the following sections) the calculations must be done with spinors, and those are only implemented with LSDA, not with GGAs or other functionals.

2.2.3 The LSDA+U method

Describing strongly correlated systems is not an easy task and the LSDA is certainly not the tool to do so. The most famous example of this is Mott insulators. These are materials that are predicted by DFT to have a metallic ground-state when in fact they are insulators[30]. The strong Coulomb interaction forces the electrons into localized atom-like orbitals which gives rise to their insulator behavior. The LSDA tends to over-delocalize these valence electrons, leading to a wrong tendency towards metallic ground-states.

Enter the Hubbard correction. The LSDA+U approach was first introduced by Anisimov and co-workers.[31–33] This method aims at a better description than the common LSDA, particularly by keeping some information about orbital localization, all while having a small impact on the overall computational cost. It is however not the only way to deal with strongly correlated systems, with other alternatives being some hybrid functionals and self-interaction-corrected local spin density approximation.[30]

In the LSDA+U approach, we essentially just add a correction to the total energy term for the orbitals of interest.

$$E_{\mathrm{DFT}+U}\left[n,\left\{n^{I,\sigma}_{mm'}\right\}\right] = E_{\mathrm{DFT}}[n] + E_{ee}\left[\left\{n^{I,\sigma}_{mm'}\right\}\right] - E_{dc}\left[\left\{n^{I,\sigma}_{m'_m}\right\}\right] \tag{2.15}$$

where $E_{DFT}[n]$ is the DFT total-energy functional, E_{ee} is the electron-electron interaction energy, and E_{dc} is the double counting term to make sure that the part of the electron-electron interaction already present in E_{DFT} is not counted twice. Both the electron-electron and the double counting terms depend on the density matrix of a localized orbital set composed of localized orbitals around the atom I, $\{\phi_{I,m}\}$. E_{dc} is also not known in the general case with several approximations existing. In the rotationally invariant form proposed by Dudarev et al. [34], which is also the one implemented in Octopus[35], we have:

$$E_{ee}\left[\left\{n^{I,\sigma}_{mm'}\right\}\right] = \frac{U}{2}\sum_{m,m',\sigma} N^{\sigma}_{m}N^{-\sigma}_{m'} + \frac{U-J}{2}\sum_{m\neq m',\sigma} N^{\sigma}_{m}N^{\sigma}_{m'}, \tag{2.16}$$

$$E_{dc}\left[\left\{n^{I,\sigma}_{mm'}\right\}\right] = \frac{U}{2}N(N-1) - \frac{J}{2}N\left(\frac{N}{2}-1\right), \tag{2.17}$$

In this $N^{\sigma} = \sum_m n^{\sigma}_{mm}$ and $N = N^{\uparrow} + N^{\downarrow}$. Combining these two expressions we get the formula for the total correction to be added to the DFT total energy.

$$\begin{aligned}E_U\left[\left\{n^{I,\sigma}_{mm'}\right\}\right] &= E_{ee}\left[\left\{n^{I,\sigma}_{mm'}\right\}\right] - E_{dc}\left[\left\{n^{I,\sigma}_{mm'}\right\}\right]\\ &= \sum_{I,n,l}\frac{U^{\text{eff}}_{I,n,l}}{2}\sum_{m,\sigma}\left(n^{I,n,l,\sigma}_{mm} - \sum_{m'} n^{I,n,l,\sigma}_{mm'}n^{I,n,l,\sigma}_{m'm}\right)\end{aligned}$$

Here I is the atom index, σ is the spin index, and n, l and m are the principal, azimuthal, and angular quantum numbers. Let us note that the total correction E_U depends only on an effective Hubbard U, $U_{eff} = U - J$, and not on U and J individually.

For a periodic system, as is the case in this work, the occupation matrices $n^{I,n,l,\sigma}_{mm'}$ are:

$$n^{I,n,l,\sigma}_{mm'} = \sum_{n}\sum_{\mathbf{k}}^{\text{BZ}} w_{\mathbf{k}} f^{\sigma}_{n\mathbf{k}}\left\langle\psi^{\sigma}_{n,\mathbf{k}} \mid \phi_{I,n,l,m}\right\rangle\left\langle\phi_{I,n,l,m'} \mid \psi^{\sigma}_{n,\mathbf{k}}\right\rangle, \tag{2.18}$$

where $w_{\mathbf{k}}$ is the weight of the k-point, $f^{\sigma}_{n\mathbf{k}}$ is the occupation of the Bloch state $\mid \psi^{\sigma}_{n,\mathbf{k}}\rangle$ and $\mid \phi_{I,n,l,m}\rangle$ are the localized orbitals that constitute the basis used to describe electron localization.

In order to obtain the set of generalized Kohn-Sham equations corresponding to this energy, equation 2.15 is minimized with respect to the wave-functions for fixed occupations:

$$\frac{\delta E_{\text{DFT}+U}\left[n, \left\{n^{I,\sigma}_{mm'}\right\}\right]}{\delta\left(\psi^{\sigma}_{i}\right)^{*}} - \frac{\delta\sum_j E_j f_j\left\langle\psi_j \mid \psi_j\right\rangle}{\delta\left(\psi^{\sigma}_{i}\right)^{*}} = 0 \tag{2.19}$$

with i and j referring to both band and k-point indexes since we are dealing with periodic systems. We can now obtain the expression of the (nonlocal) potential to be added to the DFT Hamiltonian by comparing the results from equation 2.19 to the usual Kohn-Sham equations. This potential is given by:

$$V^{\sigma}_{U}\left|\psi^{\sigma}_{n,\mathbf{k}}\right\rangle = \sum_{I,n,l}\sum_{m,m'} V^{I,n,l,\sigma}_{m,m'} P^{I,n,l}_{m,m'}\left|\psi^{\sigma}_{n,\mathbf{k}}\right\rangle \tag{2.20}$$

where we have defined:

$$V^{I,n,l,\sigma}_{m,m'} = U^{\text{eff}}_{I,n,l}\left(\frac{1}{2}\delta_{mm'} - n^{I,n,l,\sigma}_{mm'}\right) \tag{2.21}$$

$$P^{I,n,l}_{mm'} = \left|\phi_{I,n,l,m}\right\rangle \left\langle\phi_{I,n,l,m'}\right| . \tag{2.22}$$

The value of $U^{\text{eff}}_{I,n,l}$ is a parameter and must be chosen empirically in order to reproduce the desired properties.

Since the value of U is chosen by us, we do not need to limit ourselves to reproducing experimental properties. We can change the values of U used to modify the strength of the Coulomb correlations in order to gain insights into its effects. This is in fact the aim of the work presented in this thesis, as its title suggests. We are more concretely looking into the effects of correlation on the demagnetization dynamics of several systems and the Hubbard U correction is the tool that allows us to do so.

One should mention that using an empirical U is not the only option available, *ab initio* ways to calculate U have been developed and have also been implemented in the Octopus code[35, 36].

2.3 Time-dependent DFT

So far all of these considerations have dealt with the system in its ground state but if we intend to study the demagnetization process in ferromagnets, that is an inherently time-dependent process. We therefore need a time-dependent version of the theoretical tools we have been discussing.

That was precisely the problem tackled by Runge and Gross in 1984 when they developed a time-dependent version of DFT[37]. In it they present the time-dependent version of the Hohenberg-Kohn theorem, the Runge-Gross theorem. Analogously to the ground-state case, there is also a one-to-one mapping between the time-dependent external potential $v_{ext}(\mathbf{r}, t)$, such as one created by an external laser field or by the movement of the nuclei, and the time-dependent density $n(\mathbf{r}, t)$, evolving from a given initial state, up to a purely time-dependent constant in the potential. If two potentials differ only by a time-dependent constant $C(t)$, their corresponding wave-functions will differ by a purely time-dependent phase factor, $e^{-i\alpha(t)}$ and so their densities will be identical. The wave-function can therefore be seen as a functional of the density and the initial state:

$$\Psi[t] = e^{-i\alpha(t)}\Psi[n, \Psi_0](t). \tag{2.23}$$

Expectation values of Hermitian operators are also not affected by this time-dependent constant since the phase cancels out, meaning they are also functionals of the density and the initial state:

$$O[n, \Psi_0] = \langle \Psi[n, \Psi_0](t) | \hat{O}(t) | \Psi[n, \Psi_0](t) \rangle \tag{2.24}$$

Having established that there is a one-to-one correspondence between the time-dependent density and the external potential, and that expectation values are functionals of the time-dependent density, one problem still remains, as it did in the ground-state case, how to actually calculate these quantities. For that, we turn again to the Kohn-Sham formulation.

One particular case of potential is $v_{KS}[n, \Psi_0](\mathbf{r}, t)$ and so the RG theorem also applies and we can substitute the interacting system with a non-interacting one that reproduces its density $n(\mathbf{r}, \mathbf{t})$, starting from an initial state Ψ_0. The density of the non-interacting system, which mirrors the interacting one, is given by

$$n(\mathbf{r}, t) = \sum_{i=1}^{N} |\psi_i(\mathbf{r}, t)|^2 \tag{2.25}$$

where the orbitals $\psi_i(\mathbf{r}, t)$ are obtained from the time-dependent Kohn-Sham equations

$$i\frac{\partial}{\partial t}\psi_i(\mathbf{r}, t) = \left[-\frac{1}{2}\nabla^2 + \hat{v}_{KS}(\mathbf{r}, t)\right]\psi_i(\mathbf{r}, t) \tag{2.26}$$

The Kohn-Sham potential is

$$\hat{v}_{KS}[n, \Psi_0](\mathbf{r}, t) = \hat{v}_{ext}[n, \Psi_0](\mathbf{r}, t) + \hat{v}_{xc}[n, \Psi_0](\mathbf{r}, t) + \int \frac{n(\mathbf{r}', t)}{|(\mathbf{r}) - (\mathbf{r}')|} d\mathbf{r}'. \tag{2.27}$$

In equation 2.27, analogous to equation 2.6, the first term, v_{ext}, is the external potential, that includes the interaction of the electrons with the nuclei that may move as well as any other time-dependent external field like, for example, one created by a laser pulse. The last term is the time-dependent Hartree potential describing the Coulomb interaction and v_{xc} is the exchange-correlation term and must be approximated, as in the static case.

One characteristic that is exclusive of the TDKS procedure and has no analogue in the static case is the dependence on the initial state Ψ_0.

2.3.1 Adiabatic LDA

The simplest, and most popular, approximations used are adiabatic approximations[38]. In this class of functional, the functional's memory, i.e. its dependence on the history of the density, is ignored.

The time-dependent version of the local density approximation is the same as the static one but with the density evaluated at the time-dependent density.

$$\hat{v}_{xc}^{ALDA}(\mathbf{r},t) = \hat{v}_{xc}^{HEG}(\mathbf{r})|_{n=n(\mathbf{r},t)} \tag{2.28}$$

The ALDA can be considered an appropriate approximation to systems that vary slowly in both time and space, yet it turns out to be better than that and produces reasonable results for systems far from this regime[21].

The same approach of evaluating the time-independent functional at the time-dependent density can be extended to other static functionals (for example GGAs) to obtain an adiabatic version of them (AGGAs).

We should point out that adiabatic functionals are not the only class of functionals available for use in TDDFT, other alternatives like orbital-dependent functionals exist[38]. In fact, a recent study[16] has shown that memory effects usually ignored are of great importance when describing light-induced demagnetization and lead to bigger demagnetization values than those observed in calculations without memory effects.

2.3.2 Time propagation

The time-dependent Schrödinger equation can be reformulated as [39]

$$\psi(t) = \hat{U}(t,0)\psi_0 = \mathcal{T}exp\left\{-i\int_0^t \hat{H}(\tau)d\tau\right\}\psi_0 \tag{2.29}$$

where $\mathcal{T}exp$ is the time-ordered exponential.

In this section, we present the numerical approximations needed to apply the propagation in equation 2.29, in particular the ones used in the calculations we performed in this work and which we present in the next chapters.

The first step when applying 2.29 in practice is to divide the total propagation from the initial time $t_0 = 0$ to the final time t into several smaller propagations. This is possible since

$$\hat{U}(t_2,t_1) = \hat{U}(t_2,t_3)\hat{U}(t_3,t_1), \tag{2.30}$$

that is, propagating from t_1 to t_2 is the same as propagating form t_1 to an intermediary time t_3 and then from t_3 to the final time t_2. The full propagator will then be

$$\hat{U}(t,0) = \prod_{i=0}^{N-1} \hat{U}(t_i + \Delta t, t_i), \tag{2.31}$$

where $t_0 = 0$, $t_N = t$, and Δt is the time-step each propagation covers and we set it to be the same for all propagations. The choice of the time step is an important one in practice to guarantee the convergence of the calculations.

If the Hamiltonian was not time-dependent, the propagator would have a quite simple form, it would just be $exp\{-i\Delta t\hat{H}\}$. That is obviously not the case when we are dealing with laser excitations. However, since we divided the original interval into many smaller ones we can consider that in this small interval Δt the time-dependence is small and so we approximate the propagator by a simple exponential with the Hamiltonian taken at a certain time τ in the interval. This is indeed the case in what is perhaps the simplest approximation to the propagator, the exponential midpoint rule, where the Hamiltonian is taken at the midpoint of the interval considered,

$$\hat{U}_{EM}(t+\Delta t, t) = \exp\{-i\Delta t\hat{H}(t+\Delta t/2)\}. \tag{2.32}$$

The propagation should be time-reversible, that is, propagating forwards from the initial state should be the same as propagating backwards from the final state. This is not the case in the systems we investigate, since the presence of spin-orbit coupling breaks time-reversal symmetry[40]. Nonetheless it is still an important property in the general case. Any propagator we use should respect time-reversal symmetry when no term that breaks it is present. We can use time-reversibility explicitly and propagate the initial state $\psi(t)$ half of the interval ($\frac{\Delta t}{2}$) forward and the final state $\psi(t+\Delta t)$ the same amount backwards and we should arrive at the same state. That is,

$$\exp\left\{-i\frac{\Delta t}{2}\hat{H}(t)\right\}\psi(t) = \exp\left\{i\frac{\Delta t}{2}\hat{H}(t+\Delta t)\right\}\psi(t+\Delta t). \tag{2.33}$$

Upon rearranging we get the propagator

$$\hat{U}_{ETRS}(t+\Delta t, t) = \exp\left\{-i\frac{\Delta t}{2}\hat{H}(t+\Delta t)\right\} \times \exp\left\{-i\frac{\Delta t}{2}\hat{H}(t)\right\}. \tag{2.34}$$

This is called enforced time reversal symmetry (ETRS).

This propagator depends on the Hamiltonian at t and $t+\Delta t$. This is a problem because $\hat{H}(t+\Delta t)$ depends on the wave-functions at $t+\Delta t$, $\psi_i(t+\Delta t)$, which we obviously do not know *a priori*, since they are what we are trying to find in equation 2.29. We can solve this in two ways. We can solve it iteratively, that is we extrapolate $\hat{H}(t+\Delta t)$, use it to create the propagator in equation 2.34 and get $\psi(t+\Delta t)$. We then use $\psi(t+\Delta t)$ to recalculate $\hat{H}(t+\Delta t)$ and repeat the whole process (minus extrapolation) until self-consistency is reached. For small time-steps, doing only the first step of the iterative cycle, the extrapolation, can be enough. The other option then is to move forward using the extrapolated Hamiltonian. This is known as the approximate time reversal symmetry (AETRS) and it was the propagator used in the calculations done in this thesis. In Octopus the extrapolation is done via a second-order polynomial, that is, by using the Hamiltonian in the current plus in the two previous steps. This is about it 40% faster than the implementation for ETRS. AETRS is generally the best compromise between accuracy and speed.

There are countless other propagators one could use, not surprisingly given that the time-dependent KS equations can be viewed as an example of a system of initial value ordinary differential equations and thus subject to a great deal of interest throughout history. Many of these propagators are available in Octopus[39, 40], but since they were not the ones used in this work, we do not go into further detail on them.

We are not yet done with computational details regarding the time propagation however. One question still remains. How do we calculate the exponential of an operator?

The exponential of a matrix $\hat{A}$ is defined as:

$$\exp\left\{\hat{A}\right\} = \sum_{n=0}^{\infty} \frac{1}{n!}\hat{A}^n. \tag{2.35}$$

Obviously, we can just approximate the exponential by truncating the sum in equation 2.35 but this is far from the optimal way to do it. In our calculations we employ the Lanczos method which allows for longer time-steps, according to the Octopus variable reference.

In truth, we are not interested in the exponential of a matrix, $\exp\left\{\hat{A}\right\}$, but in its effect on a vector v, $\exp\left\{\hat{A}\right\}v$. With the Lanczos method we iteratively generate a basis $\{v_i\}_{i=1}^m$ such that

$$\hat{A}\hat{V}_m = \hat{V}_m\hat{H}_m + h_{m+1,m}v_{m+1}e_m^T \tag{2.36}$$

where $\hat{V}_m = [v_1, ..., v_m]$ is an orthonormal basis of the Krylov space

$$K_m = \mathtt{span}\{v, \hat{A}v, ..., \hat{A}^{m-1}v\}, \tag{2.37}$$

$\hat{H}_m$ is an $m \times m$ Hessenberg matrix (and which forms the upper left part of $\hat{H}_{m+1}$), and e_m is the mth unit vector in $\mathcal{C}^m$. In Octopus, the maximum dimension of the basis $\{v_i\}_{i=1}^m$ must be given. In our case it was 16. The iterative process is done until a tolerance is reached, which in our case had the same value as the default in Octopus, 10^{-5}. One can then prove that[41]

$$\exp\left\{\hat{A}\right\}v \approx \hat{V}_m \exp\left\{\hat{H}_m\right\}e_1. \tag{2.38}$$

We have reduced the problem from calculating the exponential of a large sparse matrix

$\hat{A}$, to a small dense matrix $\hat{H}_m$. The calculation of $\hat{H}_m$ can then be done in a number of ways[42].

2.4 Our calculations

In the end, the time-dependent Kohn-Sham equations, within the adiabatic approximation, that are going to be propagated in all calculations presented in this work are:

$$i\hbar\frac{\partial}{\partial t}|\psi_{n,\mathbf{k}}(t)\rangle = \left\{\frac{(\hat{\mathbf{p}}+\mathbf{A}(t)/c)}{2} + \hat{v}_{\text{ext}} + \hat{v}_{\text{H}}[n(\mathbf{r},t)] + \hat{v}_{\text{xc}}[n(\mathbf{r},t)] + \hat{v}_{\text{U}}\right\}|\psi_{n,\mathbf{k}}(t)\rangle, \tag{2.39}$$

where $|\psi_{n,\mathbf{k}}\rangle$ is a Pauli spinor representing the Bloch state with the band index n at the point $\mathbf{k}$ in the Brillouin zone, $\hat{v}_{\text{ext}}$ is the electron-ion potential, $\mathbf{A}(t)$ is the external vector potential describing the laser field, $\hat{v}_{\text{H}}$ is the Hartree potential, $\hat{v}_{\text{xc}}$ is the exchange-correlation potential given by the adiabatic LSDA and lastly $\hat{v}_{\text{U}}$ is the potential coming from the DFT+U correction.

For most atoms, such as those considered in this work, the core electrons do not play an important part in the electronic properties of the system and so we can treat them and the nucleus as an inert ion, with $\hat{v}_{\text{ext}}$ being described by a pseudopotential. The pseudopotential replicates the effective interaction between the outer electrons and the nucleus screened by the core electrons. This greatly reduces the number of electrons we have to deal with, thus further simplifying our problem.

Octopus comes with an array of different pseudopotential sets, at both the LSDA and GGA levels. Of these, two, labeled by the code as `hgh_lda` and `hgh_lda_sc`, also describe the SOC, as we shall discuss in more detail in the next subsection. These are the non-semicore and semicore versions of the Hartwigsen-Goedecker-Hutter LDA pseudopotentials[43], a semicore pseudopotential being one where the distinction between core and valence electrons is not clear and so fewer electrons are treated as part of the core. The non-semicore version proved to give wrong densities of states (DOS) for the ferromagnets studied (see figure 2.1). For this reason, all calculations presented in the next chapters have been done with the semicore version of the pseudopotentials.

2.4.1 Spin-orbit coupling

The SOC is a relativistic correction caused by the interaction between the electron spin magnetic moment and the orbital angular momentum. As we said previously, spin-orbit mediated spin-flip transitions are among the possible culprits for laser-induced ultrafast

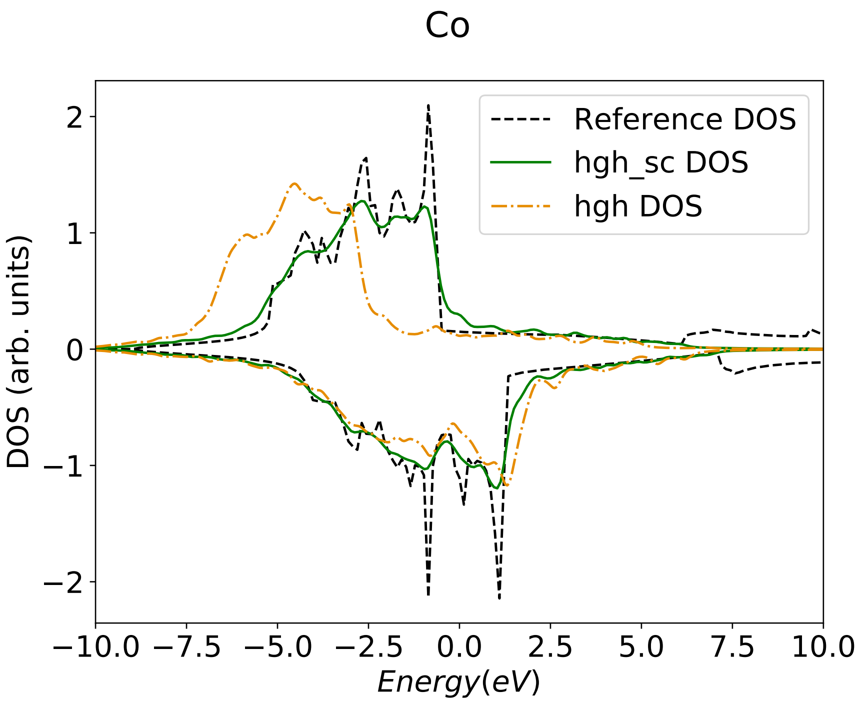

Figure 2.1: Comparison of the Co majority and minority DOS calculated using the semicore (`hgh_sc`) and non-semicore (`hgh`) versions of the Hartwigsen-Goedecker-Hutter LDA pseudopotentials as implemented on the Octopus code version. The reference density is from the materials project database.[44]

demagnetization, since it allows transitions between spin states[7]. Thus it is important that we account for it in our calculations.

The SOC term has the form

$$\hat{H}_{SO} = \frac{1}{4c^2}\sigma \cdot \left[\nabla v_{ext} \times \hat{\mathbf{p}}\right] \tag{2.40}$$

where v_{ext} is the electron-ion potential and σ are the Pauli matrices.

The SOC does not enter directly in this form in the Hamiltonian in Octopus. The SOC is taken into account in some of the pseudopotentials available, the `hgh_lda` pseudopotentials[43], as we have referenced above. These pseudopotentials reproduce fully relativistic all-electron calculations. That is, for each of the atoms available (H to Rn) the authors of ref. [43] solved the two-component Dirac equation and then fitted their parameters to it.

In the end, their potential has the form

$$V\left(\mathbf{r}, \mathbf{r}'\right) = V_{\text{loc}}(r)\delta\left(\mathbf{r} - \mathbf{r}'\right) + \sum_l V_l\left(\mathbf{r}, \mathbf{r}'\right) + \Delta V_l^{\text{SO}}\left(\mathbf{r}, \mathbf{r}'\right)\hat{\mathbf{L}} \cdot \hat{\mathbf{S}}. \tag{2.41}$$

In equation 2.41, V_{loc} and V_l represent, respectively, the local and non-local parts of the potential and V_l^{SO} represents the spin-orbit part of the potential. This is of special interest to us because it means that the SOC is parameterized independently of the rest and so its strength can be scaled when used by a program like, say, Octopus. This will prove of interest in chapter 5.

Additionally, just for the sake of completeness, the SOC part of the potential has the form

$$\Delta V_l^{\mathrm{SO}}(\mathbf{r},\mathbf{r}') = \sum_{i=1}^{3}\sum_{j=1}^{3}\sum_{m=-l}^{+l} Y_{l,m}(\hat{\mathbf{r}}) p_i^l(r) k_{i,j}^l p_j^l(r')\, Y_{l,m}^*(\hat{\mathbf{r}}'), \tag{2.42}$$

where $Y_{l,m}$ are the spherical harmonics, $p_i^l(r)$ are projectors with a Gaussian form (for more details see ref. [43]) and $k_{i,j}^l$ are the parameters.

Chapter 3

Ferromagnets

Now that we have laid out all the necessary theoretical details in the previous chapter, now that we know what TDDFT calculations of laser-induced ultrafast demagnetization actually entail, we can move on to the calculations themselves.

In this chapter, we start applying laser fields to magnetic materials to simulate how their magnetic moments respond. We start by looking at the most famous class of magnetic materials, ferromagnets (as one could probably have guessed given this chapter's name). More specifically we will start with bulk elemental $3d$ transition metals Fe, Co, and Ni. These materials are a good place to start since there have been already multiple studies into different facets of their light-induced ultrafast demagnetization we can use as a reference point.[9, 11, 16] From a computational point of view bulk elemental ferromagnets are also a good starting point given that they have only one atom in the unit cell and so the calculations run faster. There is also yet another good reason to choose Fe, Co, and Ni: the LSDA, the approximation most commonly used in ultrafast demagnetization studies, is known to not be able to accurately describe their electronic structure[14]. This gives us a chance to look at the impact of electron correlation on light-induced demagnetization and how important a correct description of the initial state is.

To do so we start by laying out all the studies done to guarantee the proper convergence of the calculations. Having established that our calculations are well converged we move on to the demagnetization calculations and present our results at the LDA and LDA+U level, and relate the findings to the system's electronic structure. With this relationship in mind, we then investigate the role that several laser parameters (intensity, fluence, duration, frequency) play in the demagnetization dynamics of the system.

The systems studied here were body-centered cubic (BCC) iron with a lattice parameter of 2.856 Å, face-centered cubic (FCC) cobalt with a lattice parameter of 3.544 Å, and FCC nickel with a lattice parameter of 3.520 Å. All calculations in this work were done with the real-space time-dependent DFT code Octopus.

3.1 Ground state convergence

It is of course of the utmost importance that our calculations are well converged, otherwise they are meaningless. The results of a DFT calculation with Octopus depend on a number of parameters, some with a bigger impact than others, and we must guarantee that our choices lead to correct results. One obvious example of a question we must consider in practice is when is self-consistency reached? DFT is an iterative process, and we have said previously in chapter 2 that we exit this iterative process when the density is converged. But what do we consider as a converged density? Octopus defaults to exiting the SCF loop once the relative error of the density is smaller than 10^{-6} for two consecutive iterations. This relative error is defined as

$$\epsilon_{rel} = \frac{1}{N}\epsilon_{abs} \tag{3.1}$$

where N is the total number of electrons and ϵ_{abs} is the absolute error on the density defined as

$$\epsilon_{abs} = \int |n_{out}(\mathbf{r}) - n_{inp}(\mathbf{r})| \, d\mathbf{r}. \tag{3.2}$$

This is also the criteria we use.

Another parameter of great importance is the spacing. Octopus is a real-space code which means that quantities such as the density are represented on a real-space grid with each point separated by a certain spacing. One may get the density to converge to a certain threshold but if the grid is too coarse the density, and therefore all related properties one might be interested in, will not be very accurate. Obviously the finer the mesh the better the results but also the more demanding the computations. It is necessary then to find what is the smallest real-space grid that still produces correct results, that offers the best compromise between accuracy and speed.

We performed several calculations to guarantee that the ground-state was converged with regards to the spacing and the uniform **k**-point grid used and those results are presented in this section. By converged ground-state we mean that several properties of interest, the total energy, the magnetization, the DOS, and the actual demagnetization dynamics, do not change considerably when we increase the number of points in either the real-space or **k**-point grid.

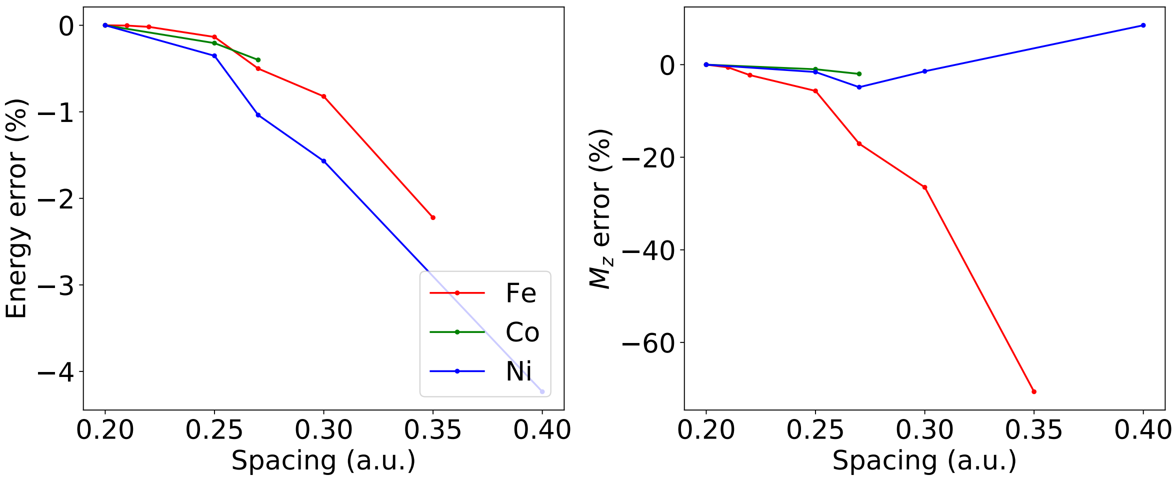

Figure 3.1: Convergence of the total energy (left panel) and the z component of the magnetization (right panel) with regards to the spacing used. These calculations were all done with a $4 \times 4 \times 4$ **k**-point grid for all systems.

3.1.1 Total energy and magnetization convergence

We start by looking at the total energy and the z component of the magnetization, as that is essentially the direction in which the magnetization points.

For their convergence with the spacing see figure 3.1. In it we compare the ground-state total energy (and the z component of the magnetization), calculated with different values for the grid spacing while maintaining all other variables the same, to the most accurate results we have, those with the smallest spacing. This is why both graphs tend to zero as we move left (to smaller spacing values), as those were the calculations used as benchmarks. While a smaller value for the spacing means more accurate results it also means more demanding calculations and so we search for the largest spacing possible that still produces satisfactory results. It is apparent that the magnetization is much harder to converge than the total energy, necessitating a much smaller spacing to achieve similar error values. In fact, for Fe, the energy with largest spacing used (0.35 a.u.) has a relative error of 2.22 % and we need to go all the way down to a spacing of 0.22 a.u. to find a similar error in the magnetization (2.27%). The magnetization is so much harder to converge that the reason there are so few points for Co is that for larger spacing values the calculations do not converge to the correct ground-state, we obtain a non-magnetic state.

Next, the same quantities were converged with regards to the **k**-point grid used to sample the Brillouin zone along each axis. We now keep the spacing fixed and increase the size of the **k**-point grid. The values chosen for the spacing were the largest ones that still produced a relative error for the magnetization of the order of 1 % in figure 3.1 (0.21 a.u. for Fe and

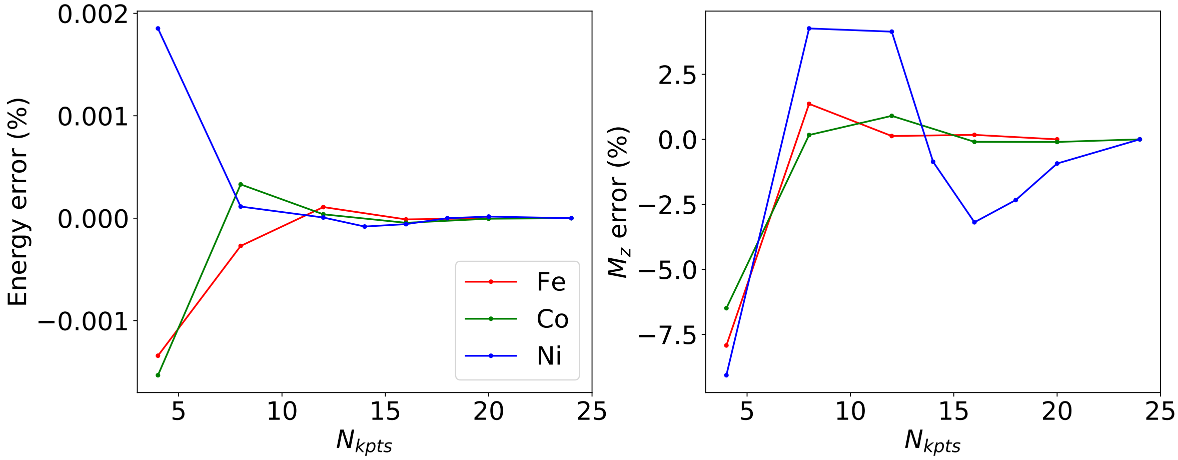

Figure 3.2: Convergence of the total energy (left panel) and the z component of the magnetization (right panel) with regards to the $N_{kpts} \times N_{kpts} \times N_{kpts}$ **k**-point grid used. These calculations were all done with a constant spacing of 0.21 a.u. for Fe and 0.25 a.u. for both Co and Ni

0.25 a.u. for both Co and Ni). Figure 3.2 displays these results.

The more accurate results are now on the right side, with the denser **k**-point grids, and so those are the ones against which the error values displayed are defined. Both the total energy and the magnetization vary a lot less with the density of the **k**-point grid than with the value of the spacing, although the magnetization still changes quite a bit. We can consider the magnetization converged for our purposes if it has a relative error smaller than 1 % which happens with an N_{kpts} value of 12, 8, and 14 for Fe, Co, and Ni respectively. The energy on the other hand can be considered converged with all of the grids used.

3.1.2 Density of states convergence

The total energy and the z component of the magnetization are not the only quantities we have access to. They are not the only ways we have to assess the convergence of the ground-state. Another way the convergence of the ground state was guaranteed was by looking at the density of states (DOS). This is depicted for Fe in figure 3.3. The left panel shows the DOS calculated with different values of spacing but with a fixed $4 \times 4 \times 4$ **k**-point grid, as was done in figure 3.1. And the right panel shows the DOS calculated with different **k**-point grids but a constant value for the spacing of 0.111 Å (0.21 a.u.), like the calculations presented in figure 3.2. As in the case of the energy and the magnetization, the DOS is also much more sensitive to the spacing than it is to the **k**-point grid. The DOS with the largest spacing considered is completely different to those calculated with smaller values whereas in the **k**-point grid the sparsest grid only exhibits some small though significant differences

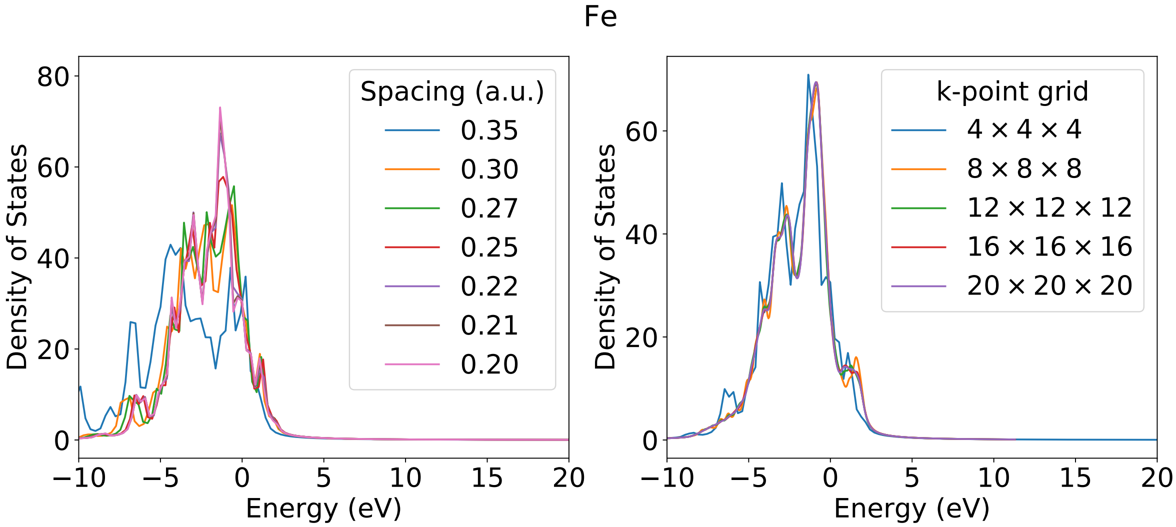

Figure 3.3: Convergence of the density of states of Fe with regards to the spacing (left panel) and to the **k**-point grid used (right panel). In both panels 0 corresponds to the Fermi energy.

when compared to the DOS with denser grids.

In figure 3.4 we show the same plots but for Co. The changes in the DOS with the spacing are not as wild here as in figure 3.3, which is expected as we could not use values for the spacing as large as those in the Fe case, but the **k**-point case is far more interesting. While previously it seemed like the ground-state was converged with an $8 \times 8 \times 8$ **k**-point grid, as the relative error in both the energy and magnetization was under 1%, figure 3.4 makes it clear we can not consider it as such. The DOS with that **k**-point grid exhibits some noticeable deviations from the DOS with denser grids.

A similar figure of the convergence of the DOS for the remaining case of Ni is shown in appendix A.

3.1.3 Demagnetization convergence

Finally, the quantity we are really interested in, the one that is most important to be well converged, is the demagnetization, i.e. how the magnetization changes in time under the influence of a laser field.

To confirm that the dynamics were converged, small propagations, just 3 fs, were performed using different values for the spacing and **k**-point grid. These results for Ni are shown in figure 3.5.

It is clear that the results are well converged. As with the ground state properties we looked at before, the demagnetization dynamics are easier to converge with the **k**-point grid than with the spacing. Going from a $14 \times 14 \times 14$ **k**-point grid (solid red line) to a $24 \times 24 \times 24$

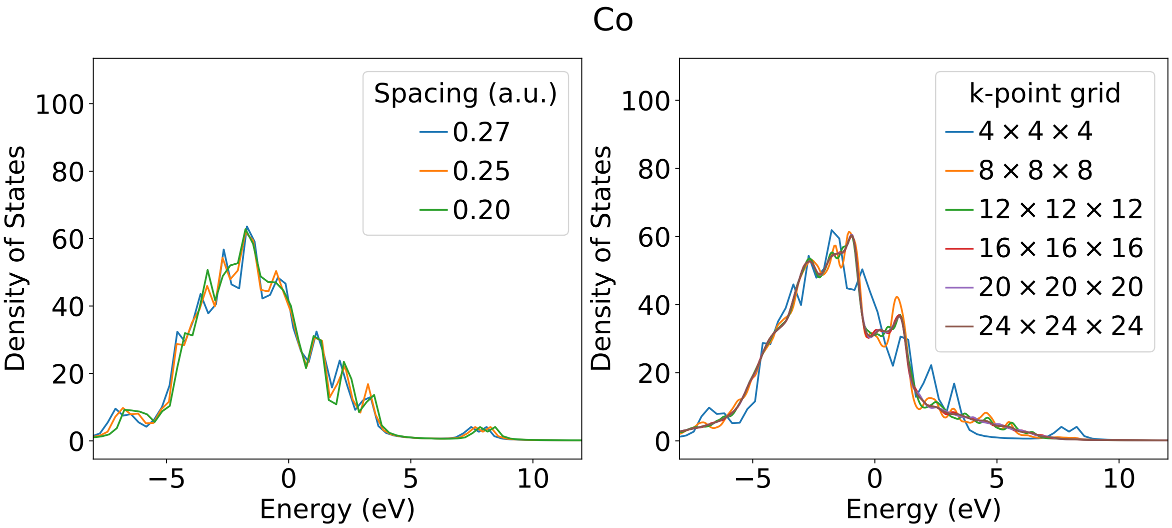

Figure 3.4: Convergence of the density of states of Co with regards to the spacing (left panel) and to the **k**-point grid used (right panel). In both panels 0 corresponds to the Fermi energy.

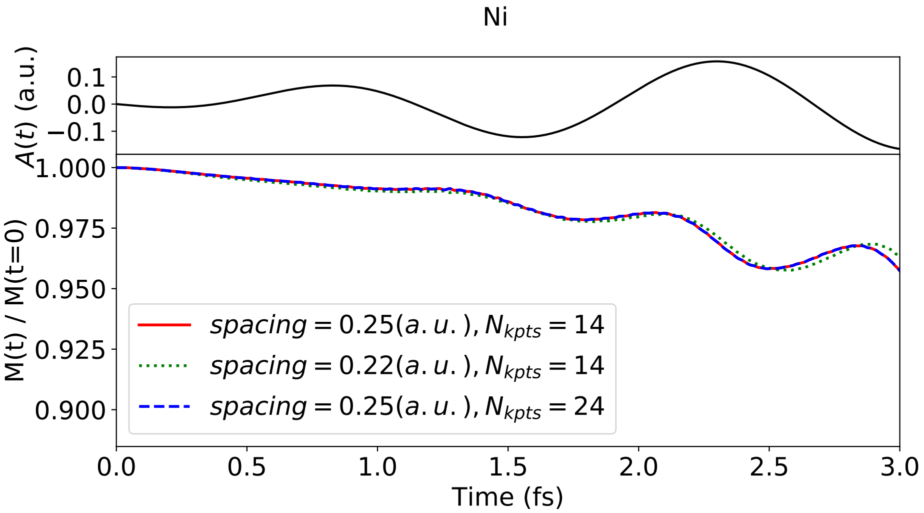

Figure 3.5: Short propagation of the relative magnetization in Ni with different parameters. The upper panel shows the vector potential **A**(t) of the laser pulse and the lower panel the various dynamics. The results are nearly the same with different spacing and **k**-point grid which means the calculations are well converged.

k-point grid (dashed blue line) while using the same spacing produces no visible changes in figure 3.5. Varying the spacing, however, going from a spacing of 0.25 a.u. (0.132 Å) in the solid red line to a spacing of 0.22 a.u. (0.116 Å) in the dotted green line, does produce some changes. These are barely noticeable though and so it is safe to say that our calculations are also converged with respect to spacing.

Taking all this information for all the quantities of interest in all of the systems considered we can finally consider the ground-state converged with a uniform spacing of 0.111 Å and a $12 \times 12 \times 12$ **k**-point grid to sample the Brillouin zone for BCC iron, a spacing of 0.132 Å and a $16 \times 16 \times 16$ **k**-point grid for FCC cobalt, and a spacing of 0.132 Å and a **k**-point grid of $14 \times 14 \times 14$ for FCC nickel.

3.2 LSDA+U calculations

With the ground state properly converged we can now move on to the time-dependent calculations.

The laser pulse used to induce the demagnetization dynamics has the form

$$f(x, y, z)\cos(\omega t)g(t). \tag{3.3}$$

$f(x, y, z)$ gives the field's polarization and spatial dependence. In our case, the field is polarized along the x-axis, perpendicular to the magnetic moment direction, and since we employ the dipole approximation, that is we discard the spatial variation of the electric field as the wavelength is much greater than the atomic distances, our field is constant in space. The central frequency of our field, ω, has a carrier photon energy of 2.712 eV which corresponds to a wavelength of 457.1 nm. As we can see the use of the dipole approximation is completely justified.

The pulse is enveloped by a cosinusoidal envelope $g(t)$ with the form

$$g(t) = E_0 \cos(\frac{\pi}{2}\frac{t - 2\tau_0 - t_0}{\tau_0}). \tag{3.4}$$

E_0 is the electric field amplitude that relates to the field's intensity, the more common way to describe its strength, by

$$I(t) = \frac{c}{8\pi}E^2(t). \tag{3.5}$$

The pulse we use has a peak intensity of 10^{15} W/cm^2. The duration of the pulse is set by t_0 and τ_0 since $g(t) = 0$ if $|t - t_0| > \tau_0$. In our case, t_0 and τ_0 are both set to 3 fs and so our pulse lasts for 6 fs, peaking at 3 fs. This means that our laser field is shorter and more intense than most laser pulses typically used in experiments. This is done for practical reasons as a short laser pulse means a smaller computation time. The higher intensity offsets the shorter length of the pulse in terms of the energy it caries and it also ensures that our calculations produce a significant amount of demagnetization since, as we discussed in chapter 1, the LSDA is known to produce demagnetization values far lower than the experimental ones. That being said some recent experiments[45] have used pulses with full width at half maximum (FWHM) as short as 4 fs and with an intensity of $4 \times 10^{12}\mathrm{W/cm^2}$ so the laser pulses used here are not completely unrealistic.

The demagnetization calculations were done at the LSDA level, with and without Hubbard U corrections of different intensities. The values of U_{eff} applied to the d orbitals of the metals studied were of 2 and 4 eV for Fe, 1.6 and 3.2 eV for Co, and 1.2 and 2.4 eV for Ni. At first, values for U_{eff} were chosen from the typical values in the literature[46–48] and subsequently other values were chosen that are either half or double the original ones in order to investigate how changes in the magnitude of the U correction impact the demagnetization dynamics.

3.2.1 Effects of U on ground-state properties

Before looking at the time-dependent results let us see some interesting effects of the Hubbard U on ground-state properties of the systems. The Hubbard U introduces a shift in the d orbitals of the metal, changing considerably its DOS. These changes with U can be seen for Fe, compared to experimental data [49], in figure 3.6.

We see a fair agreement with experiment at the LDA level but as we apply the U correction the theoretical peaks shift away from the experimental ones, especially for the majority spins. It is important to note as well that the two spin channels are affected in opposite ways. The majority spin peaks shift to lower energies while the minority spin ones shift to higher energies.

And so we seem to be in a predicament, the correction we employ does not actually correct much. A few thoughts on that. Firstly, the example we chose to show in figure 3.6 (Fe) is where the discrepancy is most drastic. The impact of the Hubbard U on the DOS of both Co and Ni (which can be seen in appendix B) is much smaller, though the LSDA results are still closer to the experimental data than the LSDA+U ones are. Secondly, the DFT+U approach is not the optimal approach to represent the ground state DOS of transition metals. Were that our aim and more sophisticated methods, such as DMFT, or at least more carefully selected values of U would have been used. That being said it has been shown repeatedly that LSDA+U can improve the description of the electronic structure of

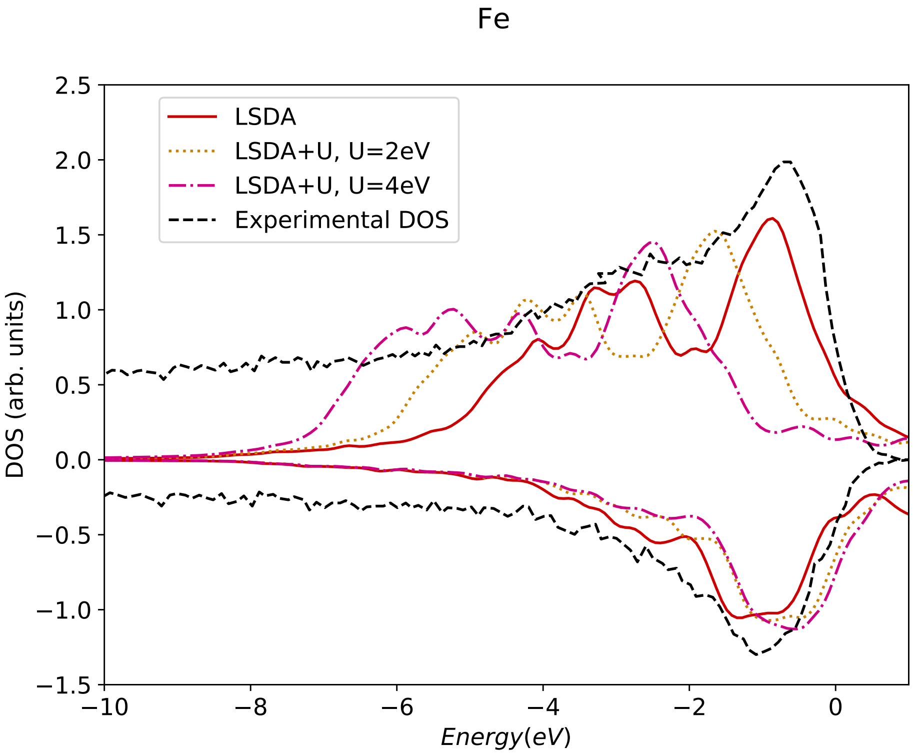

Figure 3.6: Comparison of the Fe majority and minority DOS calculated using the LDA and different U values with experimental data.[49]

Table 3.1: Ground state magnetic moments calculated versus experimental values (in Bohr magnetons per atom). The values of U used are described in the main text and $U_2 > U_1$

	$LSDA$	U_1	U_2	exp.
Fe	2.33	2.61	2.72	2.12 [52]
Co	1.68	1.76	1.77	1.75 [53]
Ni	0.659	0.683	0.688	0.61 [54]

$3d$ materials.[50, 51] Finally our aim is not really to carefully reproduce experimental results but instead to study how a change in the description of electronic correlation affects the demagnetization dynamics. For that, a static U provides a simple tool with significant effects on ground-state properties (and on the demagnetization dynamics as we will see further on).

Another example of a ground-state property affected by the addition of the Hubbard U is the magnetic moment. Its values, obtained for each system by integrating the magnetization density in the unit cell, are shown in table 3.1. With the exception of Co, the ground state magnetic moment calculated is greater than the experimental values and becomes even greater with the use of the Hubbard U. This increase is to be expected since the effect of the U correction is to shift the majority spin DOS down and the minority spin DOS up, as discussed previously and shown in figure 3.6. This increases the number of majority spin states occupied and lessens the number of minority spin ones and therefore the magnetic moment will increase. The change of the magnetic moment with U is much greater for Fe than for the other metals which is also to be expected for the same reasons as the shift caused by the Hubbard U is much more significant in this case as well.

3.2.2 Demagnetization dynamics with U

Now that we have dealt with the effects of the Hubbard U correction on ground-state properties we can finally move on to the effects we were originally interested in, those on the dynamics. The dynamics of the magnetic moments for the LSDA and LSDA+U cases are presented in Fig. 3.7. The first thing we observe is that demagnetization occurs only while the laser pulse is present (after that the magnetization essentially oscillates around a constant), unlike in experiments where most of the demagnetization is measured in fact after the laser field is turned off.[55, 56] The amount of demagnetization observed is also quite smaller than that of experimental results, with Fe demagnetizing around 9 %, Co around 6 %, and Ni around 8 % in the LSDA case whereas in the previously mentioned experiments Ni was measured to demagnetize at least 30 %, and this is while using a laser field quite less powerful than in our case. Although different from experiments our results are in line with other similar theoretical works where only electronic effects have been considered, in both the magnitude and period where the demagnetization is observed.[10, 16, 57]

We should note, on the more technical side of things, that the ground state magnetic moments whose dynamics are depicted in figure 3.7 are not calculated by integrating magnetization density in the entire unit cell like in table 3.1 but are instead calculated by integrating in spheres centered around each atom. Since there is only one atom in the unit cell for the system we study here this should not make much of a difference. Turns out that the version of Octopus we were using, when dealing with 3D materials with only one atom in the unit cell, had a bug where the radius of these spheres, which should be half of the distance between neighbouring atoms, ends up being only half of that, i.e. a quarter of the distance between neighbouring atoms. The spheres used to calculate the magnetic moments in our calculations thus had a radius of 0.618 Å for Fe, 0.627 Å for Co, and 0.622 Å for Ni. Unfortunately, we only noticed this problem too late, after the time-dependent calculations had already been done with the shorter radius but on the brighter side this turned out to not have a meaningful effect on our investigation, especially because we are not really interested in extremely precise quantitative results for certain properties but more so in the qualitative effects of the theory level used.

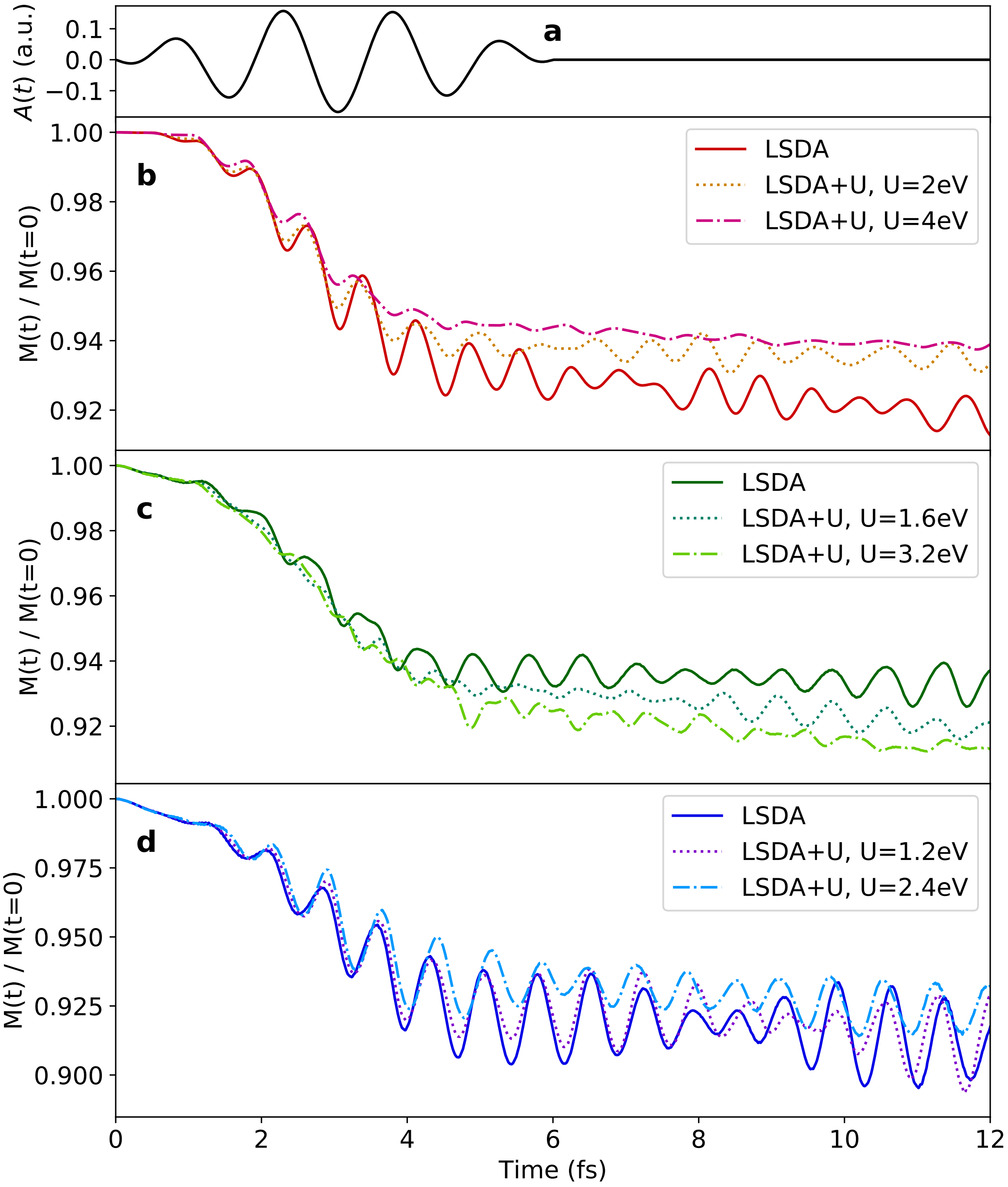

Figure 3.7: Demagnetization of elemental transition metals. From top panel to bottom panel, we have a) the vector potential $\mathbf{A}(\mathrm{t})$ of the laser pulse, the magnetization dynamics of b) Fe, c) Co, and d) Ni with standard LSDA and using LSDA+U. The parameters of the laser pulse are given in the main text.

Table 3.2: Ground state magnetic moments of Ni calculated with two different radii (in Bohr magnetons per atom).

	0.622 Å	1.244 Å
Ni	0.572522	0.679199

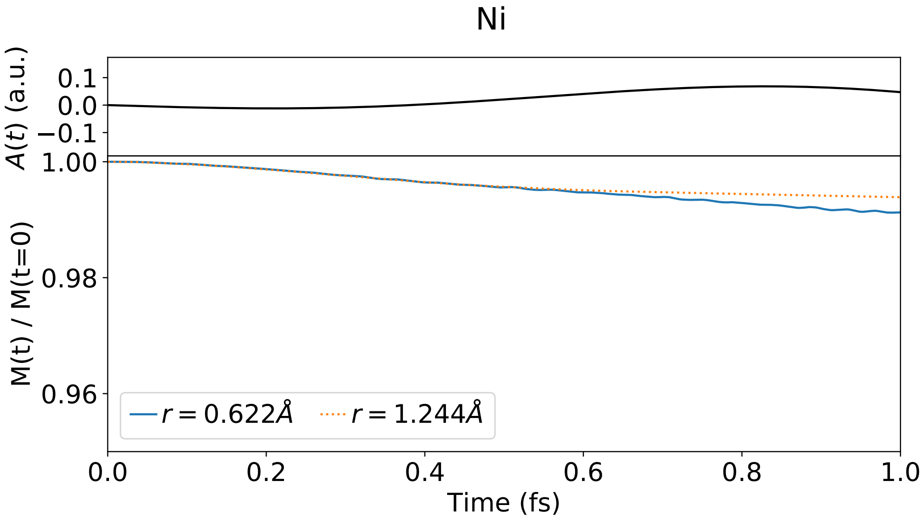

Figure 3.8: Demagnetization dynamics for Ni in a short propagation with two different radii being used to calculate the magnetic moments.

Take Ni for example. If we recalculate the magnetic moment at the LSDA level using this time a local sphere with a radius of 1.244 Å (i.e. half of the distance between two neighbouring atoms and double of what we originally used) and compare it to the magnetic moment calculated with the original radius of 0.622 Å (table 3.2) we find that the value of the magnetic moment increases by around 19%. This is not an inconsequential increase but in the grand scheme of things the system remains ferromagnetic, magnetized in the same direction and the magnetic moments are of the same order of magnitude. We would like to point out again that we are not really aiming at a perfect description of experiment (in which case a 19 % increase would not be negligible) but instead on how different theory levels affect qualitatively the dynamics.

Speaking of dynamics, they are also not affected very much by the change in the radius of the integration sphere, as seen in figure 3.8. In it, we see that the dynamics during a very short propagation (only 1 fs) do not change much with the radius used. Even if the discrepancy gets bigger further into the simulation the fact remains that the system still demagnetizes.

This means that the demagnetization we observe in this chapter is genuine and not only the result of electrons getting excited to states that lie beyond our unfortunately short integration radius. This is further corroborated by the results presented in the next chapter for antiferromagnetic materials that do not suffer from this problem. Furthermore, all of the results in this chapter suffer from this bugged radius so that the results are still consistent and comparable. And so in regards to this technical difficulty, we have found all is well that ends well.

Turning back to figure 3.7, when the Hubbard U correction is applied we find similar dynamics to the LSDA case, the difference being in the magnitude of demagnetization observed. The changes might not seem big but the demagnetization goes from around 8 % in Fe in the LSDA case to around 6 % with a U of 4 eV, a relative decrease of 25 %, though these are still quite far from the experimental results. LSDA+U then is not a magical cure that gets us results in perfect accordance with experiments, which to be fair was never really a reasonable expectation. But it does affect the results in a manner that can be considered significant and therefore a correct description of correlations is certainly a piece to be taken into account in getting us there.

We also note that for Fe and Ni the amount of demagnetization diminishes when the Hubbard U is applied while for Co it increases. So it seems that the Hubbard U impact, even qualitatively, greatly depends on the system being studied.

One important parameter to consider when doing time-dependent calculations that we have failed to mention so far in this chapter is the time-step. If a time-step that is too large is employed the propagation becomes unstable. That means, for example, that the total energy of the system will not be conserved and it will quickly diverge. At the same time, it is important to use a time-step that is as big as possible to guarantee that our calculations are done in a reasonable amount of time.

The variable reference for the Octopus code says that for 3D systems the biggest time-step possible has been found empirically to be (in atomic units)

$$dt = 0.046 - 0.207h + 0.808h^2, \tag{3.6}$$

where h is the spacing used for the real-space grid. We have found this default to generally be a good one but the value for the time-step will also depend on the system we are using, the perturbation we are applying, and other factors, so it is important that we confirm that our propagation is stable. In the end, the time-steps chosen in our calculations were 0.73 as for Fe, 1.21 as for Co, and 0.98 as for Ni.

To confirm that time-steps chosen are in fact appropriate we can look at the total energy dynamics, in figure 3.9 for the Fe case. After the laser pulse, the energy remains constant as expected since we do not consider coupling to the phonons and the external field is the only

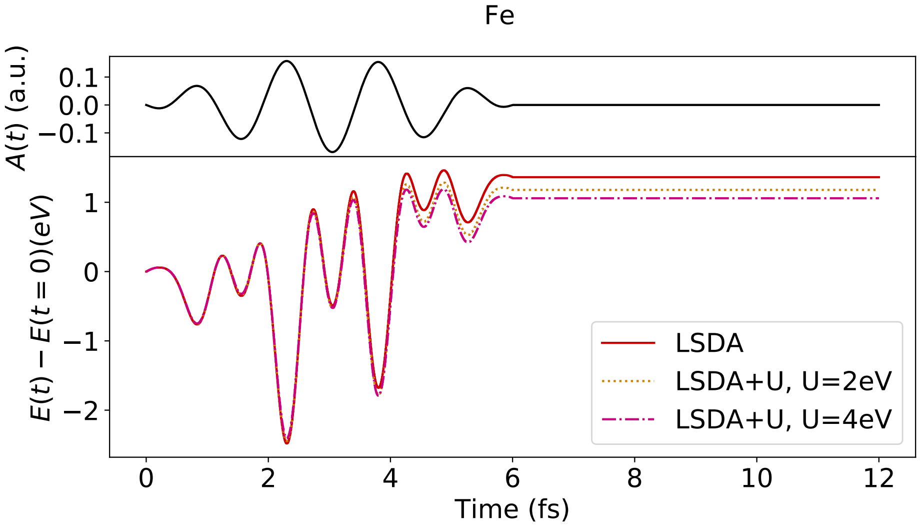

Figure 3.9: Energy dynamics for Fe in both the LSDA and LSDA+U cases.

source of energy for the system. This means that after the laser pulse there is no source of energy coming into the system and there is also nowhere else for energy to go and so the total energy must remain constant. The fact that the total energy remains constant after the pulse is therefore a good indication that the time-step was indeed chosen correctly and the calculations are converged with regards to this parameter. Similar results were obtained of both Co and Ni and are shown in appendix B.

Looking again at figure 3.9 we find that although the dynamics are rather similar for the different levels of theory considered (LSDA and LSDA+U) the final energies differ quite a bit, even though in all cases it is greater than the initial energy i.e. the system absorbed energy from the laser field. We can depict this more clearly by plotting the energy absorbed by the materials, that is, the difference between the energy at the beginning and the end of the simulation for each of the functionals used (Fig 3.10). As in figure 3.7, Co stands out as behaving contrary to both Fe and Ni. In both of those cases, the system absorbs less energy as the strength of the U applied increases but in Co it absorbs more. But since Co also demagnetizes more in the LSDA+U case what we find then is that the system absorbs more energy in the cases where it also demagnetizes more.

This apparent correlation between demagnetization and absorbed energy points to the laser field exciting a varying number of electrons, i.e. if the laser excites more electrons the system absorbs more energy and demagnetizes more, if the laser excites fewer electrons it absorbs and demagnetizes less. If this is the case we should be able to link it to the bandstructure of the material in question at equilibrium. To do so we look at the joint density of states (JDOS). The JDOS is in essence a density of transitions available to the

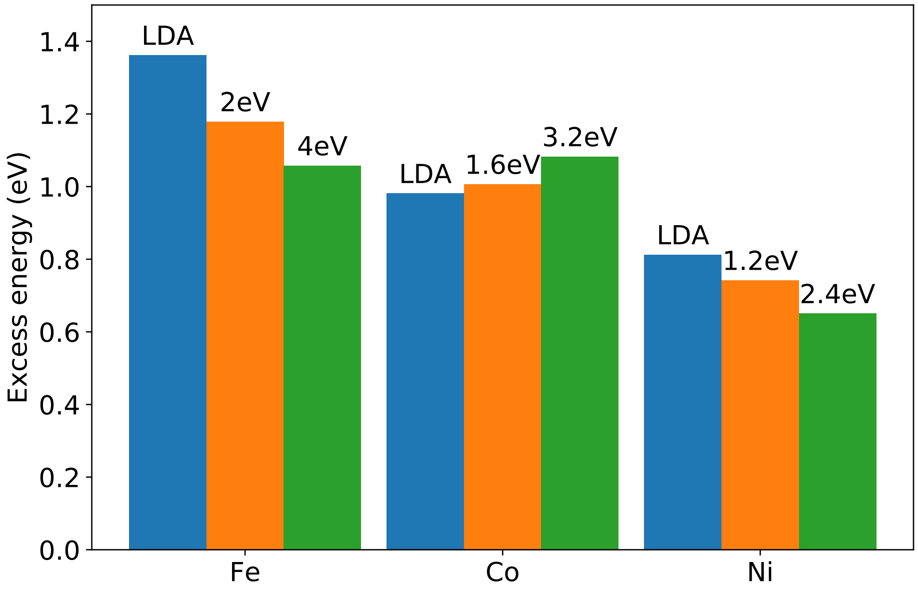

Figure 3.10: Excess energy for each material, using the same laser pulse as in Fig. 3.7, for both the LSDA and LSDA+U cases. This is computed as the energy difference between the beginning and the end of the simulation.

system. It measures how many pairs of occupied and unoccupied states in each spin channel exist that are separated by a given energy. The JDOS at the LSDA and LSDA+U level for each of the materials studied is plotted in Fig. 3.11.

The Hubbard U correction shifts the d orbitals of the metals and so in general there are fewer optical transitions at the laser frequencies and more at higher energies. This is particularly clear in the Fe case where the JDOS decreases with U in the laser region and increases for example in the region around 8 eV. As we expected there are fewer transitions available at the laser frequencies in Fe with increasing U and suitably less demagnetization. In Ni, the Hubbard U does not have a big impact on the JDOS in the region of interest and indeed its demagnetization is little affected by it. For Co, the contrarian case where demagnetization increases with U, things are a little more complicated. The region where the JDOS goes from being smaller in the LSDA+U case compared to the LSDA one to being bigger happens where the laser spectrum is strongest. This makes a simple visual interpretation rather more difficult but we can probe other areas of the JDOS where their relative strengths are clearly differentiated. For example, at lower energies, the Co JDOS is decidedly bigger in the LSDA case and it gets smaller with increasing U. We therefore expect a laser field centered at 1.2 eV (spectrum shown on the right side of Fig 3.12) to demagnetize more in the LSDA case and this is indeed what we observe on the left panel of Fig 3.12.

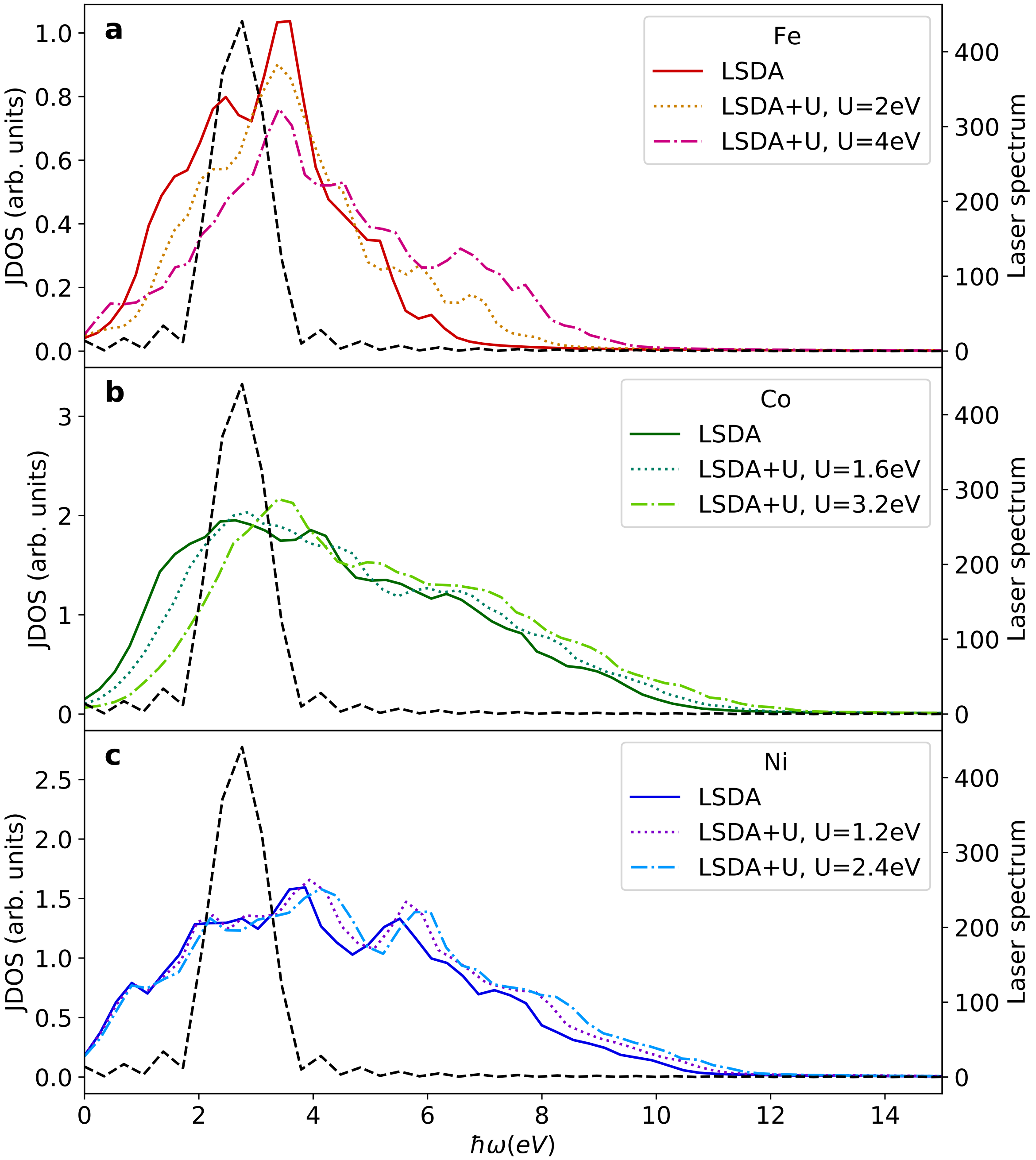

Figure 3.11: Joint density of states for the LSDA and LSDA+U cases in a) Fe, b) Co and c) Ni. Superimposed is the frequency spectrum of the laser pulse used (dotted line, in arbitrary units).

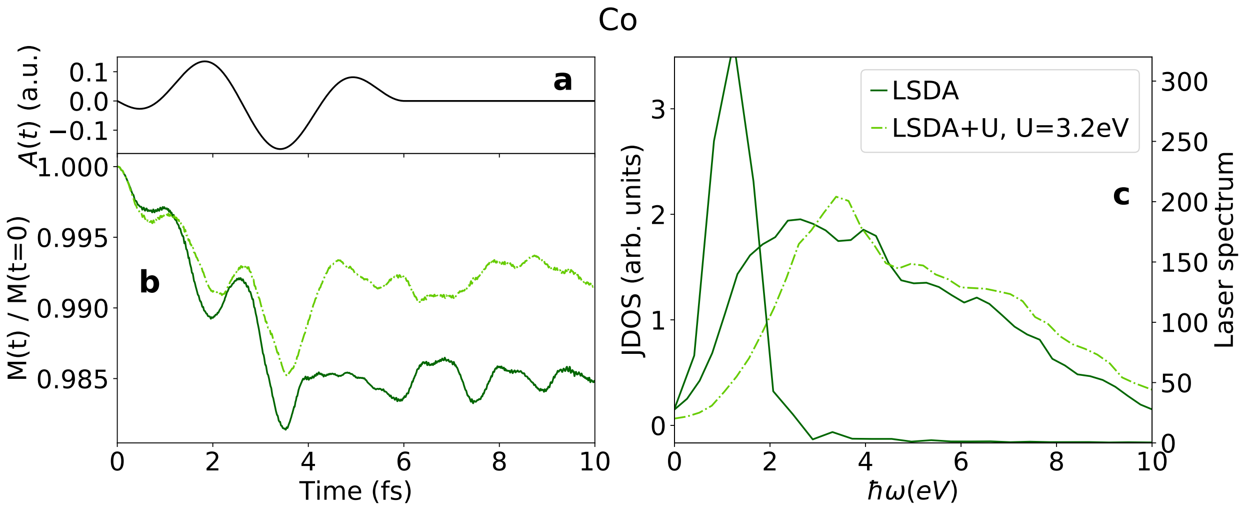

Figure 3.12:) Vector potential $\mathbf{A}(\mathrm{t})$ of the laser field with a central frequency of 1.2 eV . b) Demagnetization of Co with standard LSDA and LSDA+U with $U = 3.2$ eV c) Joint density of states for the LSDA and LSDA+U cases in Co. Superimposed is the frequency spectrum of the laser pulse used

We note that the demagnetization here is not only inverted in terms of relative strength from the Co case in Fig. 3.7 but its magnitude is also lower, as the JDOS is smaller in this region than in the region probed by the first laser. This again points to the magnitude of demagnetization being related to the amount of optical transitions available which is an important result that can be quite useful in the search for materials suitable for all-optical demagnetization.

3.3 The effects of different laser parameters

If this is the case and our results are simply due to electronic transitions then how are results at this level of theory affected by the choice of the perturbation to be applied? How do different parameters of the laser field, intensity, frequency, and duration, influence the demagnetization dynamics calculated? Is the fluence, the quantity most often used to describe the applied laser fields, even a good descriptor when dealing with such short pulses?

In this section, we present the results of calculations done with laser fields with changing parameters in order to address these questions.

3.3.1 Intensity

If demagnetization is initiated by the excitation of electrons to the conduction band then more photons should lead to more excitations and therefore more demagnetization i.e., as-

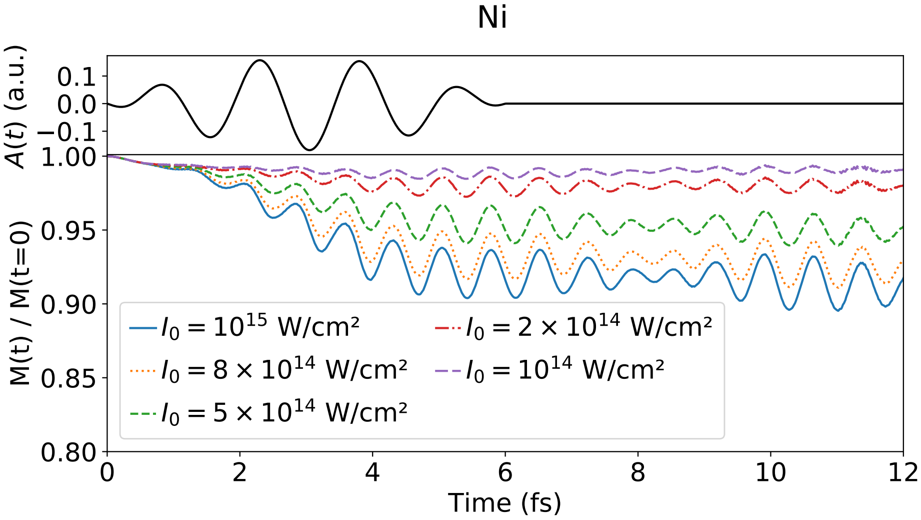

Figure 3.13: Upper panel: Laser pulse shape. Lower panel: Time evolution of the relative magnetic moment for Ni under the influence of laser field of varying peak intensity.

suming single-photon absorption, the demagnetization should scale linearly with the intensity of the laser field. In order to test this we applied laser fields of differing intensities to Ni while keeping the pulse duration and its frequency fixed (Fig 3.13).

It is clear that the different laser fields produce similar dynamics (demagnetization during the laser pulse and oscillations around a fixed value after it) and that lower intensities produce less demagnetization. But does it scale linearly as expected?

To better visualize whether that is the case we plot in figure 3.14 the final amount of demagnetization (averaged over the last 1000 time-steps, 0.98 fs) as a function of the intensity of the field used. We can see that it does indeed scale linearly.

The demagnetization scales roughly linearly with intensity but it starts to depart slightly from this behaviour as the intensity increases. The most intense pulse is 10 times as intense as the least intense one whereas the demagnetization goes from around 0.92 % in the $I_0 = 10^{14}$ W/cm^2 pulse to around 8.77 % in the $I_0 = 10^{15}$ W/cm^2 pulse or about 9.53 times as much. This departure may be due to non-linear effects created by the high intensities used. This once again suggests that at the LSDA level demagnetization and optical transition availability are tightly connected. We find similar results for Co, depicted in appendix C.

Given this, one may now ask whether the laser intensity or the laser fluence is better suited to describe demagnetization. To investigate this we employ different laser fields with the same central frequency but different pulse duration and peak intensity such that they all had the same fluence. For example, we employ a laser field that is 10 times less intense than the field we used originally, in figures 3.7 and 3.12, but also lasts 10 times longer.

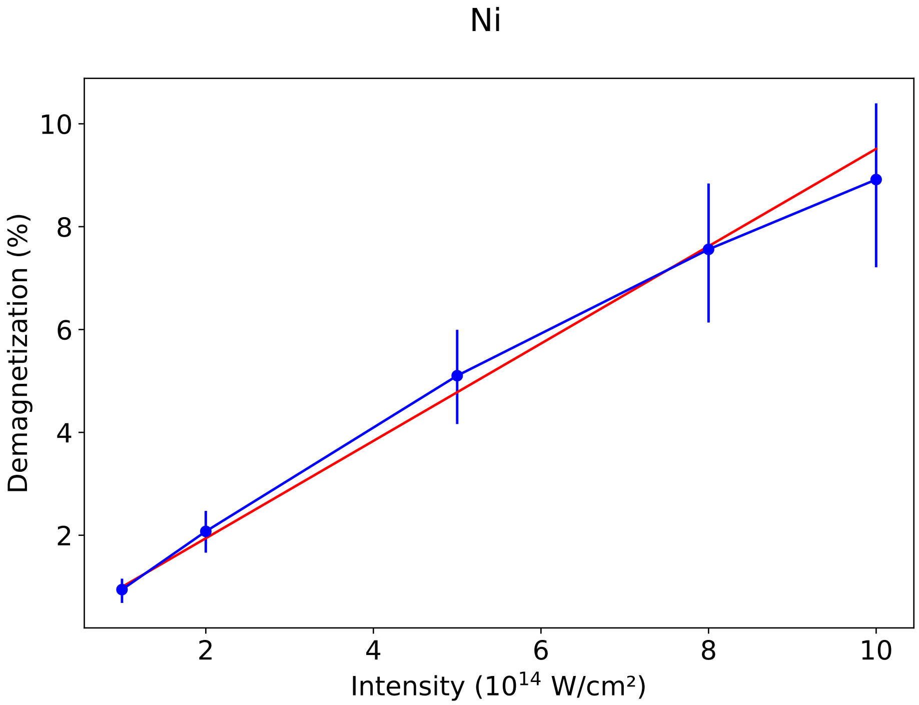

Figure 3.14: Demagnetization as a function of peak intensity for Ni. The red line is a guide to the eyes.

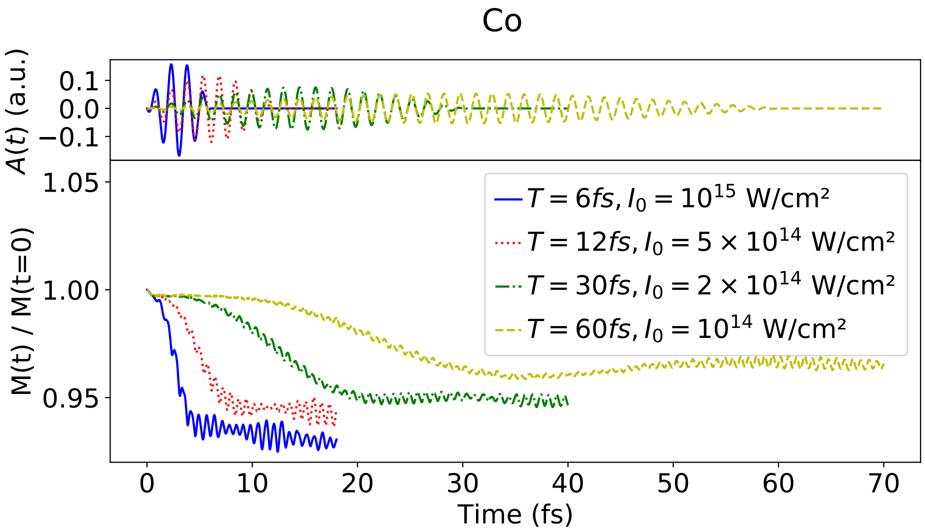

Figure 3.15: Demagnetization in Co under the influence of four distinct laser fields with the same fluence.

This time we choose Co as the system to apply the various same-fluence laser fields. As can be seen in figure 3.15, these pulses lead to quite different demagnetization levels leading us to conclude that the laser fluence is not a good predictor of how much a given laser pulse can demagnetize the material, at least for the kind of short, intense laser pulses used here.

Like in the earlier results demagnetization is not present after the laser pulse but these new longer calculations shine light on another important aspect of light-induced demagnetization which is not clear under the ultra-short laser pulses used originally: the demagnetization seems to occur mostly at the beginning of the laser pulse and to saturate as it nears its end. This is clearer in the case of the laser field with an intensity $I_0 = 10^{14}$ W/cm^2 and a total duration of $T = 60$ fs. In it, the magnetization essentially stops around the 35 fs mark, just over halfway through the laser pulse. This effect is related to the excitation to the conduction bands. In the view of single-photon absorption, the number of electrons excited by a laser pulse resembles the time integral of the pulse. That is, most of the ionization takes place around the field maximum rather than at the end of the pulse. The fact that the demagnetization process resembles the time integral of the laser pulse is yet another indication of its tight connection to the number of electrons excited in the conduction bands.

A further interesting aspect of figure 3.15 is that, at least as far as the parameters considered here, shorter laser pulses demagnetize more. And as in the first case (Figs 3.7 and 3.10), the system absorbs more energy when it demagnetizes more, as can be seen in Fig 3.16, despite all laser pulses carrying the same amount of energy.

A more intense laser field will evidently excite more electrons within each half cycle but the less intense pulses are longer so that the total amount of excitations should be the same. If we assume this process to be linear in intensity, for the same fluence we should get the same demagnetization yet this is clearly not the case in our simulations. The laser fields all carry the same total amount of energy but the system absorbs it quite differently from case to case. How then do we explain the difference in demagnetization between the various laser fields?

Looking at the frequency spectrum of the pulses and the JDOS of Co at the LSDA level, the system considered here, in Fig 3.17 we find that the laser pulses we employ have quite different frequency spectrums and, as expected, that the shorter pulses have wider spectrums. The shorter pulses are so short that they encompass a broad range of frequencies. The shortest laser (peak intensity of $I_0 = 10^{15}$ W/cm^2 and duration of $T = 6$ fs) has a FWHM of around 1.5 eV. This means this laser field has a larger set of frequencies and thus access to more optical transitions. On the other end, the longest pulse has a FWHM of about 0.25 eV and covers quite a smaller range of frequencies.

We attribute the higher demagnetization for the shorter pulses to the fact that they can

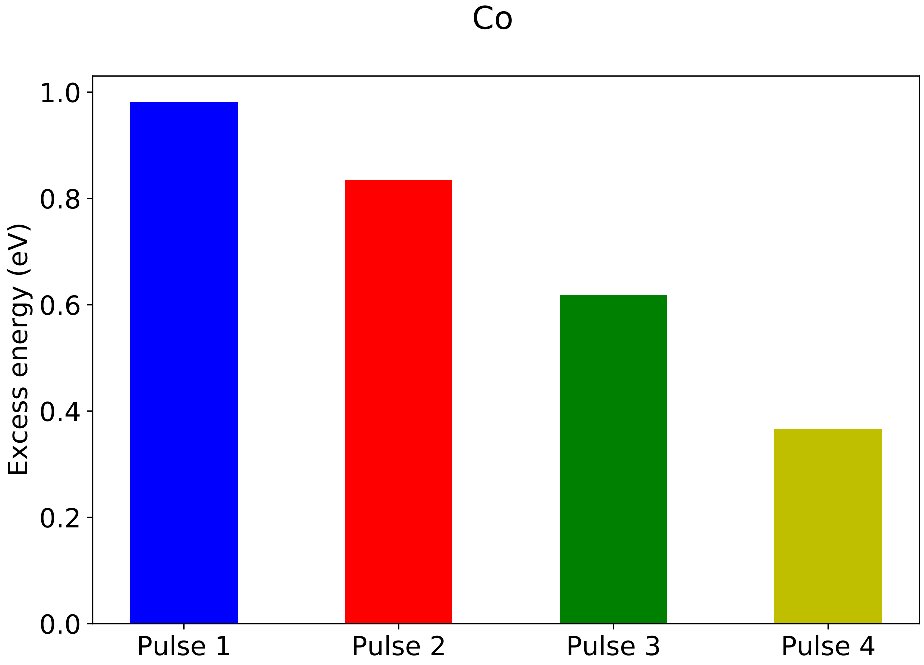

Figure 3.16: Excess energy for Co under the influence of different laser fields with the same fluence. The color coding for the different laser pulses is the same as in Fig 3.15.

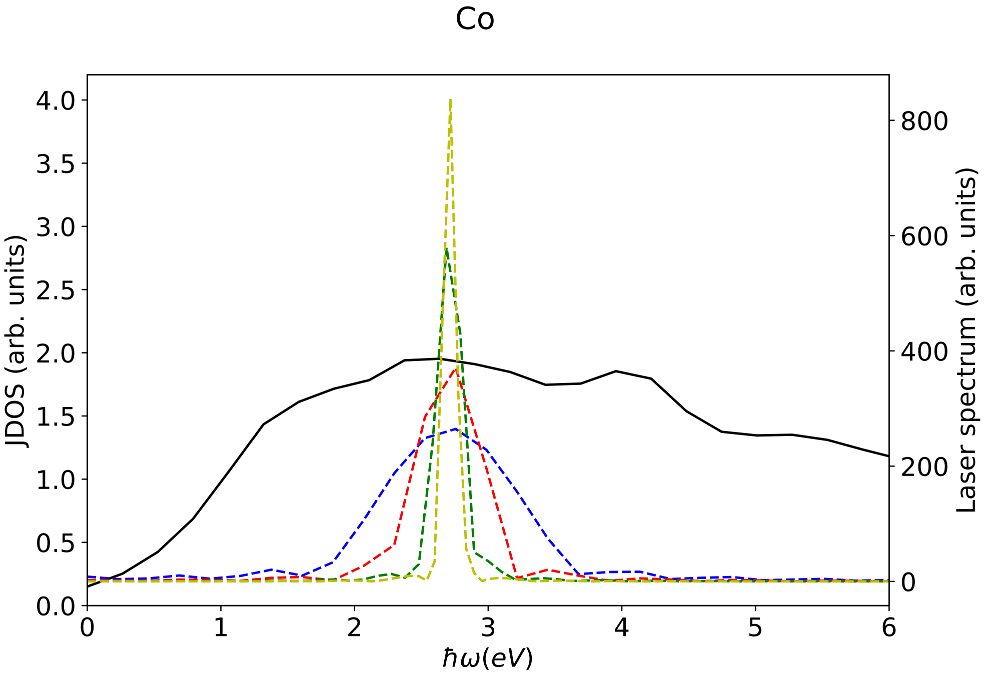

Figure 3.17: Detail of the joint density of states for Co with the frequency spectrum of the different laser pulses used superimposed. The laser spectrums are color coded the same way as in Fig. 3.15

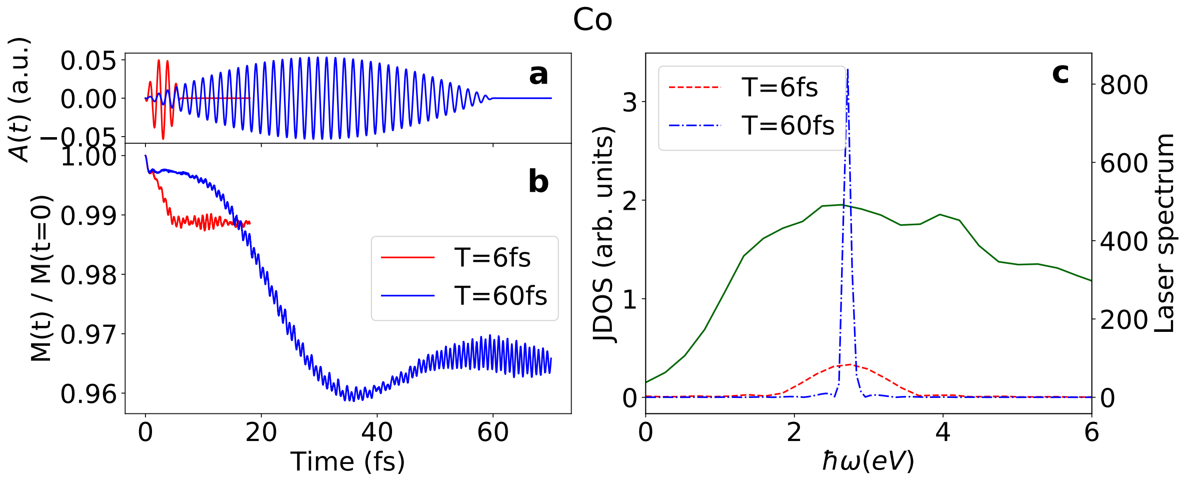

Figure 3.18: a) Vector potential $\mathbf{A}$(t) of the laser fields with different pulse duration but the same remaining parameters. b) Time evolution of the magnetic moment of Co under these two laser fields. c) JDOS of Co (solid line) and the frequency spectrum of the two laser pulses used.

excite many more electrons because they have access to many more transitions. This also means that when a pulse is so short that the number of optical transitions available varies significantly over the energy range covered by the laser spectrum, the fluence stops being a valid quantity to describe demagnetization, and one should consider instead pulse duration and intensity as two independent and equally relevant parameters having different effects on the light-induced demagnetization.

As the pulses get longer their spectrum gets narrower and so the difference in the range of available transitions decreases. As so we expect that for longer laser fields the fluence becomes a good quantity to assess the magnitude of demagnetization, since such pulses would have such a thin spectrum that the JDOS region they would probe would be essentially constant.

3.3.2 Pulse duration

Looking at figure C.2 and figure 3.15 we notice that we already have calculations for Co under the influence of laser fields with the same intensity ($I_0 = 10^{14}$ W/cm^2) but different pulse duration (6 fs in figure C.2 and 60 fs in figure 3.15). This allows us to investigate the influence of yet another laser parameter, the pulse duration, in the demagnetization dynamics of ferromagnets.

Figure 3.18 shows these results, on the left side the magnetization dynamics of Co under the influence of these different length pulses and on the right side their frequency spectrum over the Co JDOS.

The longer pulse naturally carries more energy, more photons and so, in accordance with our previous results, it should produce more demagnetization. And that is indeed what occurs although unlike in the case of different intensities (figure C.2) the increase is not even nearly linear with the increase in energy. The 6 fs pulse demagnetizes around 1.1 % while the 60 fs demagnetizes around 3.4 %. A 10-time increase in the intensity, from 10^{14} to 10^{15} W/cm^2, increases the demagnetization more than 9 times over, while an equal increase in the duration of the excitation, from 6 fs to 60 fs, produces an increase in the demagnetization of only about 3 times. And this, despite the energy carried by the pulse increasing in the same manner. Once again we find that for ultra-short pulses different laser parameters have different effects on the demagnetization dynamics and each of them must be considered in conjunction with the others.

We attribute the different scaling of the demagnetization amount when changing the duration compared to changing the intensity to the different laser spectrums of the two pulses used in the pulse duration case as seen on the right side of figure 3.18. Unlike in the different intensity case, here the two laser fields probe different areas of the JDOS. The spectrum for the 60 fs is much sharper than the 6 fs one, and so the availability of transitions is quite different from one laser to the other. When we increase the energy carried by the laser pulse by increasing its duration we decrease the number of transitions that are available to the system but when we increase its energy by increasing the intensity we do not and so the demagnetization will not scale the same way in both cases.

These results once again support our claim that when dealing with ultrashort laser pulses the fluence ceases to be an acceptable descriptor of the laser field and each parameter must be considered when defining the laser field and its effects on demagnetization.

3.3.3 Frequency

From the parameters we used to define our original laser pulse the only one we have yet to look into in more detail is the frequency. But that is not quite true. We made sense of our results for Co with the LSDA and LSDA+U (figure 3.7) by probing a new region of the JDOS where the relative strength of the JDOS at the LSDA and LSDA+U level was clear (figure 3.12). The laser pulses used in both of these cases differ only by their central frequency and so we already have the data to find the role that the laser's frequency has on the demagnetization dynamics. In fact, we have it at both the LSDA and LSDA+U level.

We choose the LSDA+U case with a U of 3.2 eV and add a third laser field with central frequency of 8 eV as a further comparison point. Figure 3.19 shows both the demagnetization achieved with each pulse as well as their frequency spectrum in relation to the Co LSDA+U

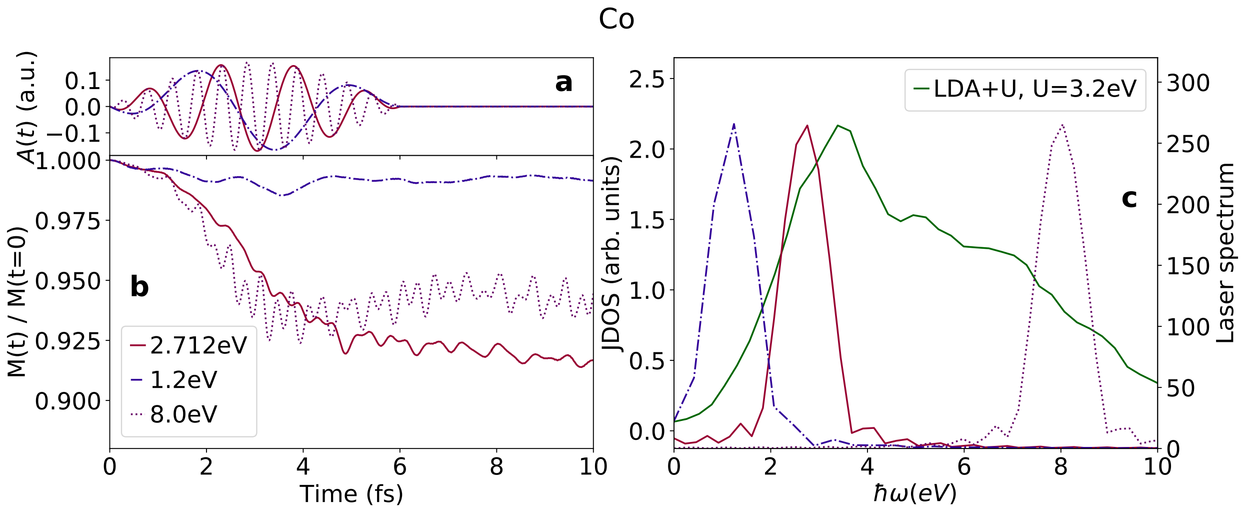

Figure 3.19: Demagnetization of Co with laser fields of central frequency 1.2 eV, 2.712 eV and 8 eV at the LSDA+U level with an effective U of 3.2 eV. **a**) Vector potential $\mathbf{A}$(t) of the laser pulses, **b**) Magnetization dynamics of Co with standard LSDA+U under the different laser pulses. **c**) JDOS for the LSDA+U Co. Superimposed are the frequency spectrums of the laser pulses used (coded as in **a**)

JDOS on its left and right side, respectively.

Once more we find evidence of the relationship between demagnetization and optical transitions at this level. The amount of demagnetization observed tracks pretty well with the strength of the JDOS in the area covered by the spectrum of the laser field in question. The field with central frequency 1.2 eV is centered in the region with by far the lowest JDOS of the three and the demagnetization is correspondingly far lower than with the other two laser fields. Furthermore, the original field of 2.712 eV covers the area with the highest JDOS and demagnetizes the most. This is despite the fact that the highest frequency laser caries more energy than the middle one, meaning that the demagnetization observed at the ALSDA level is not just a function of the energy given to the system but does indeed depend critically on the availability of optical transitions.

All of the results in this section lay further strength to our claim that at the adiabatic LSDA level, with frozen ions, all the demagnetization observed is the result of atomic transitions. Whatever knob we turn in the external field we apply, be it its intensity, frequency, or duration, we can predict its effects, at least qualitatively, simply by considering its impact on the field's spectrum and how that relates to the JDOS of the material in question.

Chapter 4

Antiferromagnets

In this chapter we turn our attention to another class of systems, antiferromagnets. In antiferromagnetic materials, the magnetic moments are arranged ferromagnetically in different sublattices so that the total magnetic moment is zero. That is, magnetic moments in different sublattices point in opposing directions while all having the same direction in the same sublattice.

Antiferromagnetic systems are of particular interest to the field of spintronics because they promise an extremely fast switching rate. The spin dynamics in antiferromagnets are orders of magnitude faster than in ferromagnets[58] and so can be used to achieve even faster reading and writing speeds. This speedup is a well-known property of antiferromagnets, known as the exchange enhancement of dynamic parameters[59], resulting from the fact that dynamic parameters contain a large parameter, H_{ex}, the exchange field of the antiferromagnet, not present in ferromagnets.

In particular, we will be looking at antiferromagnetic transition metal oxides where electronic correlations play an important part. In fact, correlations play such an important part in describing, for example, NiO that, when ignored, the ground-state is predicted to be metallic when in reality it is an insulator. This class of materials is known as Mott insulators. Since we are dealing with the same class of metallic elements as in the previous chapter we run into the same problem that the localized $3d$ orbitals are not properly described at the LSDA level. MnO, FeO, CoO, and NiO are examples of Mott insulators where the LDA is well known for its inability to correctly reproduce the insulating case[30]. Changing to a spin-dependent version (LSDA) does produce a band gap at the Fermi level for MnO[60, 61]. And yet it still fails to do so for many other systems, FeO and CoO among them, meaning that a better approach is necessary, like the LSDA+U one. If correlations play such an important part in describing the ground-state properties of antiferromagnetic transition metal oxides what is their effect on dynamical processes such as laser-induced demagnetization?

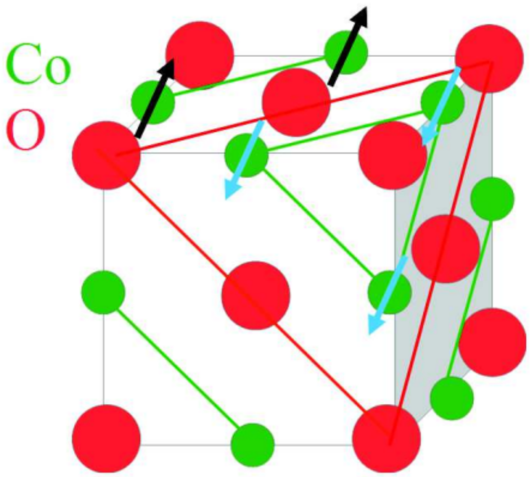

Figure 4.1: Typical structure for the transition metal oxides studied, although this picture is of CoO specifically. The alternating antiferromagnetically coupled planes are clearly visible. Taken from [62]

This is what we investigate in this chapter. We follow the blueprint laid out in the previous chapter and start by converging the ground-state in all the systems we intend to study before moving on to the LSDA and LSDA+U calculations. Here we study changes in both the ground-state and in the demagnetization dynamics. We interpret the findings in much the same manner as the ferromagnets and proceed to similar investigations of the effects of different laser parameters on the demagnetization observed.

4.1 Ground-state convergence

The antiferromagnetic materials we chose to investigate in this chapter were the transition metal oxides MnO, FeO, and NiO. These are the same transition metals used to study the ferromagnetic case with the exception of Mn substituting for Co. This was done because CoO proved to be extremely difficult to converge. The spacing needed to have the magnetization converged would be too small and the **k**-point grid too big, making the time-dependent simulations impractical.

The systems considered here all have the fcc rock-salt structure where the metal atoms form planes along the (111) direction and successive planes are coupled antiferromagnetically, as is shown in figure 4.1. Thus the simulation box used contains two metal atoms and two oxygen atoms, in order to properly simulate the antiferromagnetic state. Their lattice parameters are 3.18, 3.20, and 4.17 Å, for MnO, FeO and NiO respectively.

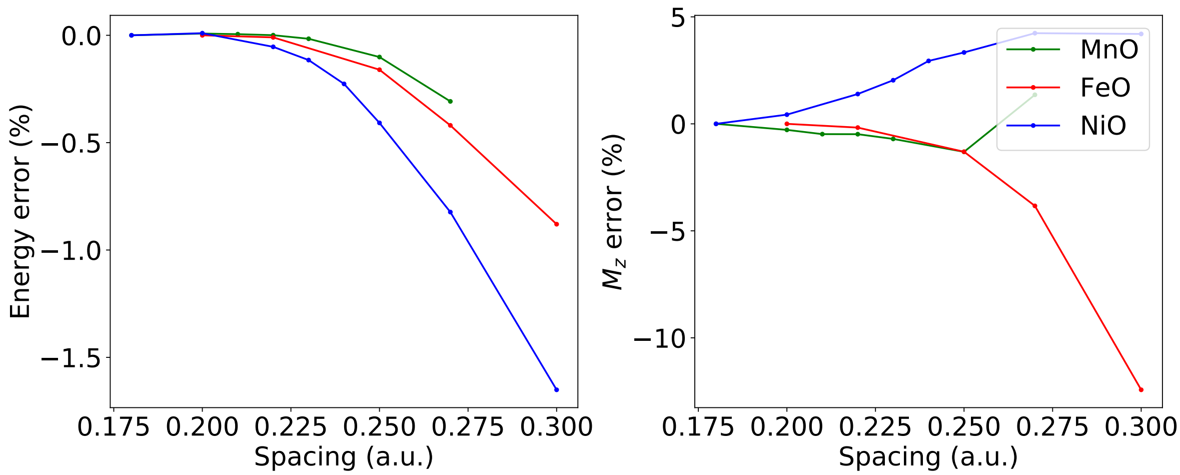

Figure 4.2: Convergence of the total energy (left panel) and the z component of the magnetization (right panel) with regards to the spacing used. The z component of the magnetization is calculated for one of the metallic atoms in the unit cell. These calculations were all done with a constant **k**-point grid. For MnO that grid was a $2 \times 2 \times 2$ **k**-point , for FeO a $4 \times 4 \times 4$ **k**-point grid and for NiO a $8 \times 8 \times 8$ **k**-point grid.

4.1.1 Total energy and magnetization convergence

Like in the ferromagnetic case we must start by ensuring that the ground-state is properly converged.

We begin by looking at the convergence of the total energy and the z component of the magnetization with regards to the spacing used, which is shown in figure 4.2. The error values displayed here, and later on in figure 4.3, are defined in the same manner as in the previous chapter, that is, in relation to the most precise calculations in each case (smaller spacing and denser **k**-point grid). The z component of the magnetization though is slightly different here compared to the one in the previous chapter. The quantity plotted here is calculated again in a sphere but this time there is no bug and the sphere's radius is indeed half the distance between two neighbouring atoms (1.123 Å for MnO, 1.042 Å for FeO, and 1.042 Å for NiO). The main difference though is that we plot the magnetization calculated around only one of the two metallic atoms present. The magnetization around the other metal atom is obviously symmetric, given that we are dealing with antiferromagnets, making the total magnetization essentially zero and therefore not a good measure of the convergence of the ground-state.

From this figure we can see that, like in the ferromagnets, the total energy is much easier to converge than the magnetization. Only one calculation here, NiO with the biggest spacing considered, even has a relative error greater than 1% for the energy. By comparison, the relative error in M_z for the same calculation is over 10%.

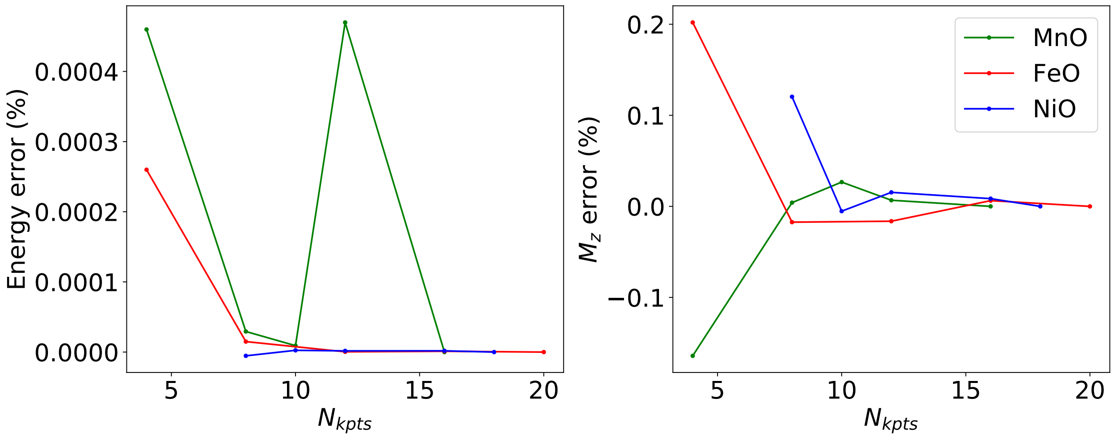

Figure 4.3: Convergence of the total energy (left panel) and the z component of the magnetization (right panel) with regards to the **k**-point grid used. The spacing was kept constant with at 0.122 Åfor MnO, 0.114 Åfor FeO, and 0.122 Å a.u. for NiO

The convergence of these same quantities with the size of the **k**-point grid is shown in figure 4.3. We again find that, as in the case of the ferromagnetic materials, the system is quite more sensitive to the spacing used than it is to the **k**-point grid. The total energy remains essentially constant and even the magnetization does not change much with the increase in **k**-point grid density.

The energy and the z component of the magnetization seem well converged with the sparsest **k**-point grid considered but again these are not the only quantities we consider when we study the convergence of our ground-state.

4.1.2 Density of states convergence

Following the ferromagnetic case, we also look at the DOS and it proved once again to be more difficult to converge than the total energy and the magnetization.

The DOS for FeO is shown in figure 4.4, with different spacing values on the left panel and with different **k**-point grids on the right panel, analogously to figure 3.3 in the ferromagnetic case.

Here we can see why the ground-state can not be considered converged, despite the energy and the magnetization appearing converged with even the sparsest **k**-point grid size used in figure 4.3. The DOS clearly exhibits some deviations in the calculation with a $4 \times 4 \times 4$ **k**-point grid that are not present with a denser grid. This is why we can not rely on a single quantity to judge whether or not the ground state is converged. Different properties converge at different rates and it is important that all quantities of interest are well converged.

Similar plots for the DOS of MnO and NiO are presented in appendix D, where we find

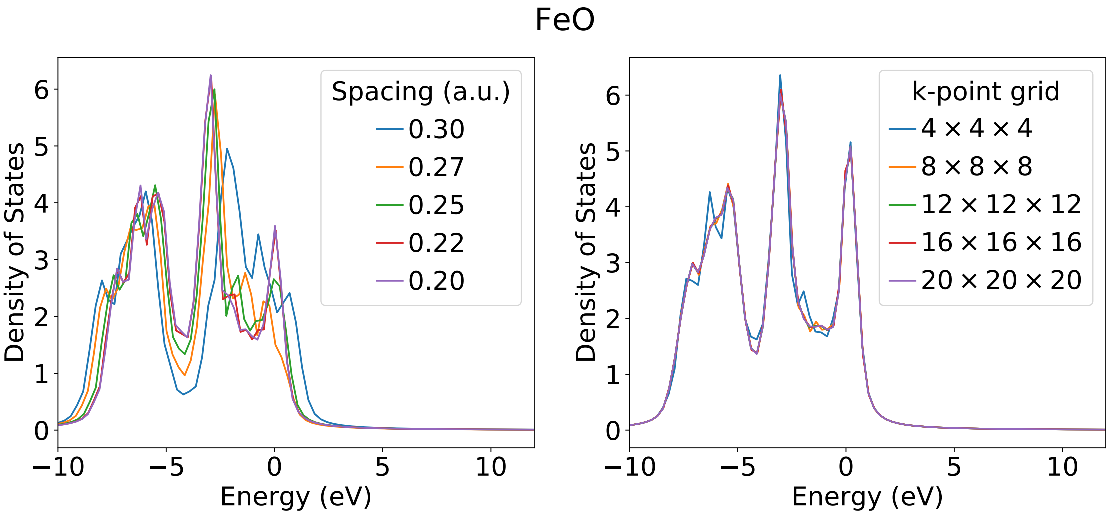

Figure 4.4: Convergence of the density of states of FeO with regards to the spacing (left panel) and to the **k**-point grid used (right panel). In both panels 0 corresponds to the Fermi energy

that for MnO, like for FeO, the DOS is also not properly converged with a $4 \times 4 \times 4$ **k**-point grid. In the NiO, case the smallest **k**-point grid considered was an $8 \times 8 \times 8$ one and the DOS seems properly converged with it.

The data shown in figure 4.4 also reinforces the notion that these systems are more sensitive to changes in the spacing than in the **k**-point grid.

4.1.3 Demagnetization convergence

Finally, we look at the property whose convergence is most crucial for our work, the demagnetization dynamics themselves.

To confirm that the dynamics are properly converged we again perform small time-dependent runs of just 3 fs with different spacing values and different **k**-point grids. This is shown for FeO in the LDA+U case with $U = 5eV$ in figure 4.5.

Like in the ferromagnetic case, and also similarly to the other quantities we have looked at so far, the demagnetization is much more susceptible to changes in the spacing than in the **k**-point grid. Changing from an $8 \times 8 \times 8$ to a $10 \times 10 \times 10$ **k**-point grid, while keeping the same spacing, has no discernible effect on the demagnetization dynamics (the two lines, solid blue and dotted cyan, overlap in figure 4.5). The spacing however does have a significant effect. Going from a spacing of 0.22 a.u. (0.116 Å) to a spacing of 0.20 a.u. (0.107 Å) while keeping the **k**-point grid fixed, drastically changes the dynamics just in this short interval. So while the DOS, the total energy, and the magnetization of FeO look converged with a

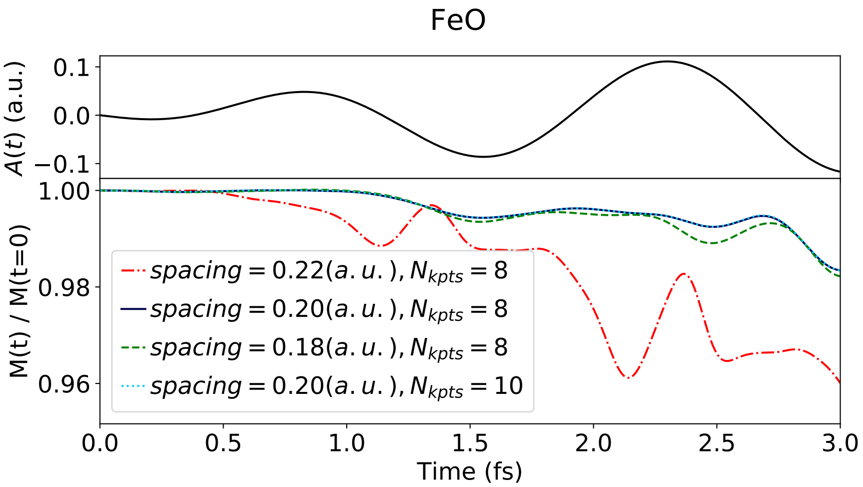

Figure 4.5: Short propagation of the relative magnetization in FeO in the LDA+U case with $U = 5eV$ with different parameters. The upper panel shows the vector potential $\mathbf{A}(\mathrm{t})$ of the laser pulse and the lower panel the various dynamics.

Table 4.1: x, y and z components of the total ground-state magnetic moment for each of the oxides considered (in Bohr magnetons).

	m_x	m_y	m_z
MnO	-0.000001	0.001397	-0.003013
FeO	-0.000381	-0.004370	-0.000061
NiO	0.000000	0.000000	0.000000

spacing of 0.22 a.u. (0.116 Å) it is clear the dynamics are not and so we cannot consider our ground-state converged with this spacing.

Similar studies for the convergence of the demagnetization dynamics for MnO and NiO were also performed and are shown with the rest of the plots regarding the convergence of the ground-state for these systems in appendix D, with comparable results.

Taking all of this information for all of the quantities considered and for the various cases studied, the ground state was ultimately considered converged with a uniform spacing of 0.122 Å (0.23 a.u.) and an 8 × 8 × 8 **k**-point grid to sample the Brillouin zone for MnO, a spacing of 0.107 Å (0.20 a.u.) and an 8 × 8 × 8 **k**-point grid for FeO, and a uniform spacing of 0.095 Å (0.18 a.u.) and a 10 × 10 × 10 **k**-point grid for NiO.

We should note that the ground-state we find is indeed antiferromagnetic as we can see by the total magnetic moment, calculated by integrating the magnetization in the entire simulation box, displayed in table 4.1.

Since there are only two magnetic atoms in the simulation box (the magnetic moment around the two oxygen atoms is essentially zero) the fact that each component of the total magnetic moment is quite small, or in the NiO actually zero, means that magnetic moments of the metal atoms are antisymmetric and we have indeed an antiferromagnetic system.

When comparing to the ferromagnets, the antiferromagnets only converge with quite a smaller spacing but also a smaller number of **k**-points, which is not surprising since the simulation box is bigger here, containing two metal atoms and two oxygen atoms.

4.2 LSDA+U calculations

With the ground state converged we can finally look at the demagnetization induced in the antiferromagnets in question by a laser pulse with the same parameters as the one used in figure 3.7.

The values for the Hubbard correction used in the LSDA+U calculations were 2 and 5 eV for MnO, 3 and 5 eV for FeO, and 2 and 6.93 eV for NiO. These values were again chosen from the range of values used in the literature.[63, 64] The U correction was only applied to the $3d$ orbitals of the metallic atoms, the O atoms were treated with standard LSDA.

The time steps used this time around were 0.73 as for NiO, also 0.73 as for MnO, and 0.48 as for FeO.

4.2.1 Effects of U on ground-state properties

Following the pattern we established in chapter 3 we start by looking at the changes brought about in the ground-state by the change in the theory level used.

In figure 4.6 we plot the DOS for FeO at the LSDA level and with both of the values used for U at the LSDA+U level, 3 and 5 eV. Looking at the DOS close to the Fermi level (represented as the zero on the energy scale) we see that the LSDA does indeed fail to predict an insulating ground-state, since the DOS not only is non-zero here, it even has a strong peak. In the calculations done with the Hubbard U on the other hand, the DOS at the Fermi level is very close to zero. With a properly selected value for the Hubbard U, one would obtain the real, insulating ground-state.

A similar shift, from the metallic to an insulator state with the application of the Hubbard U can also be seen for MnO and NiO and is depicted in appendix E.

Following again the ferromagnetic example, we can study how the Hubbard U affects the magnetic moments. These results are shown in table 4.2. Unlike in the ferromagnetic case, the magnetic moments are not calculated in the entire simulation box, those are very close to zero as we show in table 4.1, but around only one of the metallic atoms, as we have discussed above in subsection 4.1.1.

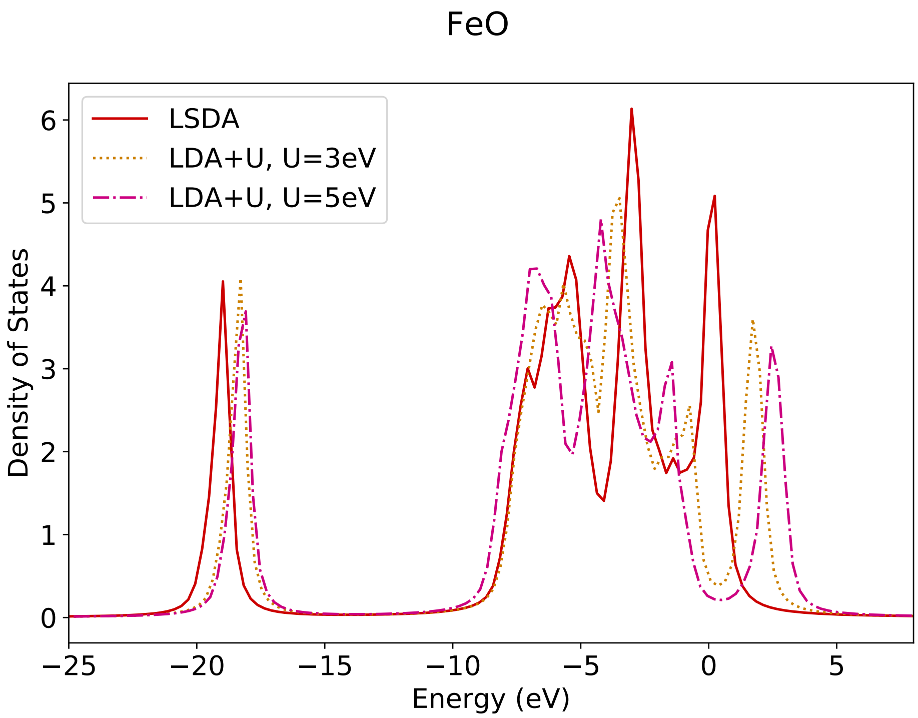

Figure 4.6: DOS for FeO in the LSDA and LSDA+U cases. In all cases the 0 of the energy corresponds to the Fermi level. Note how the system goes from metallic at the LSDA level to insulating at the LSDA+U level.

Our results are similar to other LSDA results[67], and like in our ferromagnetic calculations, the magnetic moment increases as the U increases. In fact, for both MnO and NiO, the calculated value gets closer to the experimental value as stronger U corrections get applied. This is not the case for FeO where the LSDA magnetic moment is already bigger than the experimental value, though not by much, and so as it increases with the U correction it keeps getting further from it.

This increase in the magnetic moments when the U correction is applied is easily understood in the same way as in the ferromagnetic case, discussed in chapter 3. The U values could have been chosen to better reproduce the experimental moments but we again

Table 4.2: Ground state magnetic moments per atom calculated versus experimental values (in Bohr magnetons per atom). The values of U used are described in the main text and $U_2 > U_1$

	LSDA	U_1	U_2	exp.
Mn in MnO	4.214	4.392	4.477	4.58[65]
Fe in FeO	3.438	3.503	3.554	3.32[66]
Ni in NiO	1.263	1.480	1.634	1.90[65]

note that the objective here was not to reproduce experiments but to investigate the effect of the Hubbard U in the demagnetization dynamics and how changes in the ground state description affect them in the adiabatic regime.

And so, in regards to changes to static properties, we have confirmed that even adequate values of U account much better for correlation effects in transition metal oxides and improve significantly their ground-state description. They may or may not also improve the values for the magnetic moments. But how do they affect the demagnetization dynamics?

4.2.2 Demagnetization dynamics

Before we look at the results of the time-dependent simulations we must consider the fact that we are now dealing with antiferromagnets which presents us with a new challenge, how do we plot the magnetization dynamics? The total magnetization is nearly zero, as evidenced in table 4.1, and so it is of no use.

It is usual, when dealing with antiferromagnets, to use the staggered magnetization

$$\mathbf{S} = \mathbf{M_1} - \mathbf{M_2}, \tag{4.1}$$

where M_1 and M_2 refer to the magnetization in each of the sublattices. This way we get a quantity that is non-zero and so much more useful.

However, since the dynamics in both of the magnetic atoms are generally symmetric (which we can clearly see in figure 4.7 for NiO) then it suffices to look at the magnetization surrounding one of the magnetic atoms. There is no need to go the extra step of creating a new quantity to account for the two sublattices when the dynamics in one just mirror the other.

In the end, the magnetization whose dynamics are plotted in figure 4.8 and throughout this chapter is calculated around one of the metal atoms (with the radii that are mentioned in the previous section) and the magnetization around the other metal atom is symmetric.

Now that we have guaranteed that our calculations are converged with regards to the different parameters in Octopus, that we have seen how U affects the ground-state, that we have clarified the technical details of what we will be looking at, we can finally move on to the stated purpose of this chapter, to investigate the impact of the Hubbard U correction on the light-induced demagnetization in the antiferromagnetic case. These results are shown in figure 4.8.

The first thing that jumps out from figure 4.8 when compared to the analogous results for ferromagnets in chapter 3 is the magnitude of demagnetization achieved here. Whereas in the ferromagnetic case we find demagnetizations of around 8%, in here we have, at the

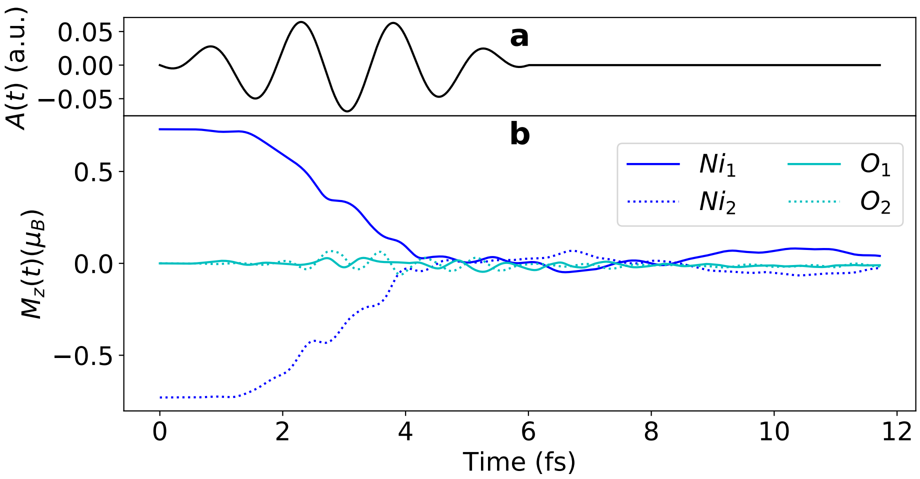

Figure 4.7: Demagnetization dynamics of the z component of the magnetic moment around each atom in the NiO case at the LSDA level. The symmetry between both magnetic atoms is clear.

LSDA level, demagnetization of around 15% for both MnO and FeO. NiO even demagnetizes almost entirely with the LSDA.

Another noteworthy difference is in the impact that the Hubbard U has. The effects on the demagnetization are much more pronounced here. For the transition metal oxides here we find relative decreases in the amount of demagnetization of around 64%, 63%, and 47% when going from LSDA to the smaller value of U for MnO, FeO, and NiO respectively. For comparison, in Fe, which is the system most affected by the U from among the ferromagnets we studied, a correction of 4 eV changes the demagnetization from around 8% at the LSDA level to around 6%. This is still a significant change but nowhere near the aforementioned change of 63% for FeO with a smaller U of 3 eV.

When compared with the ferromagnets, the demagnetization in the antiferromagnets also happens faster, saturating a bit before the end of the pulse. Take the example of Ni as a ferromagnet and in NiO. The dynamics for both of these cases at the LSDA level is depicted in figure 4.9. Take care that in this figure each one is plotted on a different axis as the amount of demagnetization observed is wildly different in the two cases and we are only interested in the overall shape. The dynamics in the antiferromagnetic case saturate a bit faster, around the 4 fs mark which is, as we discussed above, a known property of antiferromagnets and one of the reasons for the interest in their demagnetization.

Turning from differences to similarities, the magnetization also remains essentially constant here after the laser pulse which is, as we discussed in the previous chapter, both contrary to experimental results but also to be expected at this theory level.

Returning to our antiferromagnets in and of themselves, we can take a look at the dy-

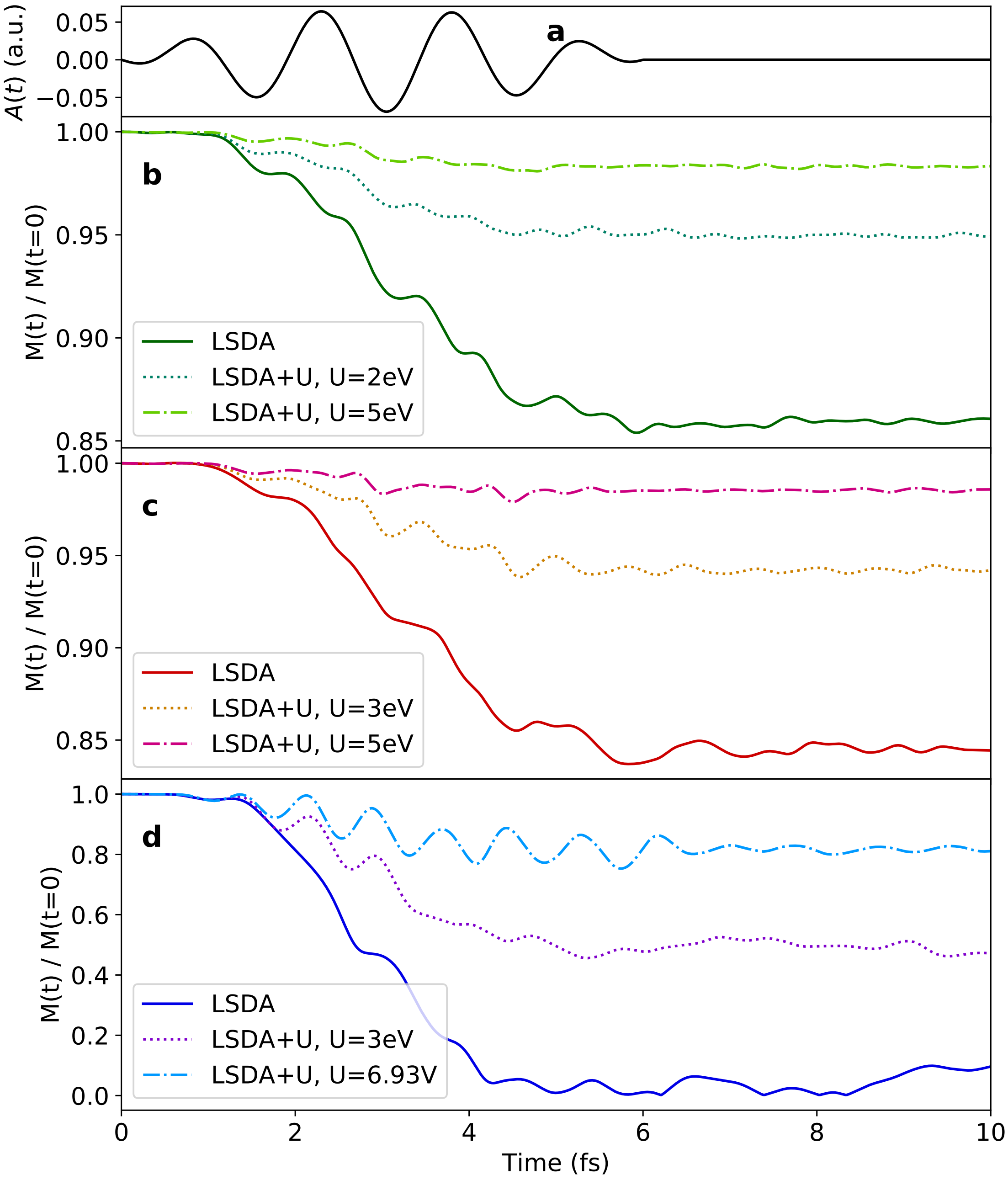

Figure 4.8: Demagnetization of transition metals oxides. From top panel to bottom panel, we have a) the vector potential $\mathbf{A}(\mathrm{t})$ of the laser pulse, the magnetization dynamics of b) MnO, c) FeO, and d) NiO with standard LSDA and using LSDA+U. The values of $U_{\text{eff}} = U - J$ and the parameters of the laser pulse are given in the main text. The magnetization plotted here is not the total one but the magnetization calculated in a sphere around one of the magnetic atoms.

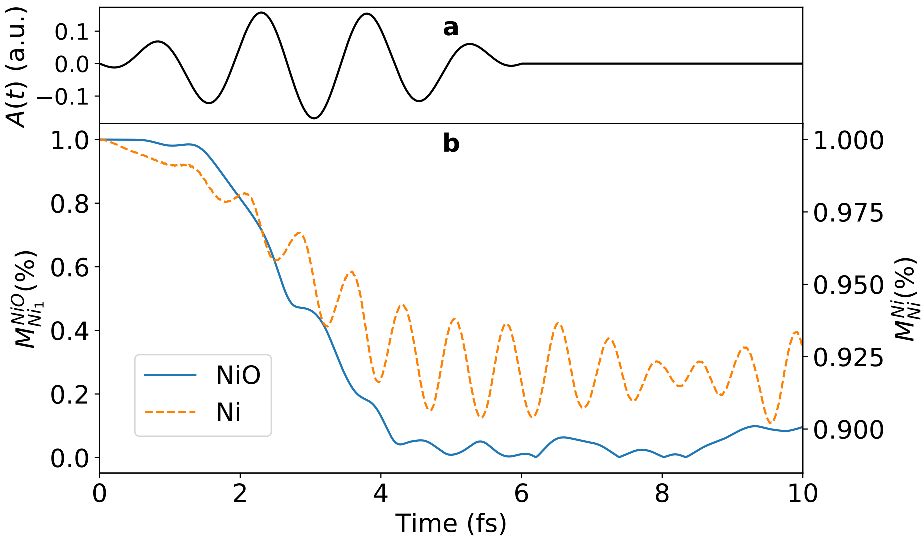

Figure 4.9: Demagnetization dynamics for bulk Ni and Ni in NiO at the LSDA level.

namics of the total energy for NiO in figure 4.10. It is important to note that, as with the ferromagnets in the previous chapter, after the laser field is gone, the total energy remains constant in all cases (including for MnO and FeO as can be seen in similar plots in appendix E). This is again an indication that the calculations are well converged with regards to the time-step used. It is also apparent that the energy after the laser pulse is greater than at the beginning, i.e. the system again absorbs energy.

But if we want to look only at the energy transferred to the system in the course of the demagnetization process figure 4.10 is not the most useful, given the huge swings in energy provoked by the extremely intense laser field we employ, and so we resort again to plotting only the energy absorbed by all the systems in figure 4.11.

Looking at it we find once more that when the system demagnetizes more it also absorbs more energy. Note also that NiO is by far the system that absorbs more energy and it is also by far the oxide that demagnetizes the most in our calculations. The difference in excess energy between the LSDA case and the different LSDA+U cases is more pronounced here than in the ferromagnets studied above, and so is the difference in demagnetization.

As in the ferromagnetic case, the increased absorption points to more transitions taking place, and so, analogously to figure 3.11, we again look at the JDOS, which we plot for the oxides in figure 4.12, with the laser spectrum superimposed. We find again that the Hubbard U correction shifts the energy of the orbitals it is applied to, increasing the energy necessary for excitations involving those states, which is reflected in the JDOS as a shift towards higher energies. This shift is also reflected in the magnetic moment calculated around each magnetic atom, as is shown in table 4.2.

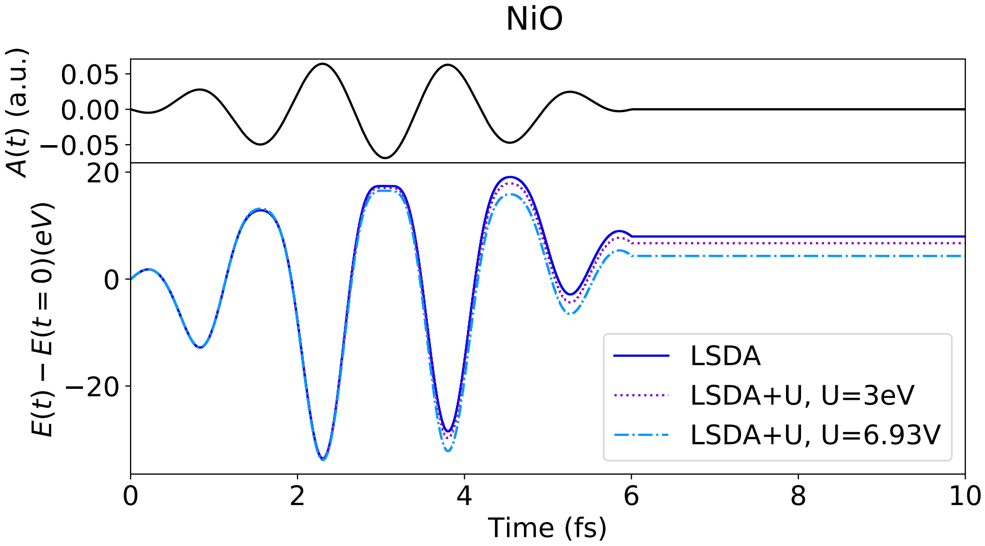

Figure 4.10: Energy dynamics for NiO in both the LSDA and LSDA+U cases.

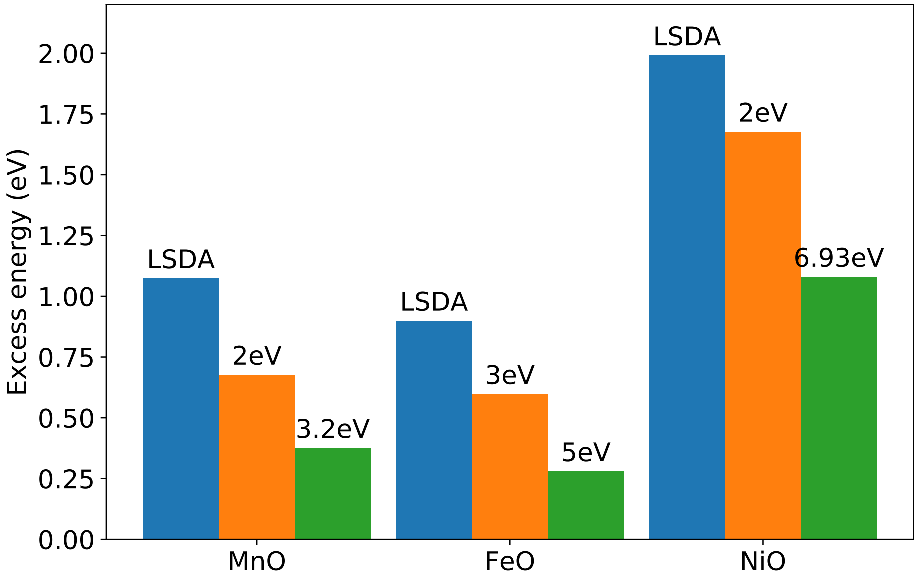

Figure 4.11: Excess energy per atom for each material, using the same laser pulse as in figure 4.8, for both the LSDA and LSDA+U cases. This is again computed as the energy difference between the beginning and the end of the simulation.

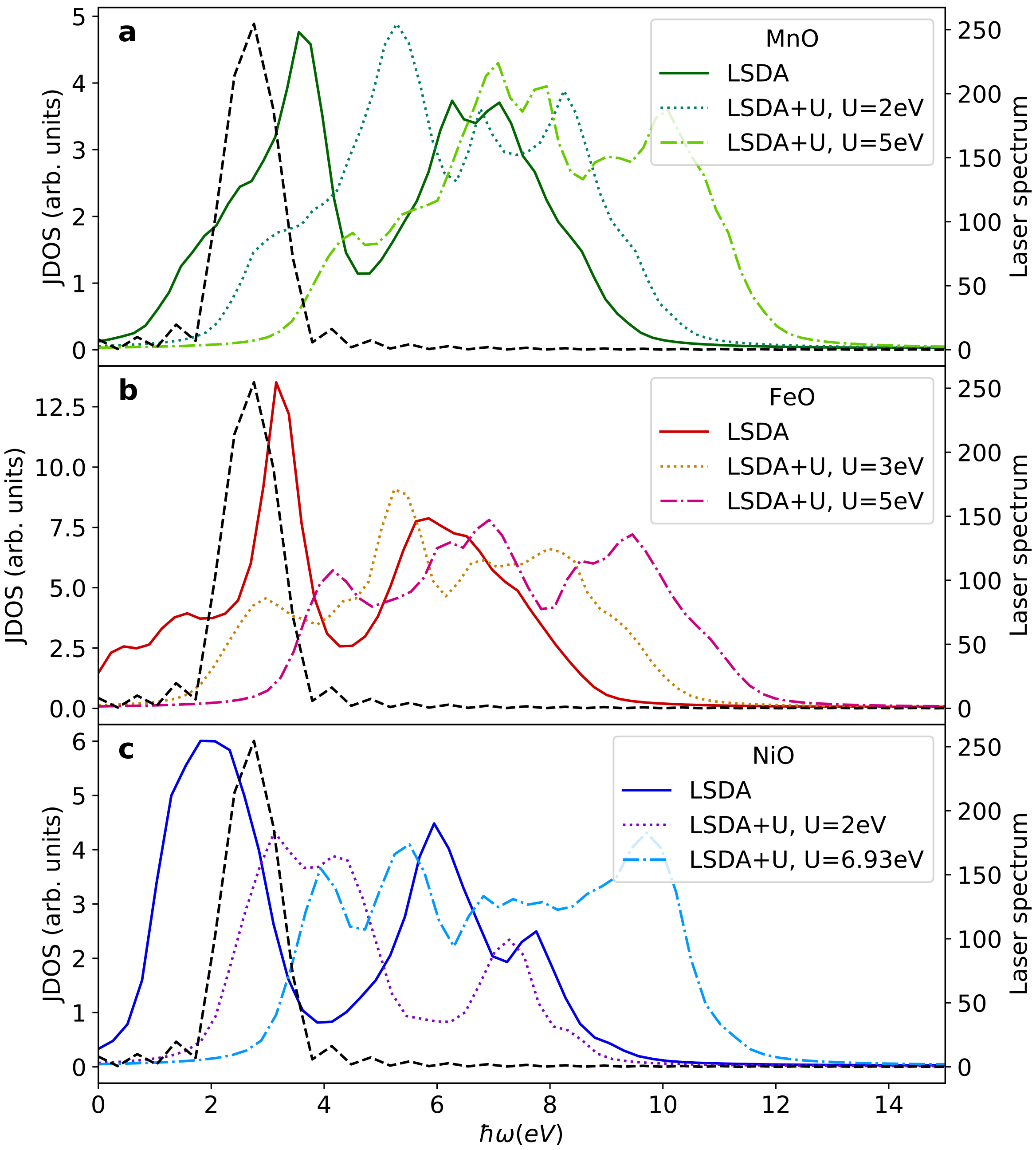

Figure 4.12: Joint density of states for the LSDA and LSDA+U cases in a) MnO, b) FeO, and c) NiO. Superimposed is the frequency spectrum of the laser pulse used (dashed line, in arbitrary units).

Returning to the JDOS, we again find a significant correlation between its strength in the areas probed by the laser field and the magnitude of demagnetization observed. For all antiferromagnets considered, the JDOS around 2.712 eV (the central frequency of the laser field used) decreases with U and so does the respective demagnetization. What's more, the JDOS changes a lot more with the Hubbard U here, for the antiferromagnets, than it does in the ferromagnets (figure 3.11). And so it is no surprise that the impact of U on the demagnetization is also much greater for the antiferromagnets than it is for the ferromagnets.

The calculations for the laser-induced demagnetization in antiferromagnetic materials reinforce our findings in the previous chapter that at the adiabatic LSDA level with frozen phonons the demagnetization observed is tightly correlated with the availability of optical transitions. The only impact the Hubbard U correction has is to shift said availability and the subsequent changes in the demagnetization dynamics are the result of that shift.

4.3 Probing different areas of the JDOS

If, at the theory level we are considering here, adiabatic LSDA, the demagnetization is simply related to optical transitions then the JDOS should have some predictive power, at least qualitatively.

In this section, we present two ways in which we can use the JDOS to predict relative levels of demagnetization and see if the picture we have, of demagnetization at the adiabatic LSDA level being driven by optical transitions, delivers on that promise. We can compare the JDOS with different U corrections over a certain frequency range and predict with which U will we observe more demagnetization. Or we can keep the theory level fixed and use laser pulses of different frequency and predict which will produce more demagnetization.

4.3.1 Using the Hubbard U

If the perturbing field is centered on a peak in the JDOS we should observe a much greater level of demagnetization than if it is centered on a valley. Consider then the JDOS for MnO around the 5 eV mark. The LSDA JDOS has a valley there and its magnitude is pretty similar to the JDOS in the LSDA+U case with a U of 5 eV. Meanwhile with a U of 2 eV the JDOS has a peak in this region. So if we apply a laser field with a central frequency of 5 eV to these three systems we expect to see similar values of demagnetization at the LSDA and $U = 5$ eV levels and more demagnetization with a U of 2 eV.

That is precisely what we see in figure 4.13. In the right panel, we see the JDOS for MnO with and without U with the spectrum of the new laser superimposed in black, to better

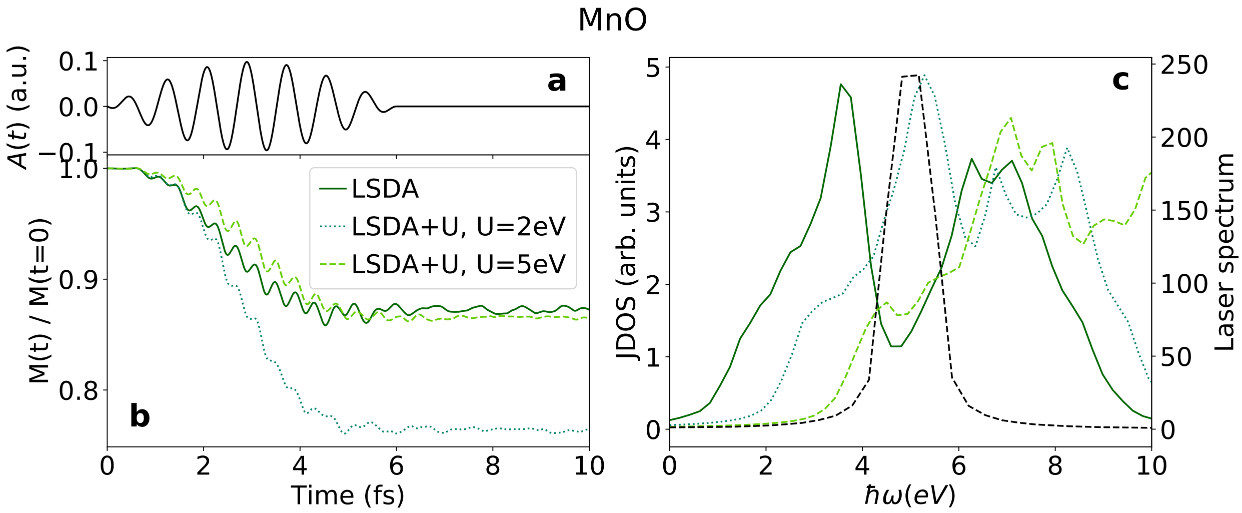

Figure 4.13: Demagnetization of MnO with a laser field of central frequency 5 eV. a) Vector potential **A**(t) of the laser pulse, b) Magnetization dynamics of MnO with standard LSDA and using LSDA+U. c) JDOS for the LSDA and LSDA+U cases in MnO. Superimposed is the frequency spectrum of the laser pulse used (black dashed line, in arbitrary units)

visualize the new area of the JDOS being probed. And on the left panel we see the results for the demagnetization dynamics with said new laser pulse and they are exactly what we expected, similar demagnetization levels with the LSDA and with a Hubbard U of 5 eV and a much greater demagnetization with an U of 2 eV.

4.3.2 Using different frequency pulses

We can also use laser pulses with different frequencies to probe different areas of the JDOS instead of keeping the laser fixed and using the Hubbard correction to change the JDOS.

Take a look, for example, at the demagnetization in NiO at the LSDA level with pulses of central frequency 1.9 eV and 4 eV as well as the original pulse of 2.712 eV, in figure 4.14.

The original pulse's spectrum peaks slightly after a big peak in the JDOS. When we apply a pulse centered on this peak in the JDOS (1.9 eV), we observe essentially the same demagnetization. Since NiO already demagnetized completely with the 2.712 eV pulse the extra transitions available do not have a discernible effect, the system cannot demagnetize more. On the other hand, when we drastically diminish the number of transitions available by applying a laser pulse centered at 4 eV, where the JDOS has a big valley, the demagnetization observed is a lot smaller, about a quarter of the demagnetization observed with the other pulses.

We have also done a version of this comparison before (obviously for ferromagnets in

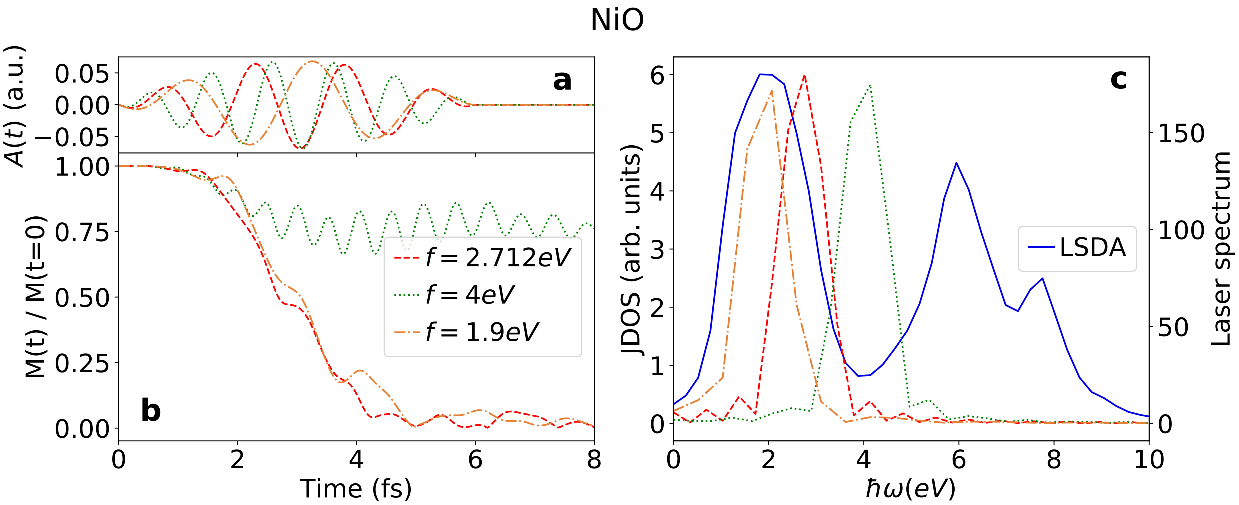

Figure 4.14: Demagnetization of NiO with laser fields of central frequency 1.9 eV, 2.712 eV and 4 eV at the LSDA level. **a**) Vector potential $\mathbf{A}(\mathrm{t})$ of the laser pulses, **b**) Magnetization dynamics of NiO with standard LSDA under the different laser pulses. **c**) JDOS for the LSDA NiO. Superimposed are the frequency spectrums of the laser pulses used (color-coded as in **a**)

section 3.3.3 but also implicitly for antiferromagnets in this section). When we chose a new laser field in figure 4.13 to better compare the demagnetization across theory levels we also ended up, in conjunction with figure 4.8, with results for the demagnetization with laser pulses of different frequency at three different levels, LSDA and LSDA+U with a U of 2 eV and 5 eV.

For all of these cases, the changes in demagnetization are what we expected. At the LSDA level, we go from pretty close to a peak, in a zone where the JDOS is relatively strong, with the laser of frequency 2.712 eV to a region where the JDOS has a local minimum and is quite less strong, with the 5 eV laser field. And the demagnetization suitably decreases from around 15% in figure 4.8 to slightly over 10% in figure 4.13. With a Hubbard U of 2 eV, the strength of the JDOS in the area covered by the spectrum increases when going from one laser field to the other, and the demagnetization also increases, from around 5% in figure 4.8 to over 20% in figure 4.13.

Thus the JDOS does have predictive power, at least in qualitative terms. All the results we have shown in this chapter are in line with our interpretation that at the adiabatic level the availability of transitions at the laser frequencies is of tremendous importance to the light-induced demagnetization dynamics.

Chapter 5

Spin-orbit coupling

In this chapter, we shift our investigation not to a new set of materials but instead to the effects of a very important term when describing demagnetization dynamics, the spin-orbit coupling.

As we alluded to in the introduction, spin-orbit mediated spin-flips are one of the possible mechanisms responsible for laser-induced ultra-fast demagnetization[7]. Given that phonons do not play a role in the calculations presented in chapters 3 and 4, SOC is the likely culprit behind the demagnetization observed at this theory level. And so it is worth it to look into it a bit more closely.

In this chapter we address how changes in the magnitude of SOC impact the results, and investigate the origins of demagnetization in our calculations.

5.1 Spin-orbit strength

So far, we have shown that at the adiabatic level the demagnetization is intimately related to the number of optical transitions available. But these are not spin-flip transitions. The actual change in the magnetization comes from SOC mediated transitions after the laser field excites the system away from equilibrium.

To gain insight into the role of the SOC in the demagnetization process we can make use of a variable in the Octopus code, `SOStrength`, that lets us choose the strength of the SOC in our calculations. So not only can we see how the demagnetization dynamics proceed if we turned the SOC off, but also if the coupling was a lot stronger than in reality.

We tried this for Ni, with the same structure and the same ground-state parameters as in chapter 3. The choice of using one of the materials studied in the previous chapters is an obvious one as it saves us the trouble of having to converge the ground state again. From those, the ferromagnets are the better choice as their simpler structure and smaller unitary

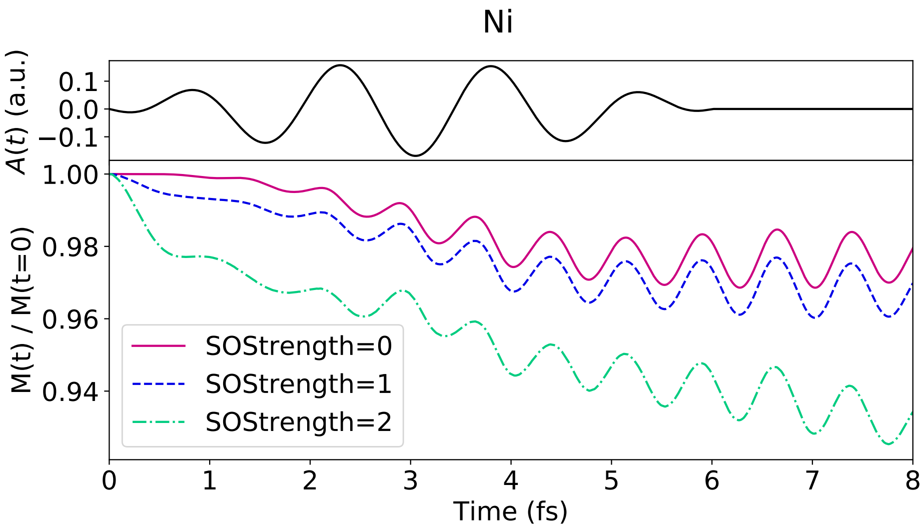

Figure 5.1: Demagnetization of fcc Ni with different strengths for the spin-orbit coupling. a) the vector potential $\mathbf{A}(\mathrm{t})$ of the laser pulse. b) the magnetization dynamics of Ni with different SOC strengths. The parameters of the laser pulse are given in the main text in chapter 3

cell mean that the calculations are performed faster. On top of that, we have found in the previous chapters that the demagnetization proceeds in much the same manner, and relates similarly to the respective electronic structure, in both ferromagnets and antiferromagnets, and so there is also no physical reason to choose the more complex system. From among Fe, Co, and Ni, we choose Ni, again for computational reasons as it offers the best compromise between **k**-point grid size and spacing used. All of this can be summarized by saying that Ni was chosen for practical computational reasons.

We also employ the same laser field as previously, detailed in chapter 3. The only difference between the results shown in figure 5.1 is the strength of the SOC. It was set to 0 in one case, and to 2 in the other, as well as the original case where it has the default value of 1.

We find that changing the strength of the SOC has a significant, but not huge, impact on the amount of demagnetization observed.

Perhaps more surprisingly, eliminating the SOC completely, i.e. setting its strength to 0, still seems to produce some demagnetization. If our calculations are truly well converged and nothing is wrong with the Octopus code, this result would contradict previous ones[7, 12], and it would mean that the LSDA would break the zero-torque theorem[68]. But not all is lost quite yet. It is perfectly possible that the demagnetization observed in this case is only the product of the excitation of electrons to the outside of the integration spheres, that is, the demagnetization plotted in figure 5.1 for the `SOStrength` = 0 case is not legitimate, it

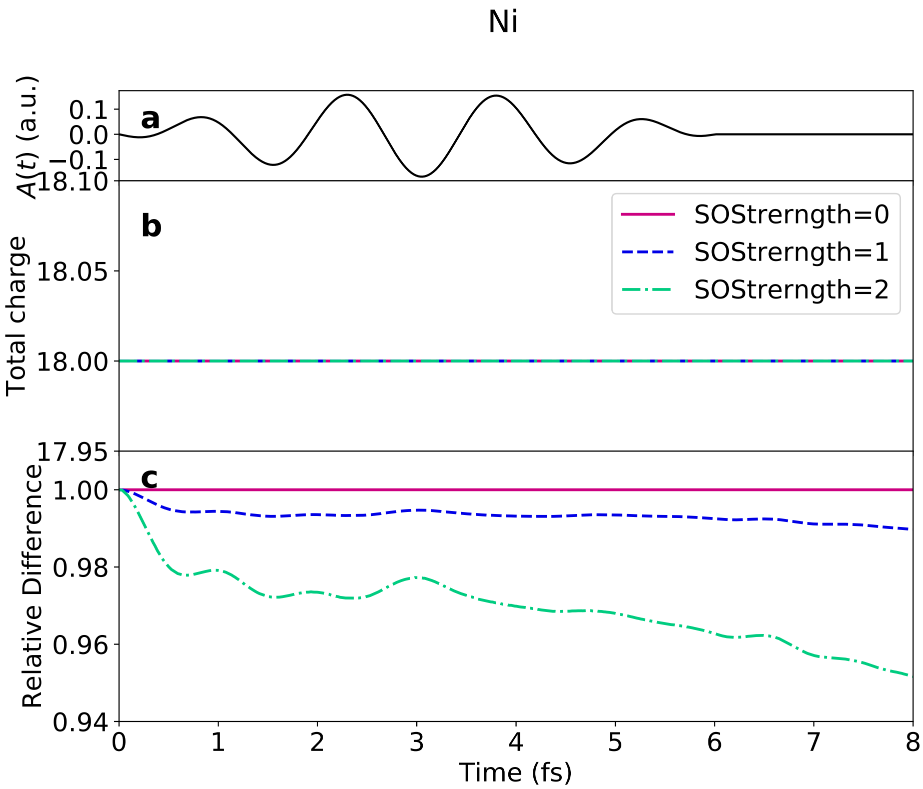

Figure 5.2: a) the vector potential $\mathbf{A}$(t) of the laser pulse b) Total charge c) Relative difference of the majority and minority charges. The exact meaning of this quantity is discussed in more detail in the main text.

is only an artifact of the way the magnetization is calculated in Octopus.

To confirm this hypothesis we plot, in figure 5.2, different integrals of $n_{\alpha\beta}$, at the different `SOStrength` levels.

In section b) of figure 5.2 we plot the total charge, i.e. the integral of n^{Tr} (see equation 2.12), over the entire simulation box. As we can see, the total number of electrons remains constant throughout the propagation in all cases. This assures us that the code is working properly, the propagation is stable, and we are not creating or destroying electrons. Moreover 18 is the number of non-core electrons in Ni in the pseudopotentials we are using.

In section c) we plot the integral of $n_{\uparrow\uparrow}(t) - n_{\downarrow\downarrow}(t)$, relative to its value at $t = 0$. This quantity is related to the z component of the magnetization[24]. We can now confirm that the demagnetization without SOC in figure 5.1 is truly spurious. And when we turn on SOC there is indeed some legitimate demagnetization, even if not much.

So if we consider the entire simulation box and integrate over it, we confirm that our calculations are well converged and they agree with previous results. Our results also strengthen the idea that SOC mediated spin-flips are an important part of laser-induced demagnetization, though far from being the only process involved. After all, even with double the SOC, the demagnetization we observe in Ni is still very far from the experimental one[55].

The type of analysis done in figure 5.2 is only possible because we only use one atom in the unit cell. The same plot for the antiferromagnets we studied in chapter 4 would not provide us with any insightful information. The total magnetization is always zero, regardless of the demagnetization dynamics of each atom.

This raises a question regarding the code we have been using, Octopus. Spheres are clearly not the best volume to use when integrating the local magnetic moments, as they do not cover the entire space. This is something that should be changed in the future, perhaps by using Voronoi cells.

Chapter 6

Conclusion

We have employed the LSDA+U method to investigate how the description of correlations, and therefore how changes to the bandstructure caused by it, impacts the light-induced demagnetization on a number of materials. Specifically, we considered the elemental ferromagnetic transition metals Fe, Co, and Ni, as well as the antiferromagnetic transition metal oxides MnO, FeO, and NiO.

In all cases, we found that the Hubbard U correction produces significant changes in the amount of demagnetization observed. The overall impact is greater for the oxides, where the amount of demagnetization observed is also much larger, but is still considerable in the ferromagnetic materials. And yet the results we have presented in this thesis are still very far off from the experimental ones, especially for the elemental ferromagnetic metals. A correct description of electronic correlations is an important piece in correctly representing light-induced demagnetization with *ab initio* methods but it is also clear that there is a myriad of other processes and effects that further contribute to the demagnetization and need to be addressed in the future. One clear example of a process that certainly plays an important part, yet we fail to account for it in our calculations, is the interaction with the phononic system.This is clearly an area that deserves further investigation in the future.

We have established a relationship between the amount of demagnetization observed in our calculations and the JDOS of the material in question in the energy range of the laser pulse used. That is, in our calculations, for both ferro and antiferromagnets, the system demagnetizes more when there are more transitions available at the laser frequencies. This holds for all the material studied across all the theory levels used. In fact, this is the reason for the changes in the demagnetization when the Hubbard U is applied. The Hubbard U changes the JDOS and the demagnetization changes accordingly, which is why the effects of applying the U are not always the same. Sometimes the demagnetization increases, sometimes it decreases, depending on the material in question and the laser pulse applied. It is also why the effect of the Hubbard correction is more pronounced in the antiferromagnets we studied, it has a bigger impact on their electronic structure

We investigated this relationship further by performing several calculations where we change different laser parameters and see how each impacts the demagnetization. In every single one of these calculations, the system demagnetizes more when there are more transitions available, be it (1) from a change in the DOS in the region of the laser spectrum, whether that change is from the Hubbard U changing the DOS or from shifting the spectrum by using a different central frequency, (2) from an increase in the area covered by the laser spectrum because the pulse is shorter, or (3) just simply because there are more photons in the laser field due to its intensity increasing.

One interesting corollary of our investigation into the impact of different pulse parameters on the demagnetization is that for sufficiently short pulses the fluence ceases to be a good descriptor. These pulses are so short that their spectrum covers a region where the JDOS changes significantly and so one needs to be careful about how each laser parameter individually affects its spectrum. It is possible to have pulses with the same fluence produce different demagnetization levels.

We have confirmed that SOC is crucial when simulating demagnetization, as without it no demagnetization takes place. But it is also clear from our calculations that at the LSDA level a lot of other information is still missing. We have also found an issue in the Octopus code that affects slightly the results produced. To solve it the way the magnetization is calculated in the Octopus code should be tweaked.

One can continue to investigate the role of correlations in the demagnetization dynamics by employing more sophisticated corrections, like an *ab initio* time-dependent U[36].As for the broader field of light-induced demagnetization, the adiabatic approximation is clearly a crude one when dealing with the ultrafast, high-intensity laser pulses used in it, and so another area that should be further looked into is to develop and use better functionals that take into consideration memory effects. Moreover, there is already evidence that such memory effects play a key role in demagnetization[16]. Exchange-correlation functionals with non-zero exchange torque could also help elucidate the role of optical torques in the demagnetization process and so it is worth it to invest in their development and use for non-colinear magnetism.

One thing is for certain, the adiabatic LSDA, even with a static U is very far off from accurately describing the physics we observe in experiment. Which is not to say that it is completely unusable. It does produce some demagnetization, and as we have seen it does highlight the importance of SOC in the demagnetization process as well as the role of spin-flip transitions in it. And we have used it to produce insights into the relationship between the magnitude of demagnetization and the availability of optical transitions. But it is clear, and this work helps cement this fact, that time-dependent DFT simulations with adiabatic functionals, and with only simple corrections to it, are not the most accurate tools to describe real-world light-induced demagnetization, even if they do offer some insights.

Appendix A

Ground-state convergence in ferromagnets

In chapter 3 not all plots for the ground-state convergence are shown. This would have been too repetitive in the main text. And yet, as we stressed out in that chapter, the proper convergence of the ground-state is vital. In this appendix we present the plots regarding the ground-state convergence in ferromagnets missing from chapter 3.

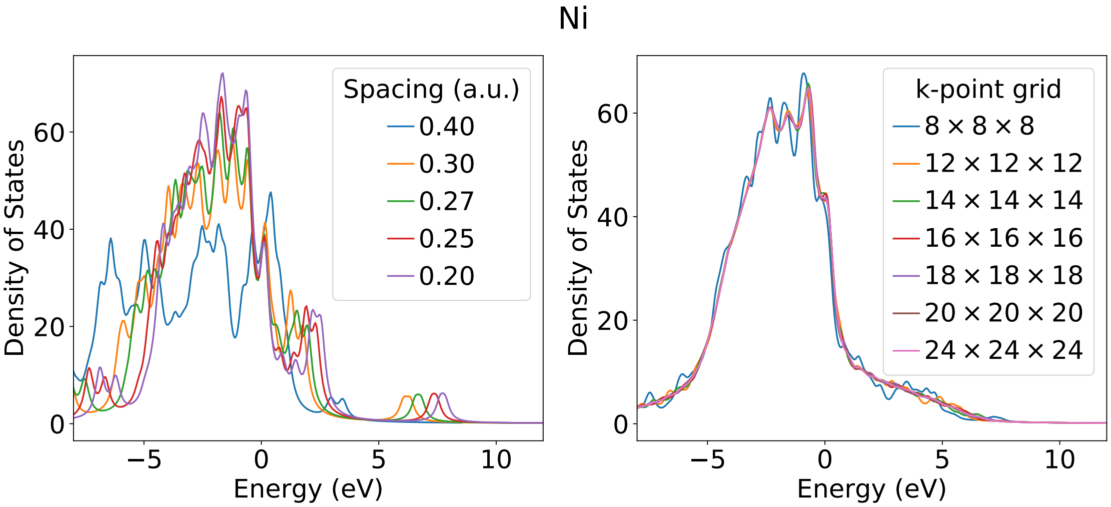

Figure A.1: Convergence of the density of states of Co with regards to the spacing (left panel) and to the **k**-point grid used (right panel). In both panels 0 corresponds to the Fermi energy

The convergence of the DOS with both the spacing and the **k**-point grid for Ni is the only one missing in the main text and is shown here, in figure A.1. The results follow much the same trend as those of Fe and Co, discussed in the main text.

For the convergence of the demagnetization, ensured by doing short propagations with

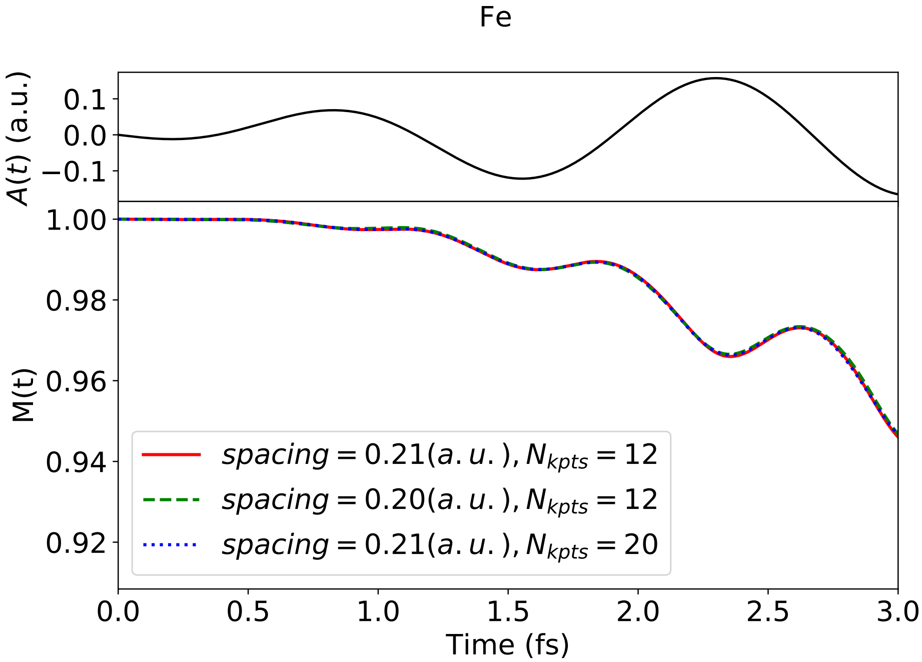

Figure A.2: Short propagation of the relative magnetization in Fe with different parameters. The upper panel shows the vector potential $\mathbf{A}(t)$ of the laser pulse and the lower panel the various dynamics. The results are nearly the same with different spacing and **k**-point grid which means the calculations are well converged.

different spacing values and different **k**-point grids, only the results for Ni are shown in chapter 3. The results for Fe and Co (figures A.2 and A.3 respectively) are similar the the Ni ones (figure 3.5).

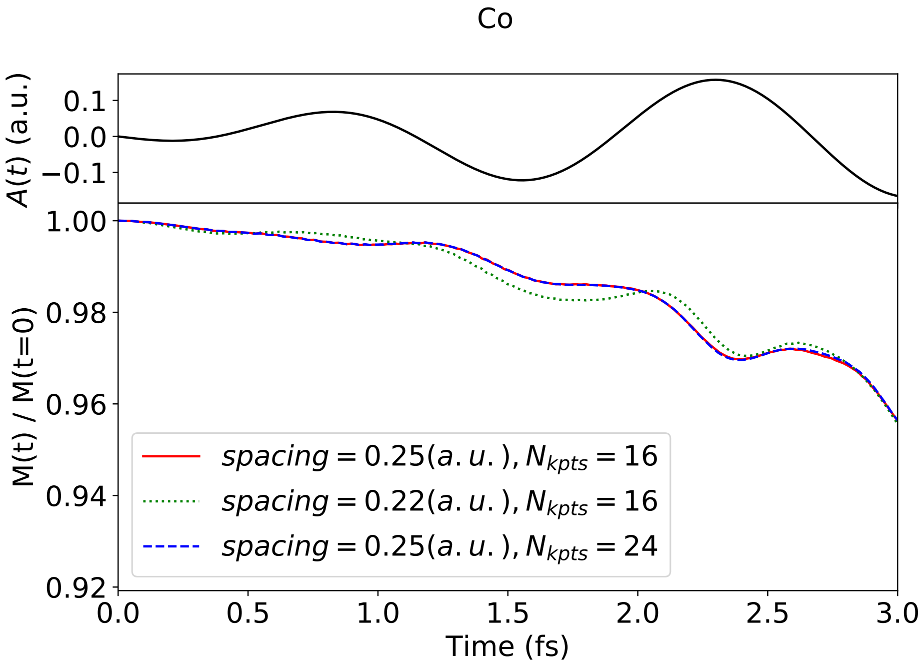

Figure A.3: Short propagation of the relative magnetization in Co with different parameters. The upper panel shows the vector potential $\mathbf{A}$(t) of the laser pulse and the lower panel the various dynamics. The results are nearly the same with different spacing and **k**-point grid which means the calculations are well converged.

Appendix B

LSDA+U results for Co and Ni

The effects of the Hubbard U correction on the ground-state DOS for Co and Ni are not shown in chapter 3. Only Fe is shown there because the results are more pronounced in it. The results for Co and Ni are shown in this appendix (figures B.1 and B.2). Similarly to the Fe case discussed in chapter 3, the LSDA results are closer to experiment and the Hubbard U shifts them away.

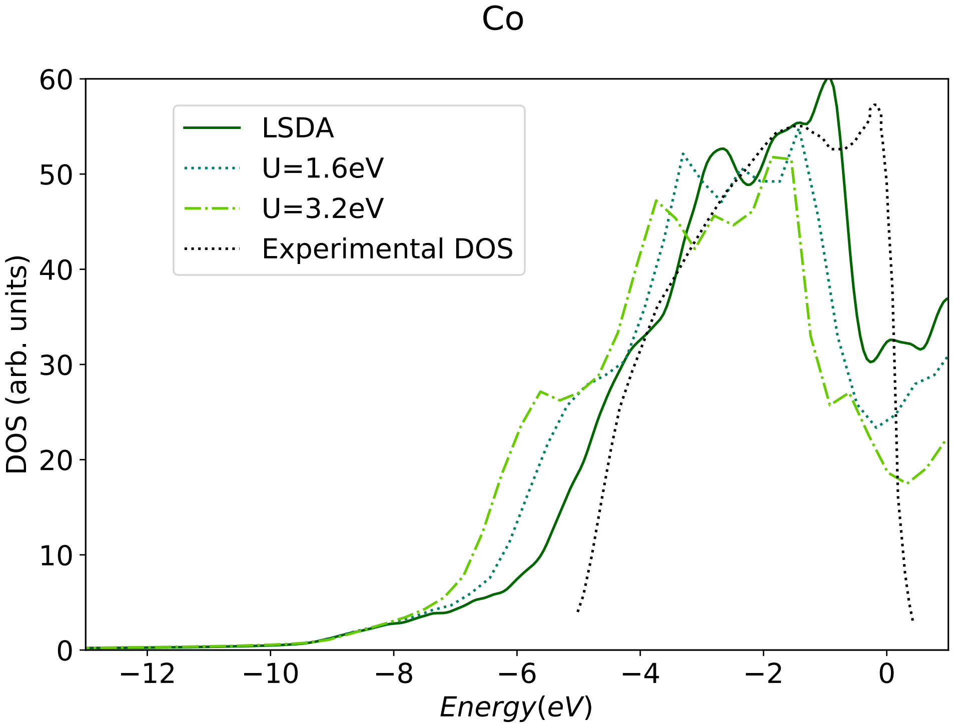

Figure B.1: Comparison of the Co DOS calculated using the LDA and different U values with experimental data.

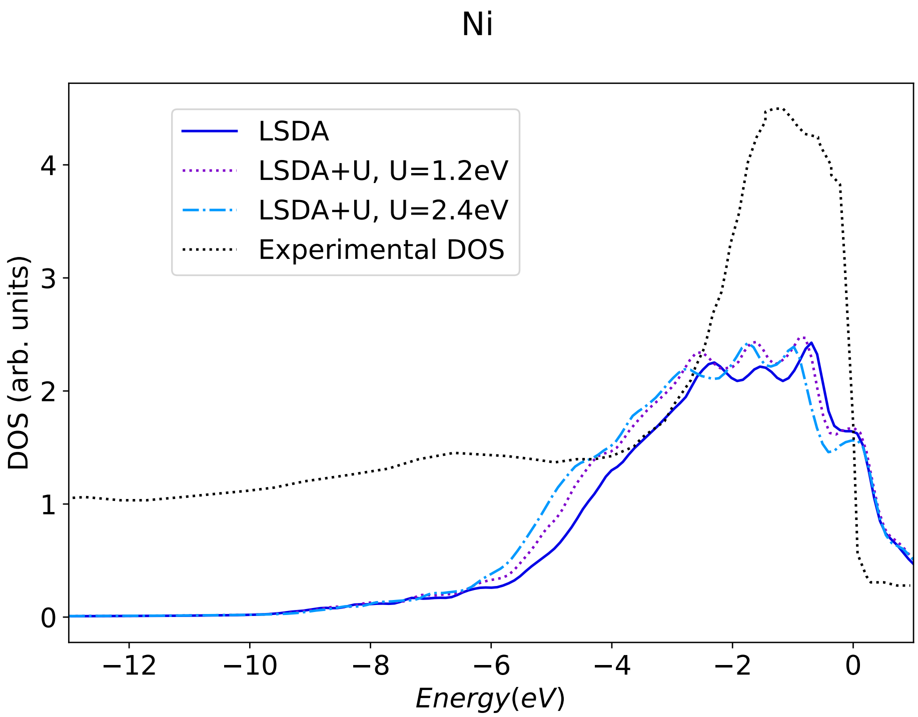

Figure B.2: Comparison of the Ni DOS calculated using the LDA and different U values with experimental data.

The dynamics of the energy are also missing for Co and Ni in chapter 3. These results (figures B.3 and B.4) are also similar to the analogous Fe ones. The energy at the end of the pulse is higher for Co and Ni in the cases where it demagnetizes more, like in the Fe case. The energy also remains constant after the pulse which means the time-step was properly converged for Co and Ni as well.

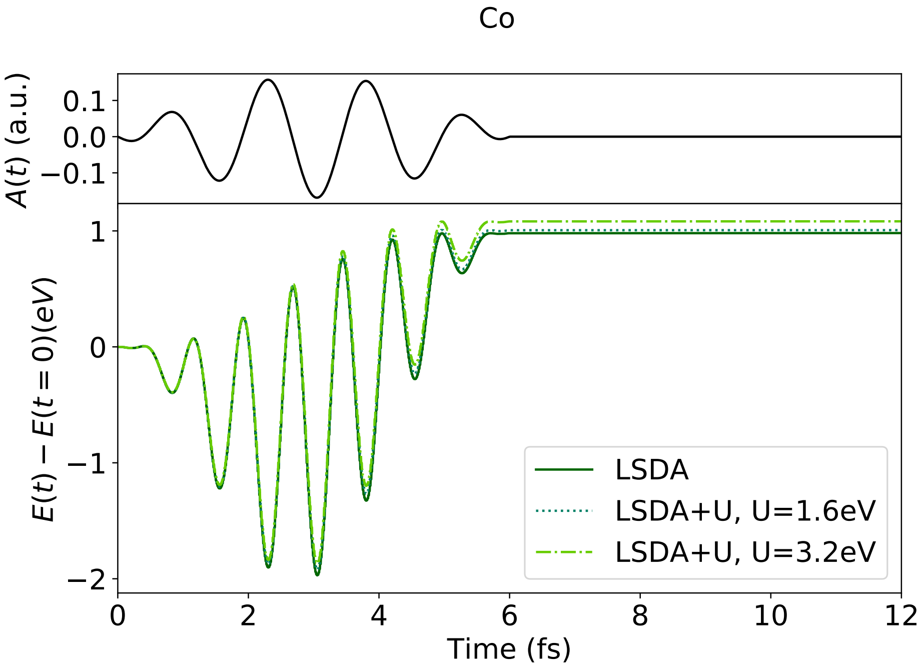

Figure B.3: Energy dynamics for Co in both the LSDA and LSDA+U cases.

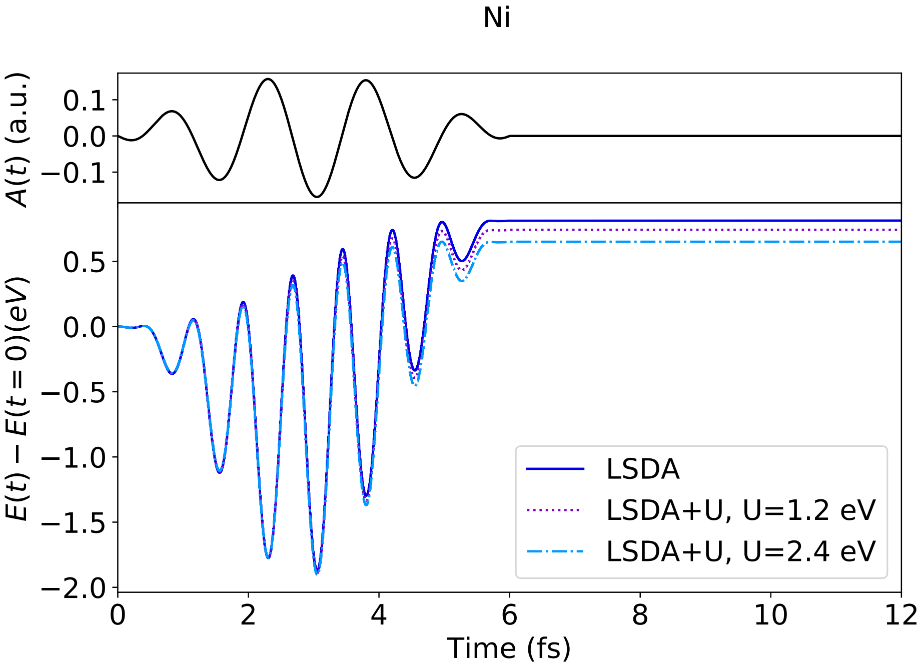

Figure B.4: Energy dynamics for Ni in both the LSDA and LSDA+U cases.

Appendix C

Demagnetization in Co under laser pulses of varying intensity

Like for Ni, in figure 3.13, the demagnetization in Co was also investigated under laser pulses with different intensities and the same pulse duration and central frequency. This is depicted in figure C.1.

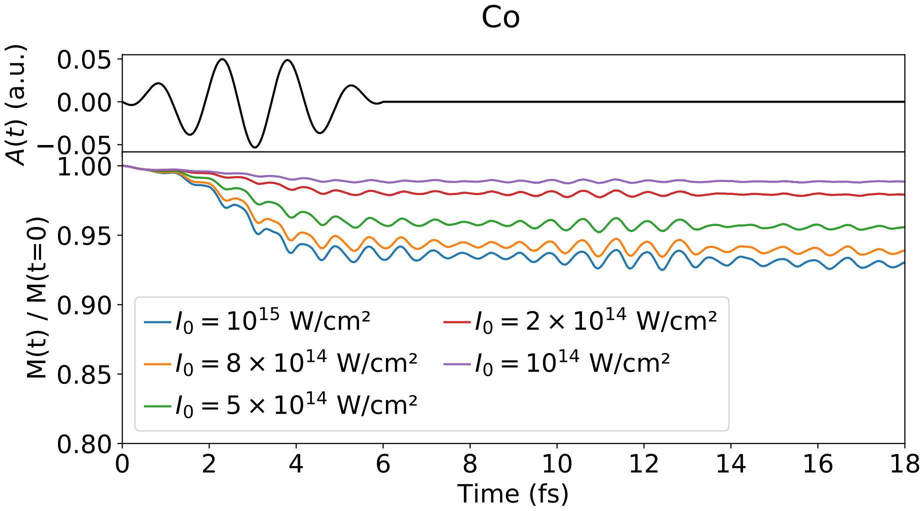

Figure C.1: Upper panel: Laser pulse shape. Lower panel: Time evolution of the relative magnetic moment for Co under the influence of laser field of varying peak intensity.

Also as in the Ni case, the demagnetization increases with increased intensity but it deviates more form the linear scaling (figure C.2). The most intense pulse is 10 times more intense than the least intense one but Co only demagnetizes approximately 6.3 times more.

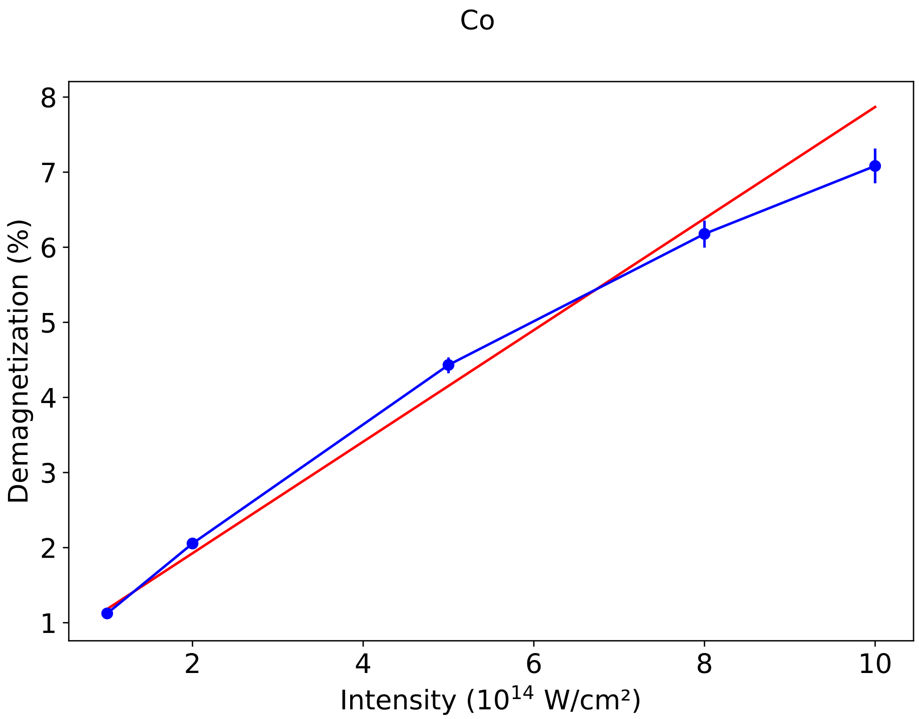

Figure C.2: Demagnetization as a function of peak intensity for Co. The red line is a guide to the eyes.

Appendix D

Ground state convergence in MnO and NiO

In the antiferromagnetic case, once again not all plots regarding the ground state convergence were shown in chapter 4. In that chapter only the convergence of FeO is presented. The extra plots for the convergence of MnO and NiO are presented in this appendix.

For the convergence of the DOS with both the spacing and the **k**-point grid see figure D.1 for MnO and figure D.2 for NiO.

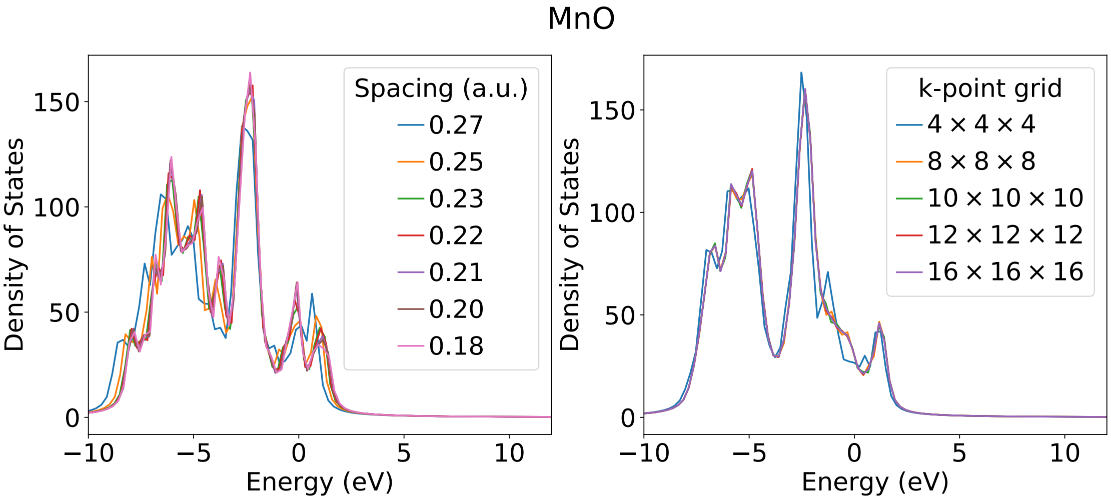

Figure D.1: Convergence of the density of states of MnO with regards to the spacing (left panel) and to the **k**-point grid used (right panel). In both panels 0 corresponds to the Fermi energy

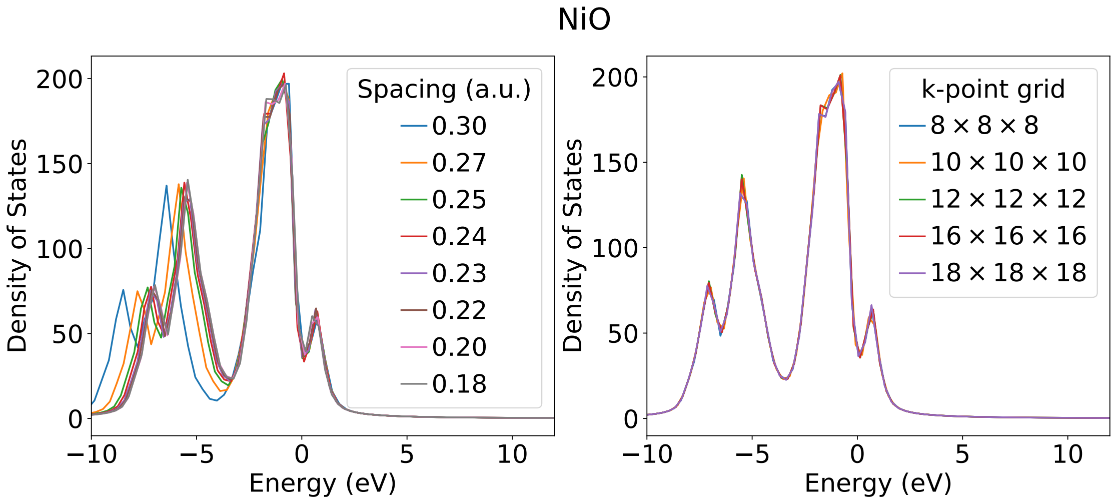

Figure D.2: Convergence of the density of states of NiO with regards to the spacing (left panel) and to the **k**-point grid used (right panel). In both panels 0 corresponds to the Fermi energy

For the convergence of the demagnetization dynamics see figures D.3 and D.4 for MnO and NiO respectively.

The results in this appendix follow closely those of FeO, discussed in more detail in chapter 4.

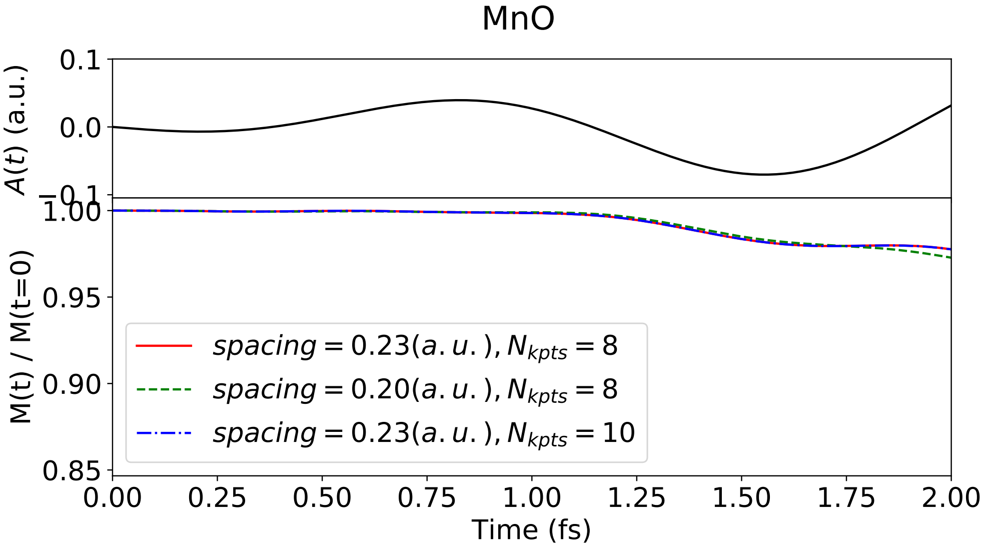

Figure D.3: Short propagation of the relative magnetization in MnO in the LDA with different parameters. The upper panel shows the vector potential $\mathbf{A}(\mathrm{t})$ of the laser pulse and the lower panel the various dynamics.

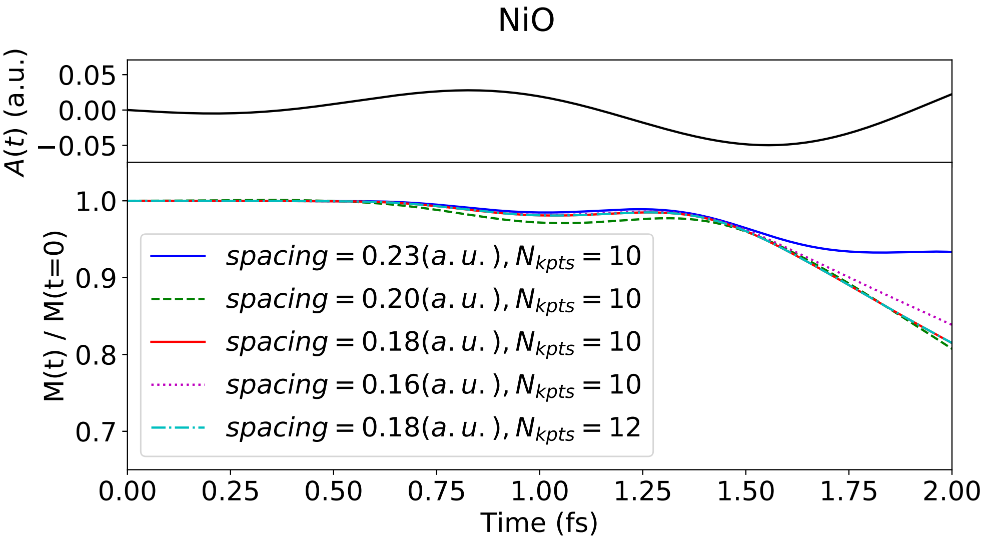

Figure D.4: Short propagation of the relative magnetization in NiO in the LDA with different parameters. The upper panel shows the vector potential $\mathbf{A}(\mathrm{t})$ of the laser pulse and the lower panel the various dynamics.

Appendix E

LSDA+U results for the antiferromagnets

In this appendix we show extra plots for the DOS of MnO and NiO at both the LSDA and LSDA+U level. These plots (figures E.1 and E.2) are analogous to figure 4.6 for FeO.

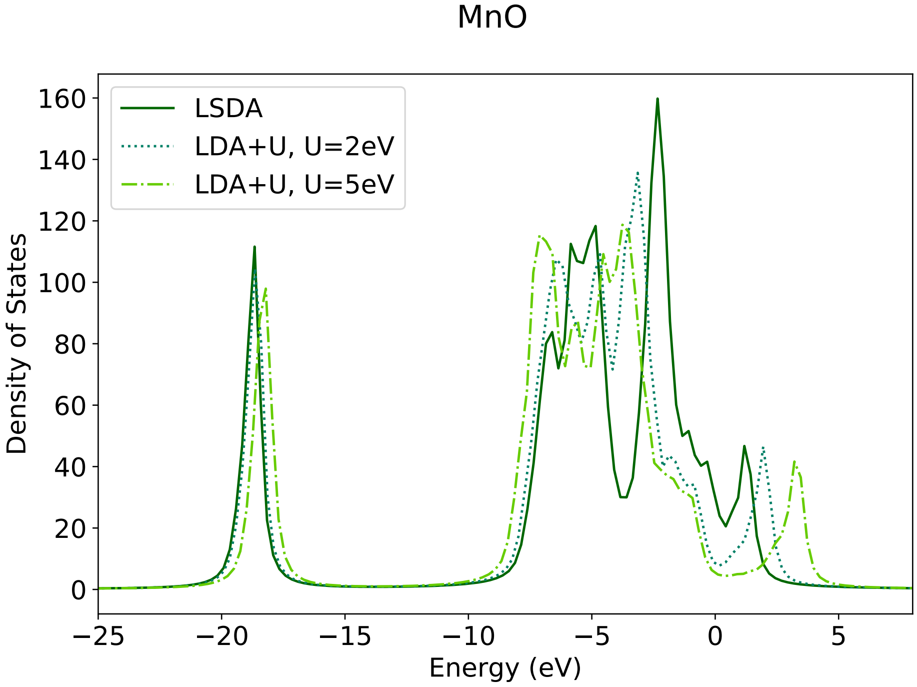

Figure E.1: DOS for MnO in the LSDA and LSDA+U cases. In all cases the 0 of the energy corresponds to the Fermi level. Note how the system goes from metallic at the LSDA level to insulating at the LSDA+U level

Similarly to the FeO case discussed in the main text, the Hubbard U correction produces the correct insulator state as opposed to the metallic state produced by the LSDA.

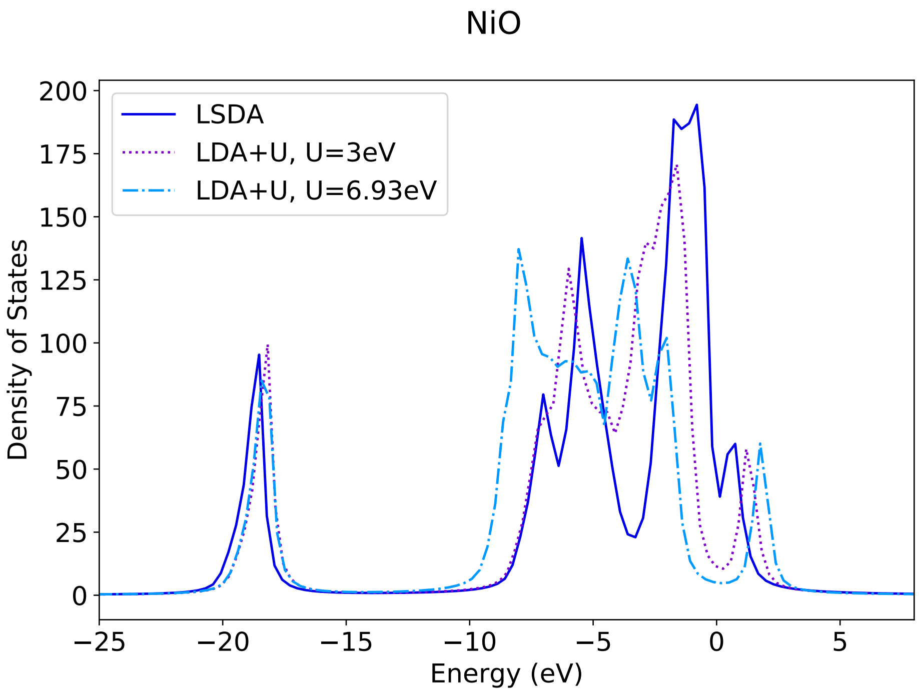

Figure E.2: DOS for NiO in the LSDA and LSDA+U cases. In all cases the 0 of the energy corresponds to the Fermi level. Note how the system goes from metallic at the LSDA level to insulating at the LSDA+U level

The energy dynamics for MnO and FeO are plotted in figures E.3 and E.4.

As in previous cases the system demagnetizes more when it absorbs more energy and the time-step selected was adequate as the energy remains constant after the laser pulse.

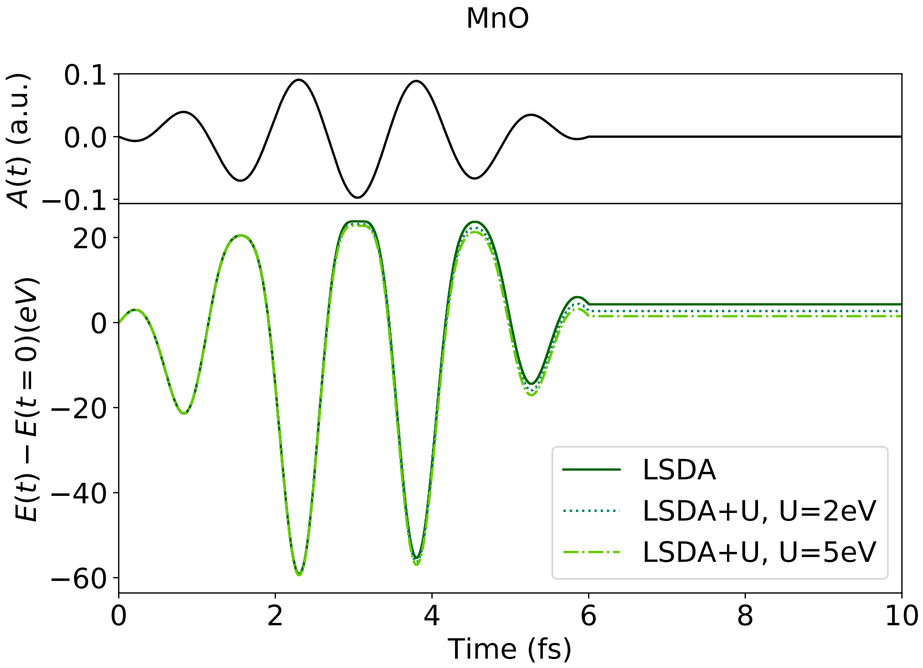

Figure E.3: Energy dynamics for MnO in both the LSDA and LSDA+U cases.

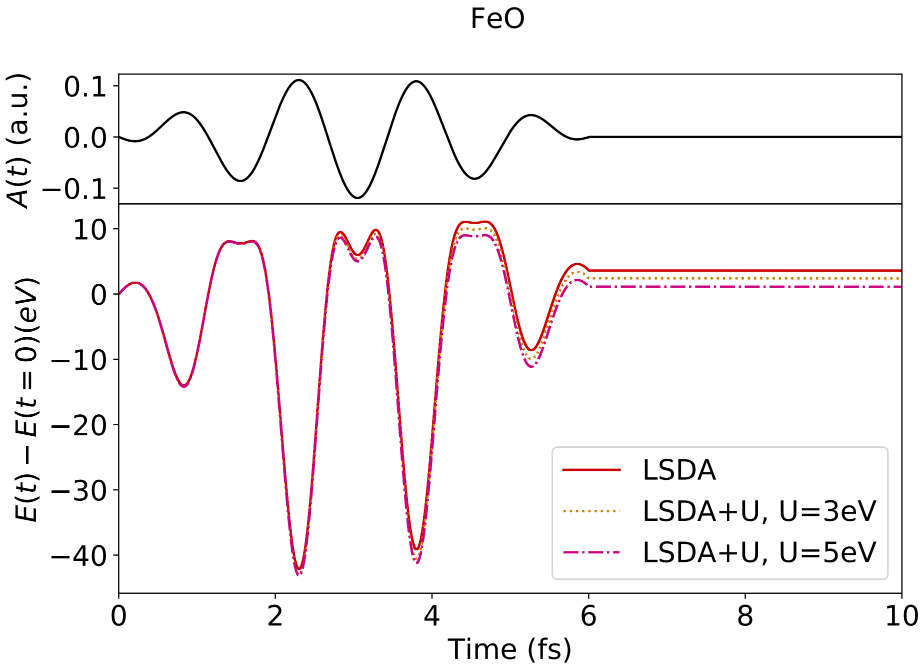

Figure E.4: Energy dynamics for FeO in both the LSDA and LSDA+U cases.

Bibliography

[1] E. Beaurepaire, J.-C. Merle, A. Daunois, and J.-Y. Bigot, Physical Review Letters **76**, 4250 (1996).

[2] A. Kirilyuk, A. V. Kimel, and T. Rasing, Reviews of Modern Physics **82**, 2731 (2010).

[3] A. El-Ghazaly, J. Gorchon, R. B. Wilson, A. Pattabi, and J. Bokor, Journal of Magnetism and Magnetic Materials **502**, 166478 (2020).

[4] H. Vonesch and J.-Y. Bigot, Physical Review B **85**, 180407 (2012).

[5] M. Battiato, K. Carva, and P. M. Oppeneer, Physical Review Letters **105**, 027203 (2010).

[6] B. Koopmans, J. Ruigrok, F. Dalla Longa, and W. De Jonge, Physical Review Letters **95**, 267207 (2005).

[7] G. Zhang and W. Hübner, Physical Review Letters **85**, 3025 (2000).

[8] V. Shokeen, M. Sanchez Piaia, J.-Y. Bigot, T. Müller, P. Elliott, J. K. Dewhurst, S. Sharma, and E. K. U. Gross, Physical Review Letters **119**, 107203 (2017).

[9] K. Krieger, P. Elliott, T. Müller, N. Singh, J. Dewhurst, E. Gross, and S. Sharma, Journal of Physics: Condensed Matter **29**, 224001 (2017).

[10] G. E. Topp, N. Tancogne-Dejean, A. F. Kemper, A. Rubio, and M. A. Sentef, Nature communications **9**, 1 (2018).

[11] K. Krieger, J. Dewhurst, P. Elliott, S. Sharma, and E. Gross, Journal of Chemical Theory and Computation **11**, 4870 (2015).

[12] M. Stamenova, J. Simoni, and S. Sanvito, Physical Review B **94**, 014423 (2016).

[13] W. Kohn and L. J. Sham, Physical Review **140**, A1133 (1965).

[14] M. Ekholm, D. Gambino, H. J. M. Jönsson, F. Tasnádi, B. Alling, and I. A. Abrikosov, Physical Review B **98**, 094413 (2018).

[15] G. Zhang, Y. Bai, and T. F. George, Journal of Physics: Condensed Matter **28**, 236004 (2016).

[16] S. R. Acharya, V. Turkowski, G. P. Zhang, and T. S. Rahman, Physical Review Letters **125**, 017202 (2020).

[17] S. Sharma, S. Shallcross, P. Elliott, and J. Dewhurst, arXiv preprint arXiv:2203.14234 (2022).

[18] P. Tengdin, W. You, C. Chen, X. Shi, D. Zusin, Y. Zhang, C. Gentry, A. Blonsky, M. Keller, P. M. Oppeneer, *et al.*, Science Advances **4**, eaap9744 (2018).

[19] G. Zhang, Y. Bai, W. Hübner, G. Lefkidis, and T. F. George, Journal of Applied Physics **103**, 07B113 (2008).

[20] F. Heiße, F. Köhler-Langes, S. Rau, J. Hou, S. Junck, A. Kracke, A. Mooser, W. Quint, S. Ulmer, G. Werth, *et al.*, Physical Review Letters **119**, 033001 (2017).

[21] M. A. Marques, N. T. Maitra, F. M. Nogueira, E. K. Gross, and A. Rubio, *Fundamentals of time-dependent density functional theory*, Vol. 837 (Springer, 2012).

[22] P. Hohenberg and W. Kohn, Physical Review **136**, B864 (1964).

[23] J. Kubler, K.-H. Hock, J. Sticht, and A. Williams, Journal of Physics F: Metal Physics **18**, 469 (1988).

[24] C. A. Ullrich, Physical Review B **98**, 035140 (2018).

[25] D. Hobbs, G. Kresse, and J. Hafner, Physical Review B **62**, 11556 (2000).

[26] M. A. Marques, M. J. Oliveira, and T. Burnus, Computer Physics Communications **183**, 2272 (2012).

[27] N. Mardirossian and M. Head-Gordon, Molecular Physics **115**, 2315 (2017).

[28] D. M. Ceperley and B. J. Alder, Physical Review Letters **45**, 566 (1980).

[29] X. Andrade, D. Strubbe, U. De Giovannini, A. H. Larsen, M. J. T. Oliveira, J. Alberdi-Rodriguez, A. Varas, I. Theophilou, N. Helbig, M. J. Verstraete, L. Stella, F. Nogueira, A. Aspuru-Guzik, A. Castro, M. A. L. Marques, and A. Rubio, Physical Chemistry Chemical Physics **17**, 31371 (2015).

[30] M. Imada, A. Fujimori, and Y. Tokura, Reviews of Modern Physics **70**, 1039 (1998).

[31] V. I. Anisimov, J. Zaanen, and O. K. Andersen, Physical Review B **44**, 943 (1991).

[32] V. I. Anisimov, I. Solovyev, M. Korotin, M. Czyżyk, and G. Sawatzky, Physical Review B **48**, 16929 (1993).

[33] I. Solovyev, P. Dederichs, and V. Anisimov, Physical Review B **50**, 16861 (1994).

[34] S. L. Dudarev, G. A. Botton, S. Y. Savrasov, C. J. Humphreys, and A. P. Sutton, Physical Review B **57**, 1505 (1998).

[35] N. Tancogne-Dejean, M. J. Oliveira, and A. Rubio, Physical Review B **96**, 245133 (2017).

[36] L. A. Agapito, S. Curtarolo, and M. B. Nardelli, Physical Review X **5**, 011006 (2015).

[37] E. Runge and E. K. Gross, Physical Review Letters **52**, 997 (1984).

[38] C. Fiolhais, F. Nogueira, and M. A. Marques, *A primer in density functional theory*, Vol. 620 (Springer Science & Business Media, 2003).

[39] A. Castro, M. A. Marques, and A. Rubio, The Journal of Chemical Physics **121**, 3425 (2004).

[40] A. Gomez Pueyo, M. A. Marques, A. Rubio, and A. Castro, Journal of Chemical Theory and Computation **14**, 3040 (2018).

[41] M. Hochbruck and C. Lubich, SIAM Journal on Numerical Analysis **34**, 1911 (1997).

[42] C. Moler and C. Van Loan, SIAM review **45**, 3 (2003).

[43] C. Hartwigsen, S. Gœdecker, and J. Hutter, Physical Review B **58**, 3641 (1998).

[44] A. Jain, S. P. Ong, G. Hautier, W. Chen, W. D. Richards, S. Dacek, S. Cholia, D. Gunter, D. Skinner, G. Ceder, *et al.*, APL Materials **1**, 011002 (2013).

[45] F. Siegrist, J. A. Gessner, M. Ossiander, C. Denker, Y.-P. Chang, M. C. Schröder, A. Guggenmos, Y. Cui, J. Walowski, U. Martens, *et al.*, Nature **571**, 240 (2019).

[46] A. Grechnev, I. Di Marco, M. Katsnelson, A. Lichtenstein, J. Wills, and O. Eriksson, Physical Review B **76**, 035107 (2007).

[47] Y. S. Mohammed, Y. Yan, H. Wang, K. Li, and X. Du, Journal of Magnetism and Magnetic Materials **322**, 653 (2010).

[48] A. Vega and W. Nolting, Physica Status Solidi (b) **193**, 177 (1996).

[49] B. Sinković, E. Shekel, and S. Hulbert, Physical Review B **52**, R8696 (1995).

[50] M. Cococcioni and S. De Gironcoli, Physical Review B **71**, 035105 (2005).

[51] V. Anisimov and O. Gunnarsson, Physical Review B **43**, 7570 (1991).

[52] J. Callaway and C. Wang, Physical Review B **16**, 2095 (1977).

[53] J. Crangle, The London, Edinburgh, and Dublin Philosophical Magazine and Journal of Science **46**, 499 (1955).

[54] C. Kittel, *Introduction to Solid State Physics* (Wiley, New York, 1986).

[55] T. Roth, A. Schellekens, S. Alebrand, O. Schmitt, D. Steil, B. Koopmans, M. Cinchetti, and M. Aeschlimann, Physical Review X **2**, 021006 (2012).

[56] C. Stamm, N. Pontius, T. Kachel, M. Wietstruk, and H. Dürr, Physical Review B **81**, 104425 (2010).

[57] J. K. Dewhurst, A. Sanna, and S. Sharma, The European Physical Journal B **91**, 1 (2018).

[58] A. Kimel, A. Kirilyuk, A. Tsvetkov, R. Pisarev, and T. Rasing, Nature **429**, 850 (2004).

[59] B. Ivanov, Low Temperature Physics **40**, 91 (2014).

[60] K. Terakura, T. Oguchi, A. Williams, and J. Kübler, Physical Review B **30**, 4734 (1984).

[61] K. Terakura, A. Williams, T. Oguchi, and J. Kübler, Physical Review Letters **52**, 1830 (1984).

[62] F. J. Ferraro, *Magnetic anisotropies and exchange bias in ultrathin cobalt layers for the tunnel anisotropic magnetoresistance*, Ph.D. thesis, Université Grenoble Alpes (2015).

[63] M. Forti, P. Alonso, P. Gargano, and G. Rubiolo, Procedia Materials Science **1**, 230 (2012).

[64] Z. Fang, I. V. Solovyev, H. Sawada, and K. Terakura, Physical Review B **59**, 762 (1999).

[65] A. K. Cheetham and D. A. O. Hope, Physical Review B **27**, 6964 (1983).

[66] H. Fjellvag, B. C. Hauback, T. Vogt, and S. Stølen, American Mineralogist **87**, 347 (2002).

[67] P. Dufek, P. Blaha, V. Sliwko, and K. Schwarz, Physical Review B **49**, 10170 (1994).

[68] K. Capelle, G. Vignale, and B. L. Györffy, Physical Review Letters **87**, 206403 (2001).

List of Publications

1. R. Hussein, J. Schmidt, T. Barros, M. Marques, and S. Botti, Machine-learning correction to density-functional crystal structure optimization. MRS Bulletin 47, 765–771 (2022).
2. T. Barros, N. Tancogne-Dejean, J. Berakdar and M. Marques, Impact of electron correlation on the light-induced demagnetization of elemental ferromagnetic metals. The European Physical Journal B, 95(10), 1-8, (2022).

Acknowledgements

First and foremost I would like to thank my supervisor, Prof. Dr. Miguel Marques, for everything, especially for going way beyond what was expected.

I would also like to thank everyone that helped me in my academic journey, particularly Dr. Nicolas Tancogne-Dejean.

Thank you as well to all of my friends and colleagues, for all of their friendship and support.

I would like to thank all of my family as well, for always making sure home was not far away.

Finally, I would like to thank my parents. For their support, for their sacrifices, for their help, for their love. Obrigado.

Lebenslauf / Curriculum Vitae

Persönliche Daten / Personal data

Name	Tomás Périé de Barros
Geburtsdatum / Date of birth	09.01.1995
Geburstort / Place of birth	Coimbra, Portugal
Staatsangehörigkeit / Nationality	Portugiesisch / Portuguese
Adresse / Address	Reilstrasse 129, 06114 Halle (Saale), Germany
E-mail	tomas.perie-de-barros@physik.uni-halle.de

Bildung / Education

04.2019 - Present	PhD in Physics Martin-Luther University Halle-Wittenberg, Germany Supervisor: Miguel A. L. Marques
09.2016 - 10.2018	Master's degree in Physics specialization in Condensed Matter Physics University of Coimbra, Portugal Master thesis: "Time-dependent local density of states as a tool to study optical response" Supervisor: Fernando M. S. Nogueira
09.2013 - 07.2016	Bachelor's degree in Physics University of Coimbra, Portugal
09.2010 - 07.2013	High School Escola Secundária Dr. Joaquim de Carvalho, Figueira da Foz, Portugal

Date, Place

Tomás Périé de Barros

Eidestaatliche Erklärung

Hiermit erkläre ich, gemäß §5 der Promotionsordnung der Naturwissenschaftlichen Fakultät II - Chemie, Physik und Mathematik der Martin-Luther-Universität Halle-Wittenberg vom 13.06.2012, dass die vorliegende Arbeit

"Impact of electron correlation on light-induced demagnetization"

selbständig und ohne fremde Hilfe verfasst, andere als die von mir angegebenen Quellen und Hilfsmittel nicht benutzt und die den benutzten Werken wörtlich oder inhaltlich entnommenen Stellen als solche kenntlich gemacht habe. Ich erkläre, die Angaben wahrheitsgemäß gemacht und keine Dissertation an einer anderen wissenschaftlichen Einrichtung zur Erlangung eines akademischen Grades eingereicht zu habe

Date, Place	Tomás Périé de Barros